THE UNIVERSITY OF CHICAGO

ANISOTROPIC SEMICONDUCTOR NANOSTRUCTURES FOR DISPLAY APPLICATIONS

A DISSERTATION SUBMITTED TO

THE FACULTY OF THE DIVISION OF PHYSICAL SCIENCES

IN CANDIDACY FOR THE DEGREE OF

DOCTOR OF PHILOSOPHY

DEPARTMENT OF CHEMISTRY

BY

PATRICK DAVID CUNNINGHAM

CHICAGO, ILLINOIS

DECEMBER 2018

Table of Contents

List of Figures

Chapter One

Chapter Two

Chapter Three

Chapter Four

List of Tables

Acknowledgements

I wish to thank Professor Dmitri Talapin for his encouragement, patience, and stimulating discussions during my five years of graduate studies. His sharp intuition and dedication to his craft have been a tremendous driving force for my success. In my future endeavors, I will undoubtedly draw from this apprenticeship in scientific thinking with which he has provided me. I also thank my committee members, Professor Bozhi Tian and Professor John Anderson, for their help throughout the preparation of my thesis.

I have been fortunate enough to work with many outstanding colleagues during my time at the University of Chicago. Several people worked with me directly on my two projects: Dr. Chunxing She, Dr. Igor Fedin, Dr. Joao Bautista Souza, Jr., Dr. Igor Coropceanu, and Kavan Mulloy. Joao's incredible work ethic and discussions provided me with libraries of samples and synthetic insight—to him I owe much of my success. Igor C. gave me a spark that reinvigorated my passion for nanocrystal synthesis and scientific curiosity. In terms of colleagues not directly involved with my projects, Dr. Michael Boles was very supportive in my first days of joining the lab, mentoring me in experimental culture and the writing of reports. Dr. Matt Kurley was a constant source of guidance, friendship, and support. Dr. Vishwas Srivastava has been a great friend since our coursework and was always available for spirited discussion about research and life. Maggie Hudson, my fellow cat-owning friend: Thank you for many great conversations and scientific advice. Thank you to all of the other brilliant minds I have been fortunate enough to interact with in the Talapin Lab.

I would like to thank my chemistry professors at Franklin & Marshall College, the people who encouraged me to pursue my PhD and to whom I owe much of my success in graduate school. Thank you to Professors Scott Brewer, Richard Moog, and Jennifer Morford for shaping

my perspectives in chemistry and providing useful advice. A special thank you to Professor Katherine Plass, my undergraduate research advisor, for helping me build my synthetic expertise in the field of nanomaterials and advancing my scientific career.

To Tim Cronin, Ben Weissman, Kyle Gibson, Darren Veit, Dan Micheroni, Nick Williams, Anthony Schlimgen: thank you for your friendship throughout our 5 years here at U of C.

My life here in Chicago would not be the same without my friends outside of the community. A special thank you to Mclain Roth, a friend since the age of 10. I am so fortunate that you moved to Chicago early on in my PhD and provided guidance and healthy dose of distraction. It would like to thank all of the friends who have lived in or visited me in Chicago and were unfortunate enough to hear me rant or rave about my studies. Ian LeMay, Hongyi Pan, Wick Clothier, Nick Mraz, Ryan FitzGerald, Pedro Veiga de Almeida, Candice Tussing, Michael Friedman, Alexander Keto, Courtney Gregor, and Schuyler Routt. Thank you to David Kay and MetroSquash for giving me a healthy outlet to coach and play squash.

To my parents, Andrea and Mike: I am forever thankful for the love, emotional and financial support throughout my entire life. My siblings Ryan, Dylan, and Lauren have always been a phone call away and available to talk about whatever life throws our way.

To my parents-in-law, Denise and Allen: thank you for giving me permission to marry your daughter while still in the precarious position of being a starving grad student.

To incredible wife Kasey: I am so happy that you were by my side during this journey. I love you so much and truly could not have completed my PhD without you.

Abstract

The class of materials known as quantum dots (QDs) represent a tremendous success in the field of nanomaterials. Through engineering of particle size, shape, composition and effective optimization of their surfaces, these QDs can demonstrate color tunability and near unity photoluminescence quantum yield. These properties have led to incorporation in state-of-the-art display technology. Shape anisotropy of our emissive material leads to unique optical properties. The potential to generate ensemble material with precise linewidth and anisotropic radiation pattern remains an underexplored aspect for improving interaction with device stack and light outcoupling in display applications. Chapter One provides a detailed assessment of display-relevant optical parameters for solutions of highly emissive Cd-based anisotropic nanocrystals. In Chapter Two, the incorporation and alignment of these emissive materials into polymer films is discussed and their anisotropic radiation pattern is quantified. Chapter Three was motivated by the search for novel materials and details synthetic understanding of anisotropic ZnSe materials. Chapter Four is focused on the viability of creating bright core-shells with ZnSe quasi-2D nanostructures as the emissive core. Together, these chapters focus on anticipating the problem space in the next generation of displays, with the idea that anisotropic materials with narrow linewidth and direction emission will comprise the emitting layer.

1. Targeted synthesis of Cd-based anisotropic nanocrystals for display applications

1.1. Introduction: Quantum dots in state-of-the-art displays

The invention of liquid crystal display (LCD) technology has dramatically shaped the market for televisions, laptops, cellphones and other display technologies; the ability to generate sharp images in a light, compact housing with low power consumption has rendered cathode tube technology largely obsolete. LCD technology uses a backlight which transmits light through a device stack containing polarizers, liquid crystals, and color filters (Figure 1.1). The transparency of each pixel is adjusted by applying voltage across the liquid crystal cell. Traditional LCD technology utilizes color filters to generate color pixels from a white light source, which leads to large energy losses and requires efficient heat dissipation within LCD stack.

Recently, highly luminescent quantum dots (QDs) have made their way into existing display technologies—the current state of the art containing QDs as an emissive backlighting layer within ubiquitous liquid crystal display (LCD) architecture.[1-3] The benefits of QDs include increased brightness and color purity combined with stability superior to that of organic chromophores. These properties can be optimized through colloidal synthesis of nanometer-sized crystals of direct gap semiconductors by mediating their size, shape, and composition. Existing QD LCD technologies exploit the properties of quantum dots to absorb blue photons and emit red and green light matched to the transmission bands of color filters.[4] The pure colors produced by QDs give better color rendering, compared to traditional phosphors that yield broad spectra with red light shifted away from its spectral locus.[5] In the next generation technology, we envision replacing spherical QDs with nanostructures emitting linearly polarized light with high

color purity. In addition to the benefits of LCD with QD backlighting, such devices would efficiently transmit light through the first polarizer filter.[6-7] Anisotropic nanocrystals provide such a source of polarized emission. In CdSe nanorods, it is known that the breaking of spherical symmetry induces emission polarized along the long axis.[7] CdSe/CdS nanorod heterostructures are highly suitable as bright polarized emitters for LCDs—their reported photoluminescence quantum yields are as high as 85% and most recently close to 100% with optimization of shell growth conditions.[6, 8] The growth of a CdS shell on a CdSe spherical or prolate core yields a highly-emissive near-perfect polarized light source—the dielectric confinement forces a transition dipole to align along the long axis of the nanorod.[9] In addition, the symmetry of excitonic transitions in CdSe/CdS nano-heterostructures creates large anisotropy of optical transitions beyond the simple dielectric effect expected for 1D rods or wires.[9-10] An array of unidirectionally aligned nanocrystals could provide a source of macroscopic polarized emission, which can be imagined as a backlighting layer in LCD devices (Figure 1.1). Alternatively, CdSe nanoplatelets (NPLs) and their resulting core-shell heterostructures provide another potential nanomaterial with anisotropic optical properties. Nanoplatelets with a 2D electronic structure show emission wavelength dependent on thickness only.[10] Among all known nanomaterials, NPLs provide the highest color purity owing to the level of thickness control down to the atomic level.

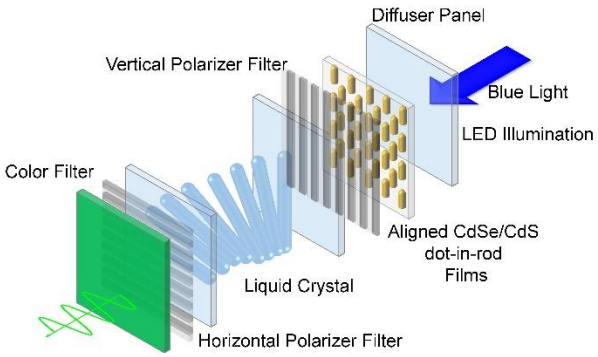

Figure 1.1. Scheme of a liquid-crystal display (LCD) using anisotropic nanocrystals as backlight source. Films could absorb unpolarized light from blue LED emitters and re-emit linearly polarized light with near unity quantum efficiency and polarization direction aligned with the vertical polarizer filter.

1.2. **Synthetic routes for highly luminescent colloidal nanorods and nanoplatelets**

We carried out a comparative study of highly luminescent anisotropic colloidal nanostructures with CdSe as the emissive component. This choice was motivated by high PL efficiency and stability of CdSe-based nanostructures and availability of synthetic routes toward high-quality nanomaterials with different electronic dimensionality. Moreover, CdSe-based quantum dots (QDs) have already demonstrated excellent performance in LCD devices.[10] Specifically, we compared spherical CdSe/CdS core-shell QDs[11] with CdSe/CdS dot-in-rod and rod-in-rod nanoheterostructures,[9, 12] as well as CdSe and CdSe/CdS nanoplatelets (NPLs) with the quantum well electronic structure[11-12] (Figure 1.2a-c). These materials covered examples of 0-, 1- and 2-dimensional electronic systems. CdSe/CdS dot-in-rods comprise a spherical wurtzite CdSe core epitaxially integrated in a CdS rod. These nanoheterostructures were synthesized using established procedures[7, 12-13] with some modification.[11]

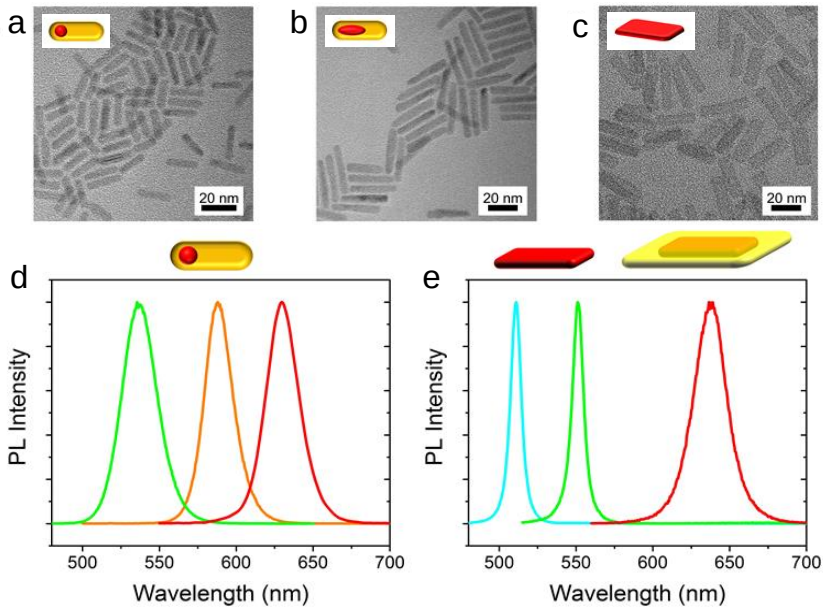

Figure 1.2. CdSe-based highly luminescent anisotropic nanostructures: TEM images of (a) CdSe/CdS dot-in-rods; (b) CdSe/CdS rod-in-rods; (c) CdSe nanoplatelets. (d,e) Characterization of ensemble spectral linewidths for CdSe based nanostructures. (d) Emission spectra of a colloidal solution of CdSe/CdS dot-in-rods. Green emitting rods are 3.5 x 9.0 nm with a 2.1 nm core; orange emitting rods are 5.1 x 35 nm with a 3.8 nm core; red emitting rods are 4.9 x 18 nm with a 4.6 nm core. (e) Emission spectra of bare CdSe nanoplatelets and CdSe/CdS core-shell nanoplatelets. The nanoplatelets emitting at 512 nm and 550nm have thickness 1.2 nm and 1.5 nm, respectively, corresponding to 4 and 5 CdSe unit cells. The red emission was observed for CdSe/CdS core-shells containing CdSe with 1.2 nm initial thickness.

1.2.1. Synthesis of CdSe seeds

In general, synthesis of CdSe followed modified literature protocols.[11-12, 14] To a three-neck round bottom flask CdO (0.060 g), n-octadecylphosphonic acid (ODPA, 0.308 g) and TOPO (3.0 g) were added and degassed for 1 hour at RT and 1-2 hours at 150 °C. The flask was then heated to above 300 °C under stream of N_2 and injected with TOP (1.5 g) when the solution was optically transparent. Trioctylphosphine selenide (TOPSe) (0.44 mL of 1.7 M) was injected at high temperatures—the size of our wurtzite cores was controlled by varying injection temperature and growth times. For example, green-emitting cores were synthesized by injection

of Se precursor at 380 °C followed by immediate quenching with toluene. Red-emitting cores were synthesized by injection of Se precursor at 370 °C with 5 minutes of growth time. Cores were transferred to a glovebox and diluted to 20 mL in toluene. The seeds were precipitated with methanol and washed at least twice more with resuspension and precipitation with toluene and methanol. The seeds were stored in TOP and their concentrations determined using the peak position of the first absorption.

The importance of a good interface between CdSe@CdS was emphasized. With respect to washing in oxygen environment, the photoluminescence of CdSe dropped off significantly. It is for this reason that CdSe "seeds" were washed and stored in the glovebox before epitaxial growth. This washing likely prevents surface oxidation of Se and leads to good epitaxial growth on a surface with homogenous composition.

1.2.2. Shell growth synthesis of CdSe/CdS nanorods.

For CdS shell growth procedure, variations on literature protocols were used.[15-16] In a typical synthesis, a three-neck round bottom flask containing CdO (0.060 g-0.207 g), ODPA (0.290-1.29 g), TOPO (2.0-3.0 g) and an additional short chain n-alkylphosphonic acid (hexyl (0.080 g) or propyl (0.015 g)) was degassed for 1 hour at RT and 1-2 hours at 150 °C. The flask was heated to above 300 °C under stream of N_2 and injected with TOP. The flask was then heated to varying temperatures (320-380 °C) and injected with a dispersion of trioctylphosphine sulfide (TOP, 0.5-1.6 g of 2.25 M) and a solution of w-CdSe (50-500 nmol) in TOP. Shell-growth times were varied between 30 s and 10 mins.

1.2.3. CdSe/CdS nanorod washing and storage

The resulting heterostructure nanorods were diluted to 20 mL in toluene and precipitated with ethanol. After resuspension in toluene, the particles were precipitated with 1% v:v

octylamine in ethanol. Nanostructures were stored in toluene with an excess of octylamine. High quantum yields were preserved through addition of excess ligand, such as n-octylamine, to improve colloidal stability of nanorod solutions upon storage.[16] In order to retain high quantum yield over extended period of time, sample exposure to oxygen has to be minimized prior to shell growth by washing solutions of CdSe "seeds" in inert atmosphere. Through additional annealing and surface passivation with Cd and S precursors, quantum yields approaching 100% can be achieved for CdSe/CdS spherical core-shells[16] and dot-in-rod samples[16] according to recent studies by the Bawendi group.

In a representative set of particles, quantum yield increased from 51% to 72% over 1 week of storage in the presence of octylamine. Thus, this post-synthetic modification increases the quality of our samples for incorporation into films.

1.2.4. Synthesis of three lateral dimensions of 512 nm (4 ML) CdSe NPLs

To synthesize 512 nm CdSe NPLs, we followed a recipe from with slight modifications.[16] Namely, we degassed 170 mg $Cd(myristate)_2$ in 15 ml ODE at the room temperature for 30 min, then we added 12 mg of Se powder and degassed the system for 30 min at 90 °C. Then we rapidly heated up the reaction mixture to 240 °C under nitrogen. At 190 °C, when the solution turned orange-red, we introduced 40 mg of finely ground $Cd(OAc)_2$. We ran the reaction at 240 °C for 5 min, then quickly cooled down the reaction mixture to 150 °C and allowed it to further cool down. At 70 °C, we injected a solution of 2 ml of oleic acid in 10 ml ODE. When the system cooled down to the room temperature, we precipitated the NPLs by centrifugation and re-dispersed them in hexane. By taking aliquots, we noticed the NPLs acquired their spectroscopic features soon after the introduction of $Cd(OAc)_2$. We hypothesize that the NPLs acquire their

target thickness fast and then grow laterally. We can thus terminate the recipe prematurely to obtain shorter 512 nm NPLs. The degree of control is demonstrated in Figure 1.3.

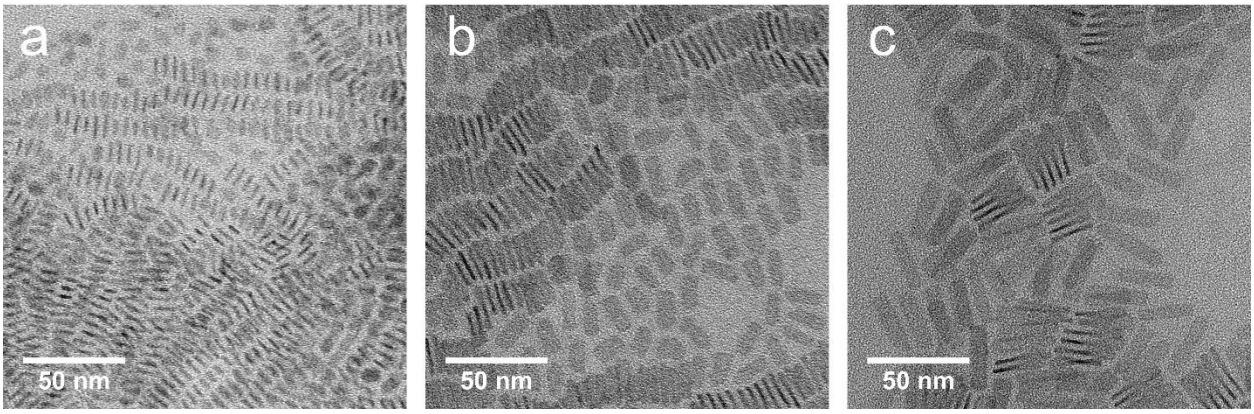

Figure 1.3. Transmission electron microscope images of CdSe NPLs with 1.2 nm thickness and different lateral dimensions: (a) “short” (b) “medium” (c) “long”.

1.2.5. Synthesis of 550 nm (5 ML) CdSe NPLs

To synthesize 550 nm CdSe NPLs, we followed exactly the recipe from the source.[16] Namely, we degassed 170 mg $Cd(myristate)_2$ in 14 ml ODE at the room temperature, heated up the reaction mixture under nitrogen, at 240 °C injected 12 mg of Se powder pre-dispersed in 1 ml ODE by sonication, in 20 s introduced 60 mg of finely ground $Cd(OAc)_2$, ran the reaction for 10 min, cooled down the reaction mixture, and at 80 °C injected 2 ml of oleic acid in 15 ml ODE. When the suspension reached the r.t., we centrifuged it without a non-solvent and re-dispersed the NPLs in hexane.

1.2.6. Shell-growth synthesis on CdSe/CdS NPLs using c-ALD

The route to colloidal atomic layer deposition (c-ALD) was first discovered in our lab.[17] We used the modified technique outlined in ref.[18] for these procedures.

1.2.7. CdSe NPL post-synthetic isolation to avoid detrimental stacking

512 nm and 550 nm CdSe NPLs tend to form stacks of 5 – 30 NPLs. A recent work by B. Guzelturk *et al*.[14] demonstrates a 3-picosecond homo-FRET rate in stacks of 512 nm CdSe NPLs. One defective NPL in a stack can serve as an exciton drain and lower thus the PL efficiency of the sample. We modified the recipes for the regular 512 nm and 550 nm NPLs so that, after the completion of the reaction at 240^{o}C, we collected the hot reaction mixture with a glass syringe and injected it into a solution of oleic acid in hexane. This modification lowered the degree of NPL stacking and increased the PL efficiency of NPL solutions.

1.3. **Comparative characterization of nanocrystal photoluminescence**

The critical parameters for application in LCD backlighting, PL quantum yield and color purity (*i.e.*, full width at half-maximum of the PL spectrum) have been assessed for different dot-in-rod and rod-in-rod samples. In order to achieve high PL quantum yields and fwhm for the same samples, extensive optimization of synthetic parameters is often required.

1.3.1. Determination of Quantum Yield

Most of the general procedure for determination of quantum yield is detailed here. Optical measurements were done using dilute solutions of nanocrystals in toluene or hexane using UV-Vis (Cary-5000) and fluorescence (FluoroMax-4 and Fluorolog-3) spectrometers. Quantum yield was calculated with respect to Rhodamine 6G with solution optical density at the excitation wavelength between 0.03 and 0.05. PL spectra are taken and the integrated areas are used in the following calculation of quantum yield:

$$QY = 0.95 \frac{I_x}{I_{st}} \frac{(1 - 10^{-A_{st}})}{(1 - 10^{-A_x})} \left(\frac{n_{tol}}{n_{EtOH}}\right)^2$$

Where x is the sample and st is Rhodamine 6G with I representing the integrated emission intensity, A representing the optical density in the absorption spectra, and n representing the refractive indices of the given solvent. It is important to note that the samples are excited at the wavelength where optical density is equal. Therefore, this term is equal to ~1 and dropped out in our calculation.

For the determination of PL quantum yield we used fresh Rhodamine 6G, Coumarin 153, and Oxazine 170 perchlorate dyes in ethanol solution. In general, the samples were excited at the wavelength where the absorption spectra of the organic dye and nanocrystal solution were equal (Figure 1.4). The optical density of the solution at this wavelength was kept between 0.03 and 0.05.

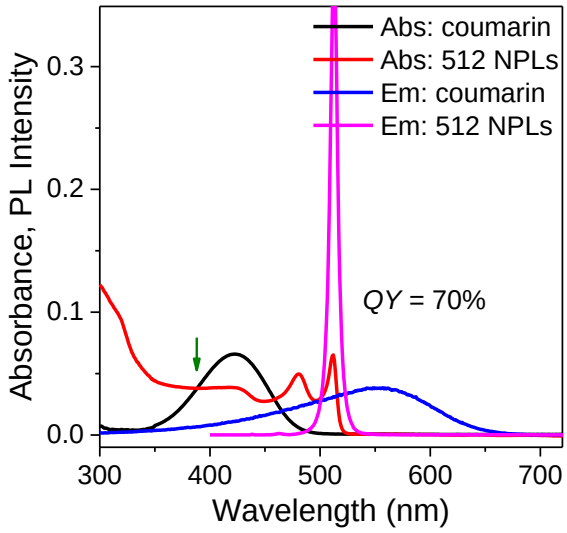

Figure 1.4. Representation of method used to determine photoluminescence quantum yield in CdSe NPLs in comparison with an organic standard dye.

1.3.2. Highest obtained values of quantum yield

Our measured values are on par or higher than the best literature values for PL quantum yield of dot-in-rod[19] and rod-in-rod[20] CdSe/CdS NCs. Dot-in-rod CdSe/CdS had typical PL

quantum yields of 70-90%, with highest yields of 93%, 77%, and 70% for green, orange, and red, respectively (Figure 1.5). Rod-in-rod CdSe/CdS samples demonstrated PL yields reaching 74% (Figure 1.5). High quantum yields were preserved through addition of excess ligand, such as n-octylamine, to improve colloidal stability of nanorod solutions upon storage.[21] Typical quantum yields of bare CdSe NPL samples can be high, up to 50-70% (Figure 1.5). For core-shell NPLs, reported literature values can be as high as 80%.[22]

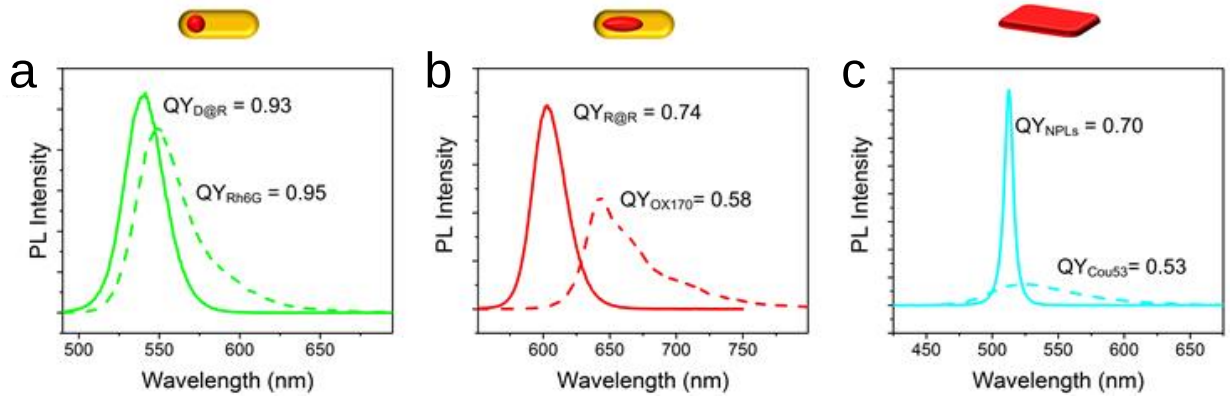

Figure 1.5. Determination of nanostructure photoluminescence quantum yields by comparison with organic standard dyes[14] for (a) CdSe@CdS dot-in-rods, (b) CdSe@CdS rod-in-rods and (c) CdSe nanoplatelets.

1.3.3. Photoluminescence spectral linewidth of ensembles

Narrow emission spectra are crucial for attaining high purity of primary red, green and blue colors of individual LCD pixels. High purity of primary colors provides better color saturation and a wider color gamut can be realized by mixing pure primary colors. From this perspective, colloidal semiconductor nanostructures are among the best options because of their narrow near-Gaussian emission spectra.[1, 23-26] We found that typical full-widths at half maximum (FWHM) were between 25-35 nm for as-synthesized CdSe/CdS nanorod heterostructures (Figure 1.2d). Lowest FWHM were 28, 21, and 26 nm for our green, orange, and red dot-in-rods,

respectively, with the lowest FWHM of 28 nm for rod-in-rods. Theses narrowest spectral linewidths could be obtained through size fractionation.

1.3.4. Estimation of highest attainable linewidths by PLE spectroscopy

The spectral width of QD samples is determined by the convolution of homogeneous linewidths of individual particles and inhomogeneous broadening that can, in principle, be eliminated by synthesis optimization or size-selective fractionation of colloidal solutions.[26] Photoluminescence excitation (PLE) spectroscopy is a simple and convenient way to reduce the inhomogeneous contribution to ensemble emission spectra; this technique was used to estimate homogeneous linewidth at room temperature (Figure 1.6 and Figure 1.7).[15] Size fractionation[27] can easily reduce spectral widths of dot-in-rod samples down to 25 nm or less. To compare these data with homogeneous linewidths for these samples, we carried out photoluminescence excitation (PLE) measurements on colloidal samples (Figure 1.6 and Figure 1.7).

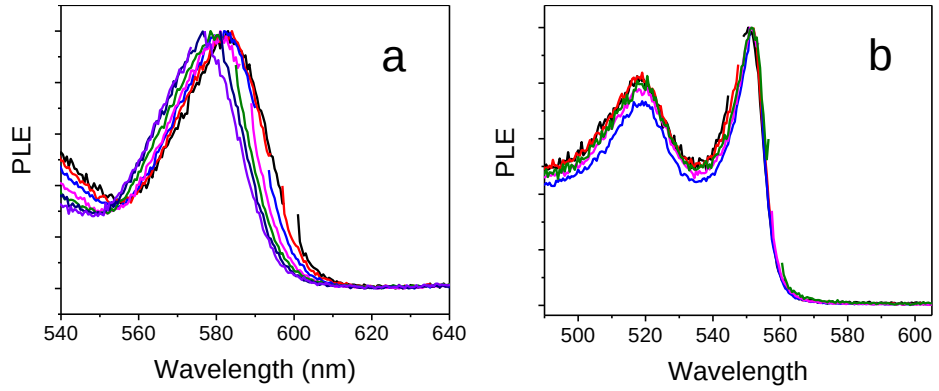

Figure 1.6. Difference in inhomogenous broadening between two different dimensionalities: (a) PLE spectra of CdSe/CdS nanorods taken at different emission wavelengths (slit width = 1 nm) reveal significant inhomogenous broadening coming from particle size distribution. (b) PLE spectra of CdSe nanoplatelets emitting at 550nm, taken at different emission wavelengths (slit width = 1 nm) reveal negligible inhomogenous broadening in NPLs**.**

Significantly higher color purity can be achieved for CdSe colloidal nanoplatelets (NPLs). Typical synthesis yields atomic level control over the thickness of the platelets, yielding emission from blue to green with narrow spectral linewidth (Figure 1.2). Ensemble PLE measurements of NPLs show negligible inhomogeneous broadening of ensemble spectra (Figure 1.6b and Figure 1.7c). Additional surface passivation of these systems can be done by growing a shell of CdS around the NPLs that shifts PL into red without introducing inhomogeneous broadening.[28]

Dot-in-rod samples with emission FWHM of 23 nm had the linewidth of the first excitonic peak of about 20 nm in PLE spectra measured with 1 nm slits (Figure 1.7a). Rod-in-rod samples with ensemble linewidths of 33 nm had homogenous linewidths of 25 nm (Figure 1.7b). These numbers provide estimates for potentially attainable PL FWHM and color purity of dot-in-rods and rod-in-rods ensembles. It is also possible that fractionation of the colloidal solutions of "seeds" could provide even further minimization of spectral linewidths. These data also show that PL FWHM of CdSe/CdS dot-in-rods and rod-in-rods are on par with spherical CdSe/CdS QDs.[8]

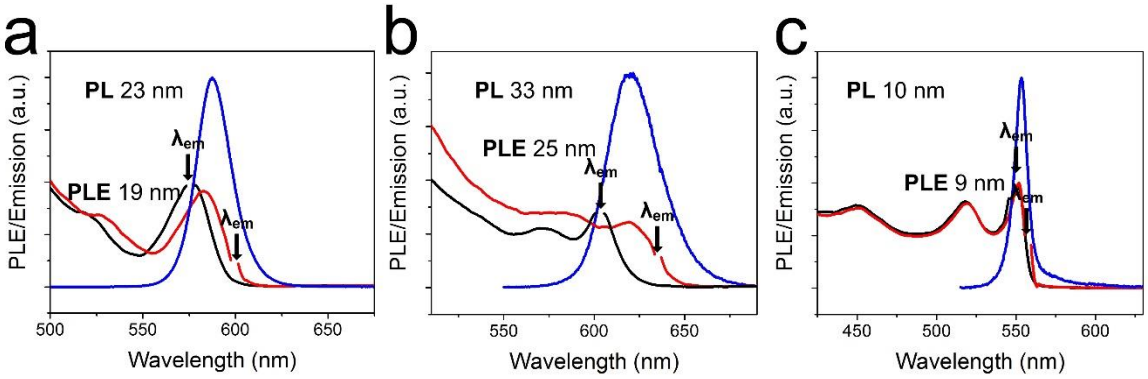

Figure 1.7. Linewidths estimated from PLE spectra measured at high (black curves) and low energy (red curves) wavelengths of the emission profiles (blue curves) for (a) CdSe/CdS dot-in-rods (orange emitting rods without size fractionation from Figure 1.2), (b) CdSe/CdS rod-in-rods (5.9 x 23 nm with 3.4 x 8.6 nm core), (e) CdSe nanoplatelets emitting at 550nm. The excitation and emission slits were fixed at 1 nm.

1.4. **Optical polarization and anisotropy of Cd-based structures in solution**

The optical polarization of light emission is crucial to the implementation of nanorods into LCD devices. Using aligned CdSe-based nanostructures with high color purity, high quantum yield, and linearly polarized emission, is imagined that we can preselect for polarized emission that efficiently propagates through the first vertical polarizer in LCD architecture. The growth of nanocrystals into anisotropic structures induces polarization of absorption and emission due to the unequal electric field strength along different dimensions. It has been established that a structure with anisotropic shape (*i.e.* ellipsoid), will attenuate electric fields perpendicular to the long axis or axes.[8] In the case of a long cylinder in external electric field, the orientation of the field with respect to the long axis can affect the magnitude of internal electric field. This difference can approach a factor of 2 for a long cylinder where external fields are aligned along and normal to the cylinder axis. However, polarization in CdSe/CdS dot-in-rods and rod-in-rods goes beyond what can be explained by simple dielectric effects. The additional anisotropy originates from the splitting of the exciton fine structure in wurtzite CdSe core.[6, 29] The fine excitonic structure of the band edge in wurtzite CdSe is determined by the oscillator strength of the 0^U excitonic state linearly polarized along the *c*-axis *versus* that of the ±1 states circularly polarized along the *ab* plane.[28] When a nearly spherical nanocrystal is elongated into a rod with aspect ratio (AR) greater than 1.25, the oscillator strength of the linearly polarized transition outweighs that of the plane polarized transitions.[28] The opposite case is true for nearly spherical CdSe quantum dots.[28] The requirement in reaching large values of linear polarization is a large enough core size to cause a swapping of the energy levels responsible for the 1D and 2D dipole emission; further increases in polarization occur by changing spacing between these two levels as a result of a strain effect with thinner and longer shells.[28] In choosing CdSe-based

nanostructures as the emissive component, we anticipate dot-in-rod and rod-in-rod heterostructures to be the ideal candidates because of their high degree of linear polarization. Our aim was to compare the optical anisotropy of different nanostructures.

1.4.1. Measuring anisotropy in solution

The detailed procedures and theory related to optical anisotropy of solution samples are available in previous studies and detailed in following sections.[28, 30] Anisotropies were measured in a JobinYvonne Fluorolog 3 using computer-controlled polarizers. In general, the optical density in the region of interest for the sample was kept below 0.05 and their absorption spectra were taken prior to measurement. The anisotropies were recorded at 1 or 2 nm increments over regions blueshifted from the band edge. As many samples have a much higher extinction coefficient at higher energies, the regions blueshifted in the spectra were not recorded. This was done to avoid the inner filter effect and saturating the detector signal. In case of CdSe nanoplatelets, measuring the "band-edge" anisotropy required particular caution due to a small Stokes shift that increases possibility of excitation scatter in the emission channel.

We compared the polarized excitation of states in nanostructures of varying geometry to probe the energy-dependence of polarization by using a method for determining anisotropy using photoluminescence excitation scans of nanocrystal ensembles (Figure 1.8a-d).[31-32] For each sample we measured a series of PLE scans using various configurations of vertical and horizontal polarizers placed at the excitation and emission channels. The anisotropy (R) was calculated as:

$$R = \frac{I_{\parallel} - I_{\perp}}{I_{\parallel} + 2I_{\perp}} = \frac{I_{VV} + I_{VH}}{I_{VV} + 2GI_{VH}} \quad (1)$$

where $I_{\parallel}$ and $I_{\perp}$ represent the intensity of light emitted parallel and perpendicular to the excitation and I_{VV} and I_{VH} are the configurations of polarizer filters at excitation and emission channels in

the measurement set up. We corrected for the differential throughput of the emission monochromator with a factor $G = I_{HV}/I_{HH}$.

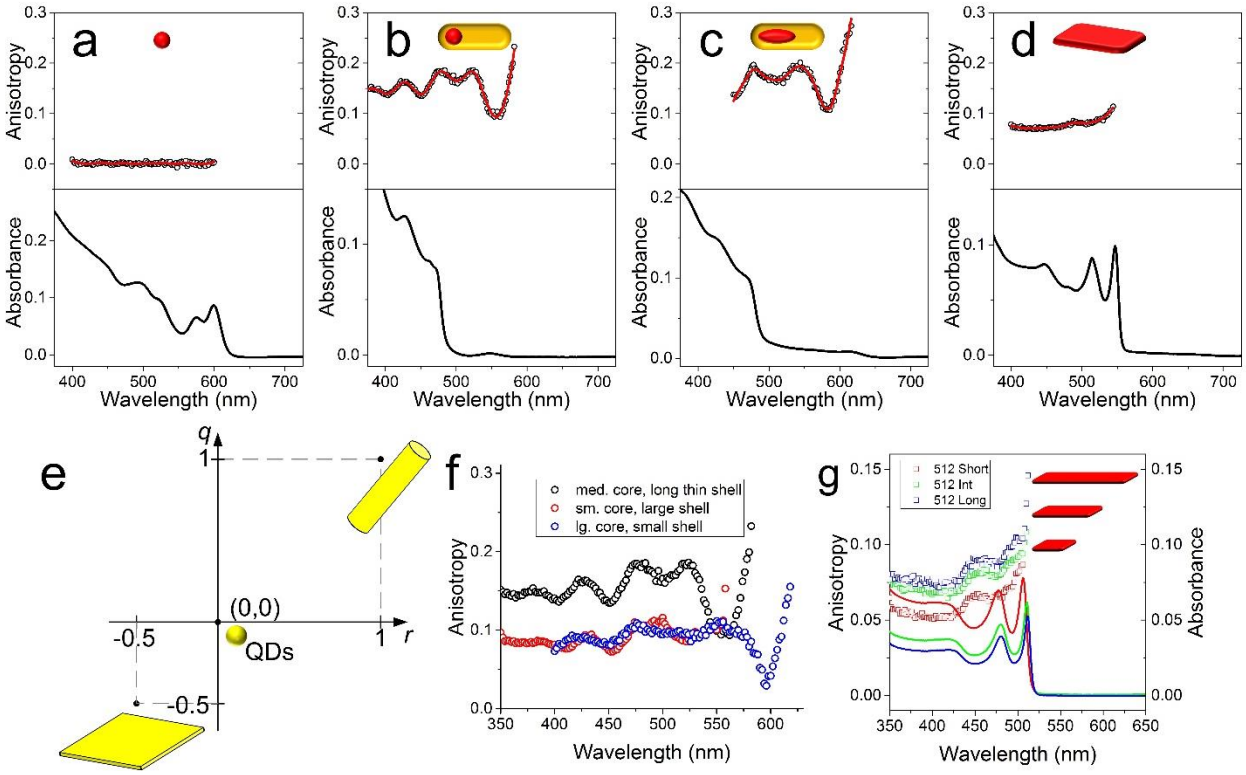

Figure 1.8**.** Anisotropy (open circles, red curve) and absorption (black curve) of quantum nanostructures: (a) CdSe sphere (5 nm); (b) CdSe/CdS dot-in-rod (5.1 x 35 nm; 3.8 nm core); (c) CdSe/CdS rod-in-rod (5.2 x 45 nm; 3.8 x 9.0 nm core); (d) CdSe nanoplatelet. (e) A scheme showing absorption and emission polarizations attainable for ideal dots, rods and platelets. (f) Comparison of optical anisotropy in different samples of CdSe/CdS dot-in-rods with varying core and shell dimensions. Medium core, long thin shell corresponds to 5.1 x 35 nm shell with a 3.8 nm core. Small core, large shell corresponds to 6.5 x 12 nm shell with a 2.3 nm core. Large core, small shell corresponds to 4.9 x 18 nm with a 4.6 nm core. (g) Solution anisotropy (open squares) and absorbance (solid lines) of three samples of CdSe nanoplatelets with identical thickness and different lateral dimensions: 3.9 x 8.8 nm for "short", 7.1 x 17 nm for "medium" and 8.7 x 29 nm for "long", see also Figure 1.3.

1.4.2. Theoretical maxima of perfectly polarized emission

The traditional definition of optical anisotropy assumes that the fluorophores are dipole oscillators. Since nanorod excitation and emission are not perfect point dipoles, our measurable value of R is reduced. For nanorods, the reduction of R into a combination of measurable

parameters has been given rigorous treatment in previous literature.[26] By taking into account the random orientation of nanorods as measured by photoselection and the fact that NRs are not perfect dipole oscillators and are represented by so-called imperfect absorption, (r), and imperfect emission polarization, (q), one can arrive at the expression for anisotropy for a system with a cylindrical symmetry:

$$R = \frac{2}{5}rq \tag{2}$$

Based on an approximation for an isotropic ensemble of cylindrical dipoles we can provide a direct relation of the total excitation anisotropy R to the absorption and emission anisotropy of individual chromophores. These two anisotropies are measured as projections along axes (r_x, r_y, r_z) and (q_x, q_y, q_z) with the values normalized such that $r_x + r_y + r_z = 1$ and $q_x + q_y + q_z = 1$. Since the minor nanorod axes are equivalent by symmetry, the intensities along these axes are equivalent ($r_x = r_y$) and ($q_x = q_y$). By reduction, we can come up with an expression for individual (r) and (q) where anisotropy is equivalent to the following:

$$r = \frac{r_z - r_x}{r_z + 2r_x};\ q = \frac{q_z - q_x}{q_z + 2q_x} \tag{3}$$

In the case of nanorods (where $r_z > r_x + r_y$ and $q_z > q_x + q_y$), both r and q can take values between 0 and 1, where our maximum values obtained from Eq. (3) are (1, 1) for (r, q) as shown in Figure 1.8e. Thus for a perfectly polarized emitter we expect to obtain values of 0.4 from Eq. (2). Therefore, reasonable approximation or direct measurement of two of the variables can yield the remaining one; thus, our solution measurement of optical anisotropy, R, is directly related to the relevant parameter of emission anisotropy, q. For a given sample of dot-in-rods both R and r should be dependent on the excitation energy, whereas q should be more or less fixed. For example, if we experimentally obtain an approximate value for absorption anisotropy of 0.9 in a sample of rod-in-rods and our solution anisotropy measures 0.3 at the band edge, then we can

expect from Eq. 2 the emission anisotropy at the band edge to be ~0.83. We can assume that for nanoplatelets, the intensity of absorption and emission are approximately equal along the two longer axes ($r_x \sim r_y$ and $q_x \sim q_y$). It necessarily follows that we can relate an ensemble of platelets using the same formalism in Eq. 1.2. However, in the case of nanoplatelets, the intensity along the unique axis is less than the two longer axes ($r_z < r_x + r_y$ and $q_z < q_x + q_y$). Thus the anisotropies of platelets are between -0.5 and 0 for r and q and we obtain maximum values of (-0.5, -0.5) for (r, q) from Eq. 3 as shown in Figure 1.8e. This would lead to a maximum value of $R = 0.1$ in the case of a nanoplatelet with perfectly polarized emission.

1.4.3. Comparison of nanocrystal emitters of different dimensionality

In order to rule out possible artifacts from our measurement setup, we also measured PLE anisotropy of samples of spherical wurtzite CdSe quantum dots. Although it is known that the transitions in the *ab* plane are expect to dominate for spherical wurtzite CdSe particles, we do not expect to observe net anisotropy at room temperature.[26] In our case, spherical wurtzite CdSe QDs yielded a featureless spectrum centered at $R = 0$, indicating no net anisotropy (Figure 1.8a). However, it is important to note that nearly spherical CdSe/CdS core-shell quantum dots have non-zero anisotropy near the band edge (Figure 1.9). CdSe/CdS dot-in-rod and rod-in-rods have similar trends in solution anisotropy, with greatest values being measured at the band edge (Figure 1.8b-c). Spectral features in these systems represent the various excitonic states; for example, the minimum at energies slightly higher than the band edge corresponds to off-axis transitions in wurtzite CdSe arising from dipoles that are not coaligned. Typically, this minimum would correspond to a state with negative anisotropy; however, negative values of anisotropy are not present due to the dielectric effect of the CdS rod-like shell.[26] These features are observed across several samples and it was confirmed that polarization of dot-in-rod samples is maximized

by increased core size and enhanced by a longer, thinner shell (Figure 1.8f). Rod-in-rods typically have band-edge anisotropies greater than that of dot-in-rods, which is consistent with the observation that rod-in-rods can attain nearly perfect polarized emission.[33] The best dot-in-rod samples demonstrated a band-edge anisotropy of 0.24, whereas the best rod-in-rod sample had a measured band-edge anisotropy of 0.27 (Figure 1.8b-c). Indeed, if absorption anisotropy is assumed to be ~0.9 in both cases, from Eq. 2 the two measured band-edge anisotropies would correspond to DOLP of 0.75 and 0.82 (CR of 7 and 10), respectively. Indeed, this small difference can lead advantageous gains in contrast ratio for display applications. CdSe NPLs were observed to have an anisotropy of 0.07 at higher energies, with an increase to above 0.1 near the band edge (Figure 1.8d). This indicates that we have a nearly perfectly polarized emitting nanoplatelet. Additional enhancement of the anisotropy, up to 0.15, is demonstrated in elongated NPLs (Figure 1.8g). The presence of polarized transitions in CdSe NPLs prompted us to explore this candidate as a polarized emitter in an aligned film. We can expect that if the long dimensions of rectangular NPLs are aligned unidirectionally, a material with high color purity and polarized emission can be achieved.

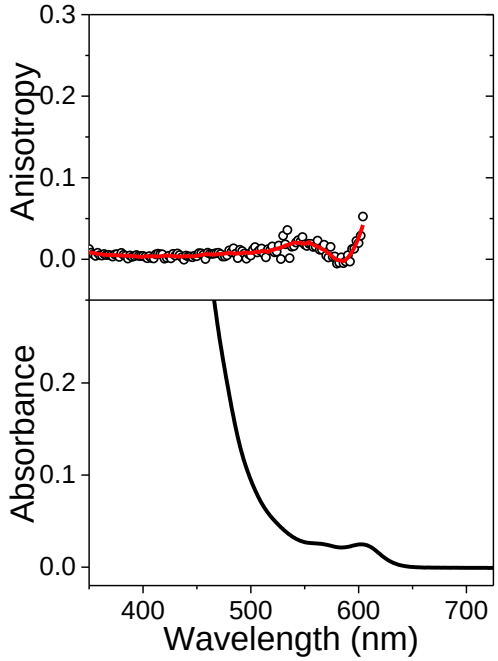

Figure 1.9. Anisotropy (open circles, red curve) and absorption (black curve) of nearly spherical CdSe/CdS core-shell quantum dots.

1.4.4. Ideal dimensionalities for core-shell nanorods

The best way to optimize polarization within these structures is to grow sufficiently thin and long shells by increasing precursor concentrations in shell-growth synthesis. Additionally, we can make the CdSe cores slightly larger (~2.5-3.0 nm in diameter) in order to obtain a suitable fine exciton structure for increased polarization.[30] However, this polarization may compromise pure green emission, as the increase of core size would shift the peak emission to the wavelengths greater than 550 nm. For red-emitting nanorods, the effect of CdS shell on the emission wavelength is weaker. Dot-in-rod samples with medium sized cores (~3-4 nm) and very long and thin shells provided the largest values of anisotropy at both band edge and blue excitation energies (Figure 1.8f). Samples with large cores had higher band edge anisotropies than those with smaller cores but their higher energy anisotropies are similar—likely due to the

similar size and aspect ratio of their CdS shells (Figure 1.8f). The polarization can be optimized by using a sufficiently large CdSe rod as the seed, which should increase the energy spacing between the optically active excitonic states. Ideally, rod-in-rod heterostructures should be used for red emission. This increased spacing enhances the polarization and the growth of a thin and long shell would not be as critical.

In order to optimize anisotropies for both red and green emission colors, one should focus on the physical dimensions of core-shell nanorods with respect to their inherent optical anisotropies rather than their susceptibility to efficient alignment. For green nanorods, the emission polarization will be lower due to the smaller gap in the optically active excitonic states;[30] therefore it is likely that a maximum degree of linear emission polarization of 0.5 can be obtained for dot-in-rod structures

1.4.5. Expected polarization in nanoplatelets

CdSe NPLs have electronic structure that can be described using the quantum well (QW) model.[33-34] In a QW, there are two optical polarization directions: one with the optical electric vector parallel to QW layer ("transverse electric" or TE polarization); and the other with the optical electric vector perpendicular to QW layer ("transverse magnetic" or TM polarization).[34] TE-polarized light can be emitted either out of the face or the edge of the QW, whereas TM polarized light can only be emitted out of the edge of the QW. The lowest energy heavy-hole (hh) to conduction band transition couples to TE-polarized emission, while the light-hole (lh) to conduction band transition couples predominantly to TM-polarized emission with a minor TE-polarized component.[35] A strong quantum confinement in CdSe NPLs leads to the large hh-lh energy level splitting of 157 meV (~6.3 k_BT at 300K) and 135 meV (~5.4 k_BT at 300K) for NPLs emitting at 512nm and 550nm, respectively.[36] As a result, the emission of CdSe NPLs is

expected to be strongly dominated by the TE mode. In a QW with large lateral dimensions, the TE mode emitted normal to QW face is circularly polarized.[37] However, since few studies exist regarding the anisotropic electronic structure of CdSe NPLs, the contribution of hh and lh states to optical anisotropy is unclear. It is expected that the small lateral dimensions and elongated shape of CdSe NPLs (Figure 1.2c) induce confinement of the exciton along the smaller lateral dimension that is expected to introduce linear polarization to the TE component emitted out of the NPL face. The band-edge hh transition demonstrates the largest anisotropies, likely due to the introduction of linear polarization to the TE component. The lh transition corresponds to a weak anisotropy minimum in all studied samples of 512 nm NPLs (Figure 1.8g).

1.5. **References**

1. Talapin, D. V.; Steckel, J., Quantum Dot Light-Emitting Devices. *MRS Bull.* **2013,** *38* (09), 685-691.

2. Jang, E.; Jun, S.; Jang, H.; Lim, J.; Kim, B.; Kim, Y., White-Light-Emitting Diodes with Quantum Dot Color Converters for Display Backlights. *Adv. Mater.* **2010,** *22* (28), 3076-3080.

3. Gee, M. B.; Lee, J. A.; Kim, K. C.; Lee, K.; Yoon, K. J.; Park, J. P.; Cho, S. H.; Noh, H. J.; Jang, K. K.; Jeong, K. S. Liquid Crystal Display Device. 2003.

4. Banin, U.; Arbell, H. Polarizing lighting systems. U.S. Patent Application 13/883,701, 2014.

5. Cho, C.; Kim, D. H.; Ha, S. W. Quantum Rod Sheet, Backlight Unit, Display Device and Manufacturing Method thereof. 2014.

6. Hu, J.; Li, L.-s.; Yang, W.; Manna, L.; Wang, L.-w.; Alivisatos, A. P., Linearly Polarized Emission from Colloidal Semiconductor Quantum Rods. *Science* **2001,** *292* (5524), 2060-2063.

7. Talapin, D. V.; Koeppe, R.; Götzinger, S.; Kornowski, A.; Lupton, J. M.; Rogach, A. L.; Benson, O.; Feldmann, J.; Weller, H., Highly Emissive Colloidal CdSe/CdS Heterostructures of Mixed Dimensionality. *Nano Lett.* **2003,** *3* (12), 1677-1681.

8. Shabaev, A.; Efros, A. L., 1D Exciton Spectroscopy of Semiconductor Nanorods. *Nano Lett.* **2004,** *4* (10), 1821-1825.

9. Ithurria, S.; Dubertret, B., Quasi 2D Colloidal CdSe Platelets with Thicknesses Controlled at the Atomic Level. *J. Am. Chem. Soc.* **2008,** *130* (49), 16504-16505.

10. Wang, F.; Wang, Y.; Liu, Y.-H.; Morrison, P. J.; Loomis, R. A.; Buhro, W. E., Two-Dimensional Semiconductor Nanocrystals: Properties, Templated Formation, and Magic-Size Nanocluster Intermediates. *Accounts of Chemical Research* **2015,** *48* (1), 13-21.

11. Talapin, D. V.; Nelson, J. H.; Shevchenko, E. V.; Aloni, S.; Sadtler, B.; Alivisatos, A. P., Seeded Growth of Highly Luminescent CdSe/CdS Nanoheterostructures with Rod and Tetrapod Morphologies. *Nano Lett.* **2007,** *7* (10), 2951-2959.

12. Carbone, L.; Nobile, C.; De Giorgi, M.; Sala, F. D.; Morello, G.; Pompa, P.; Hytch, M.; Snoeck, E.; Fiore, A.; Franchini, I. R.; Nadasan, M.; Silvestre, A. F.; Chiodo, L.; Kudera, S.; Cingolani, R.; Krahne, R.; Manna, L., Synthesis and Micrometer-Scale Assembly of Colloidal CdSe/CdS Nanorods Prepared by a Seeded Growth Approach. *Nano Lett.* **2007,** *7* (10), 2942-2950.

13. Guzelturk, B.; Erdem, O.; Olutas, M.; Kelestemur, Y.; Demir, H. V., Stacking in Colloidal Nanoplatelets: Tuning Excitonic Properties. *ACS Nano* **2014,** *8* (12), 12524-12533.

14. Bullen, C.; Mulvaney, P., The Effects of Chemisorption on the Luminescence of CdSe Quantum Dots. *Langmuir* **2006,** *22* (7), 3007-3013.

15. Chen, O.; Zhao, J.; Chauhan, V. P.; Cui, J.; Wong, C.; Harris, D. K.; Wei, H.; Han, H. S.; Fukumura, D.; Jain, R. K.; Bawendi, M. G., Compact High-Quality CdSe-CdS Core-Shell Nanocrystals with Narrow Emission Linewidths and Suppressed Blinking. *Nat. Mater.* **2013,** *12* (5), 445-51.

16. Pelton, M.; Ithurria, S.; Schaller, R. D.; Dolzhnikov, D. S.; Talapin, D. V., Carrier Cooling in Colloidal Quantum Wells. *Nano letters* **2012,** *12* (12), 6158-6163.

17. Ithurria, S.; Talapin, D. V., Colloidal Atomic Layer Deposition (c-ALD) using Self-Limiting Reactions at Nanocrystal Surface Coupled to Phase Transfer between Polar and Nonpolar Media. *Journal of the American Chemical Society* **2012,** *134* (45), 18585-18590.

18. She, C.; Fedin, I.; Dolzhnikov, D. S.; Demortière, A.; Schaller, R. D.; Pelton, M.; Talapin, D. V., Low-Threshold Stimulated Emission Using Colloidal Quantum Wells. *Nano Lett.* **2014,** *14* (5), 2772-2777.

19. Tessier, M. D.; Mahler, B.; Nadal, B.; Heuclin, H.; Pedetti, S.; Dubertret, B., Spectroscopy of Colloidal Semiconductor Core/Shell Nanoplatelets with High Quantum Yield. *Nano letters* **2013,** *13* (7), 3321-3328.

20. Bae, W. K.; Brovelli, S.; Klimov, V. I., Spectroscopic Insights into the Performance of Quantum Dot Light-Emitting Diodes. *MRS Bull.* **2013,** *38* (09), 721-730.

21. Bozyigit, D.; Wood, V., Challenges and Solutions for High-Efficiency Quantum Dot-Based LEDs. *MRS Bull.* **2013,** *38* (09), 731-736.

22. Chen, O.; Wei, H.; Maurice, A.; Bawendi, M.; Reiss, P., Pure Colors from Core–Shell Quantum Dots. *MRS Bull.* **2013,** *38* (09), 696-702.

23. Kim, T.-H.; Jun, S.; Cho, K.-S.; Choi, B. L.; Jang, E., Bright and Stable Quantum Dots and their Applications in Full-Color Displays. *MRS Bull.* **2013,** *38* (09), 712-720.

24. Supran, G. J.; Shirasaki, Y.; Song, K. W.; Caruge, J.-M.; Kazlas, P. T.; Coe-Sullivan, S.; Andrew, T. L.; Bawendi, M. G.; Bulović, V., QLEDs for Displays and Solid-State Lighting. *MRS Bull.* **2013,** *38* (09), 703-711.

25. Norris, D. J.; Sacra, A.; Murray, C. B.; Bawendi, M. G., Measurement of the Size Dependent Hole Spectrum in CdSe Quantum Dots. *Phys. Rev. Lett.* **1994,** *72* (16), 2612-2615.

26. Achtstein, A. W.; Schliwa, A.; Prudnikau, A.; Hardzei, M.; Artemyev, M. V.; Thomsen, C.; Woggon, U., Electronic Structure and Exciton–Phonon Interaction in Two-Dimensional Colloidal CdSe Nanosheets. *Nano Lett.* **2012,** *12* (6), 3151-3157.

27. Jones, R. C., A Generalization of the Dielectric Ellipsoid Problem. *Phys. Rev.* **1945,** *68* (3-4), 93-96.

28. Vezzoli, S.; Manceau, M.; Leménager, G.; Glorieux, Q.; Giacobino, E.; Carbone, L.; De Vittorio, M.; Bramati, A., Exciton Fine Structure of CdSe/CdS Nanocrystals Determined by Polarization Microscopy at Room Temperature. *ACS Nano* **2015,** *9*, 7992–8003.

29. Empedocles, S. A.; Neuhauser, R.; Bawendi, M. G., Three-Dimensional Orientation Measurements of Symmetric Single Chromophores using Polarization Microscopy. *Nature* **1999,** *399* (6732), 126-130.

30. Diroll, B. T.; Dadosh, T.; Koschitzky, A.; Goldman, Y. E.; Murray, C. B., Interpreting the Energy-Dependent Anisotropy of Colloidal Nanorods Using Ensemble and Single-Particle Spectroscopy. *J. Phys. Chem. C* **2013,** *117* (45), 23928-23937.

31. Hadar, I.; Hitin, G. B.; Sitt, A.; Faust, A.; Banin, U., Polarization Properties of Semiconductor Nanorod Heterostructures: From Single Particles to the Ensemble. *J. Phys. Chem. Lett.* **2013,** *4* (3), 502-507.

32. Ithurria, S.; Tessier, M. D.; Mahler, B.; Lobo, R. P. S. M.; Dubertret, B.; Efros, A. L., Colloidal Nanoplatelets with Two-Dimensional Electronic Structure. *Nat. Mater.* **2011,** *10* (12), 936-941.

33. Miller, D. A. B., Optical Physics of Quantum Wells. In *Quantum Dynamics of Simple Systems*, G. -L. Oppo, S. M. B., E. Riis, and M. Wilkinson, Ed. Institute of Physics: London, 1996; pp 239-266.

34. Schmitt-Rink, S.; Chemla, D. S.; Miller, D. A. B., Linear and Nonlinear Optical Properties of Semiconductor Quantum Wells. *Advances in Physics* **1989,** *38* (2), 89-188.

35. Rizzo, A.; Nobile, C.; Mazzeo, M.; Giorgi, M. D.; Fiore, A.; Carbone, L.; Cingolani, R.; Manna, L.; Gigli, G., Polarized Light Emitting Diode by Long-Range Nanorod Self-Assembling on a Water Surface. *ACS Nano* **2009,** *3* (6), 1506-1512.

36. Hartmann, L.; Djurado, D.; Florea, I.; Legrand, J.-F.; Fiore, A.; Reiss, P.; Doyle, S.; Vorobiev, A.; Pouget, S.; Chandezon, F.; Ersen, O.; Brinkmann, M., Large-Scale Simultaneous Orientation of CdSe Nanorods and Regioregular Poly(3-hexylthiophene) by Mechanical Rubbing. *Macromolecules* **2013,** *46* (15), 6177-6186.

37. Stancil, K. A., Evaporation Assisted CdSe Nanorod Assembly by Small Angle X-ray Scattering and Langmuir Adsorption. *J. Phys. Chem. B* **2014,** *118* (50), 14695-14702.

2. Alignment of nanocrystal ensembles to determine efficacy in displays

2.1. **Introduction: Organizing ensemble arrays to achieve single particle properties**

Organizing nanorods into unidirectional arrays has been demonstrated previously using self-assembly,[1-4] block co-polymer directed assembly,[5] electric-field directed assembly,[5] electrospun nanofibers,[5] mechanical rubbing,[6] and mechanical stretching.[7-8] Recently, self-assembly of liquid crystals and photoinduced alignment have been utilized together to control unidirectional alignment of nanorods for polarized emission.[9] From the practical point of view, mechanical stretching would be easy to achieve for roll-to-roll processed films. Here we have achieved high quality macroscopically polarized emitting areas by dispersing various nanocrystal emitters in a suitable polymer film and mechanically stretching to induce alignment.

2.2. **Preparation of anistropic nanocrystal-in-polymer films with high optical quality**

The state of the art in LCD technology involves highly-emissive quantum dots encapsulated in a glass capillary or in a polymer medium.[10] Incorporation of polarized emitting structures necessitates not only integration into the existing QD-LCD technology but also efficient alignment of the structures to realize ensemble polarized emitting areas. We envisioned that nanorods could be dispersed in a suitable polymer film matrix and mechanically strained to align the rods under shear force of the polymer chains. Indeed, stretched films have been used as alignment media in polarizers and even have precedence in aligning ensembles of nanorods.[10-11]

2.2.1. Polymer Screening

To maximize brightness and macroscopic alignment of CdSe/CdS nanostructures, we sought a polymer medium which dispersed nanocrystals, had co-solubility in nonpolar organic solvents, and had a glass transition temperature (T_g) above room temperature. Such a medium

would allow us to obtain a composite with fixed alignment, suitable concentration, homogeneity and optical clarity. After screening a number of candidates (Table 2.1), poly(butyl-co-isobutyl methacrylate) (PBiBMA) was chosen for solubility in chloroform and toluene, combined with good visco-elasticity at relatively mild temperatures (T_g = 35 °C). In the case of NPLs, we payed special attention to prevent aggregation and NPL stacking by using freshly prepared solutions.

Table 2.1. Preliminary results of polymers tested for dispersion and stretching of composites.

Polymer	T_g (°C)	Description	Best Result Polarized Emission
poly (butyl methacrylate) (PBMA)	**15**	**Strong plastic film, resistant to stretching at RT; stretchable in 50 °C water bath**	**1.7:1**
poly (butyl-co-isobutyl methacrylate) (PBiBMA)	**35**	**Resistant to stretching at RT; stretchable in 60 °C water bath**	**2.3:1**
poly (benzyl methacrylate) (PBzMA)	**55**	**Brittle, difficult to delaminate from glass substrate even at elevated temperatures**	**N/A**
poly (cyclohexyl methacrylate) (PCyMA)	**83**	**Somewhat brittle, cracks easily when stretched at RT and over a heat gun**	**N/A**
polystyrene-block-polybutadiene-block-polystyrene (PSBS)	**N/A**	**Spongy rubber film; stretchable at room temperature; relaxes rapidly**	**1.4:1**

2.2.2. Optimized polymer-nanocrystal nanocomposites

Investigation was made into systems which had high dispersibility of nanorods, a T_g slightly above room temperature, and elastic behavior at elevated temperatures. After screening

many polymers, we found that poly(butyl methacrylate)-co-(isobutyl methacrylate) satisfied these requirements.

For typical film preparation, nanorods were added to a solution of 5% wt. polymer in chloroform. To a glass substrate (22 x 22 mm), ~0.5 mL of solution was added to cover the entire area. The chloroform was evaporated at room temperature and then placed under vacuum for 24 hrs once most solvent had evaporated. The resulting nanorod-polymer composites were then delaminated from the slide Freestanding films were placed between two Teflon clamps and stretched by hand after submersion in a warm water bath (50-60 °C). While held under unidirectional tension, the films were subsequently submerged in cold water to set their conformation. The films were often trimmed to isolate unidirectionally stretched region and stored below room temperature to slow thermal relaxation.

Dropcasting of polymer-nanocrystal solutions and subsequent drying yielded homogenous, optically clear free-standing films (Figure 2.1a). PBiBMA-heterostructure films were highly luminescent under UV excitation and maintained brightness after stretching at elevated temperatures (60-70 °C) (Figure 2.1b). High loading concentrations (20% wt. NCs with respect to PBiBMA) could be attained for samples without visible scattering, allowing for greater flexibility in obtaining the desired optical density and brightness (Figure 2.1c). Films were typically stretched by hand to about 200-300% the original free-standing lengths. In rare cases we were able to stretch the films >500% to obtain maximum degree of emission polarization but this typically caused damage to the films. It is imagined that such films could be seamlessly incorporated as a polarized re-emitting layer demonstrated in Figure 1.1.

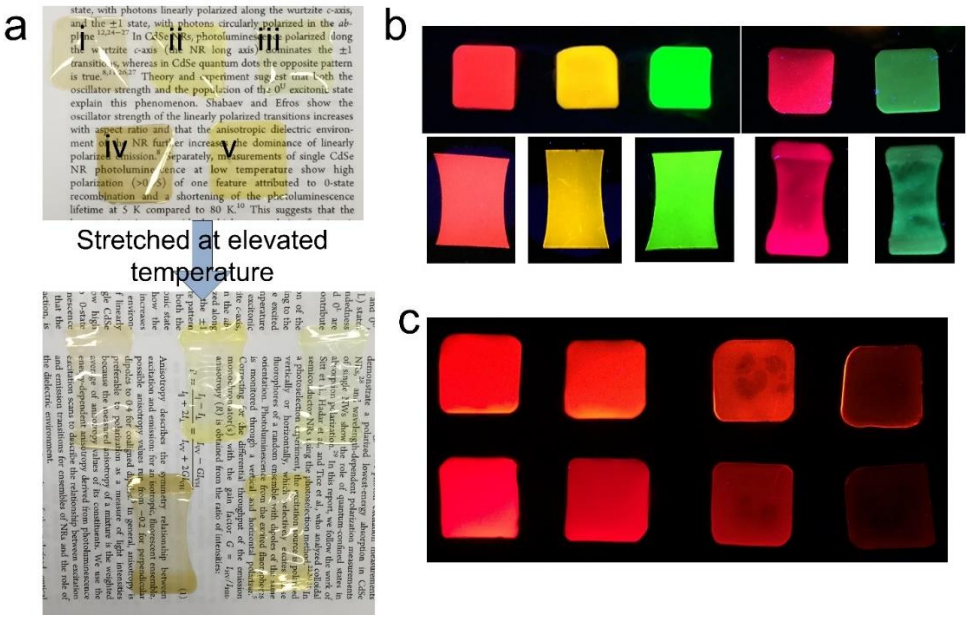

Figure 2.1. Luminescent nanomaterial-polymer composites consisting of luminescent nanocrystals dispersed in poly (butyl-co-isobutyl methacrylate). (a) Films under ambient light before and after stretching consisting of CdSe/CdS dot-in-rods: (i) 4.5 nm core, (ii) 3.8 nm core, (iii) 2.1 nm core; iv) CdSe/$Cd_{1-x}Zn_xS$ nanoplatelets, v) CdSe nanoplatelets. (b) Same films under ambient light before and after stretching. (c) Films of varying concentration under UV light. The top row of films consists of core-shell quantum dots and the bottom row of films consists of similar concentrations of CdSe/CdS rod-in-rods.

2.3. **Alignment of nanorods inside polymer films**

In order to understand the nature of nanorod alignment with respect to stretching, film samples were investigated using small angle X-ray scattering (SAXS) collected at the Advanced Light Source at Argonne National Lab

2.3.1. Quality and alignment with respect to concentrations of films

In pure PBiBMA film samples, no features were observed except diffuse background scattering before and after stretching (Figure 2.2a-b). In non-stretched films, nanorods are randomly oriented (Figure 2.2c, e, and g). In low and intermediate concentration films, the dispersion of nanorods is uniform (Figure 2.2c); whereas superstructure formation occurs as nanorod concentrations are increased (Figure 2.2e and g). Such superstructures most typically

included stacks of aligned nanorods. Strong unidirectional alignment is observed after stretching of composite films at several concentrations as evidenced by slower decay of scattering intensity in the direction normal to polymer stretching (Figure 2.2d, f, and h).

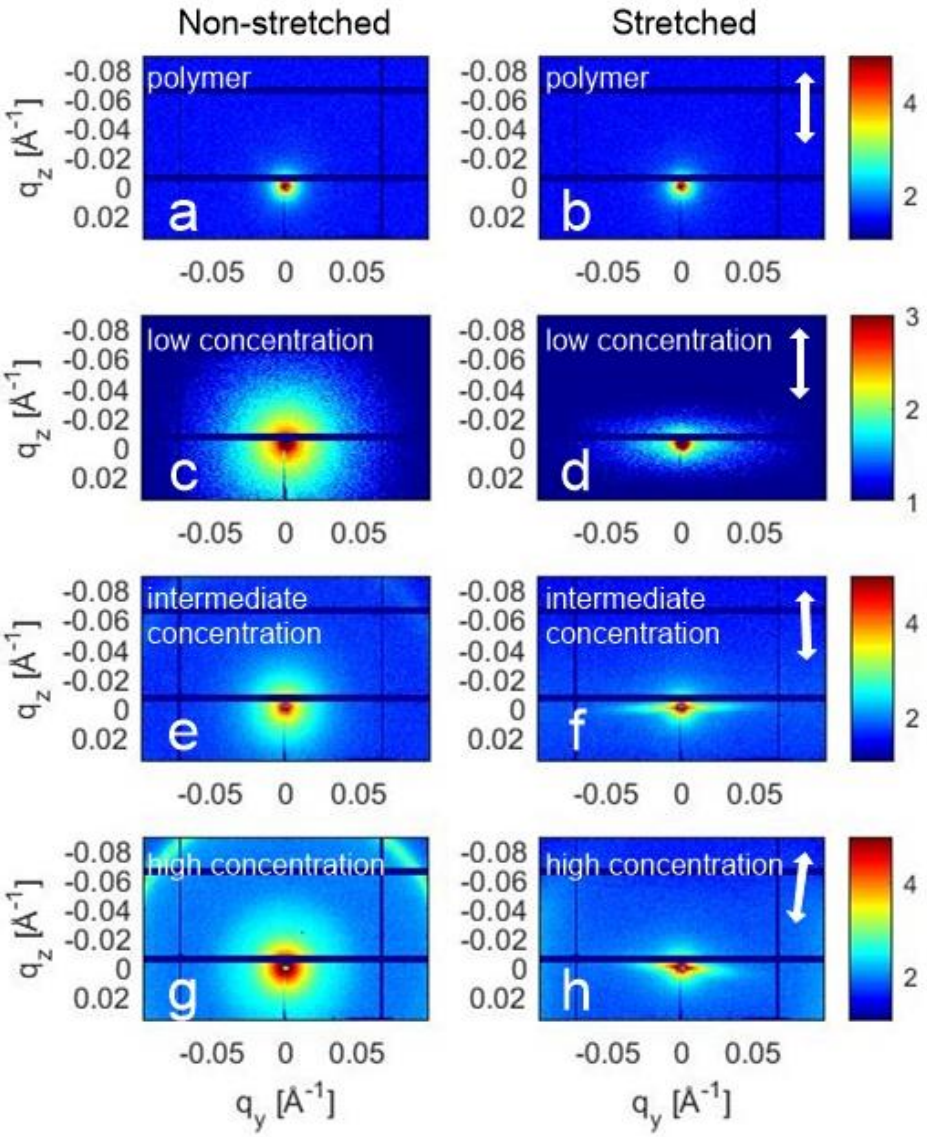

Figure 2.2. Small-angle X-ray scattering intensity maps measured from the luminescent CdSe/CdS nanorods (3.5 x 9.0 nm; 2.1 nm core) dispersed in poly (butyl-co-isobutyl methacrylate). (a,b) Pure polymer films before and after stretching along the direction shown by the arrow. (c,d) CdSe/CdS nanorods dispersed at low concentration in non-stretched and stretched polymer films, respectively. (e-h) As the concentration of dispersed CdSe/CdS nanorods increased, ordered domains, likely with smectic ordering of nanorods, formed in both non-stretched and stretched polymer films.

2.3.2. Effects of additives on dispersibility and alignment

The addition of small amounts of long chain organics was explored to determine the effect on alignment and dispersability in polymer films (Figure 2.3). The additive n-octylamine helped improve disperability of nanorods but this additive was detrimental to alignment. The addition of n-trioctylphosphine maintained alignment but a larger presence of aggregates was observed and confirmed with SAXS.

Films were prepared using the same batch of CdSe@CdS nanorods to determine the effect of additives on dispersibility and alignment. Films additives were used as 1.5% wt. of n-octylamine (OctAm) and 1.5% wt. of n-trioctylphosphine (TOP). Qualitatively, the films containing TOP maintained their bright color but appeared cloudy, whereas films with no additives and OctAm were optically clear. The SAXS patterns from the resulting films indicated that samples prepared with TOP had aggregates, whereas films with no additives had fewer and films with OctAm appeared to have almost none (Figure 2.3). After stretching, the nanorods w TOP are much more strongly aligned and have small orientation angles. The nanorods with no additives present are still well aligned, whereas those with OctAm show weaker alignment. It is possible that in the presence of octylamine the interaction of nanorods with the polymer brush is minimal. The presence of aggregates in the film with TOP could be responsible for an increase in alignment due to cooperative effects.

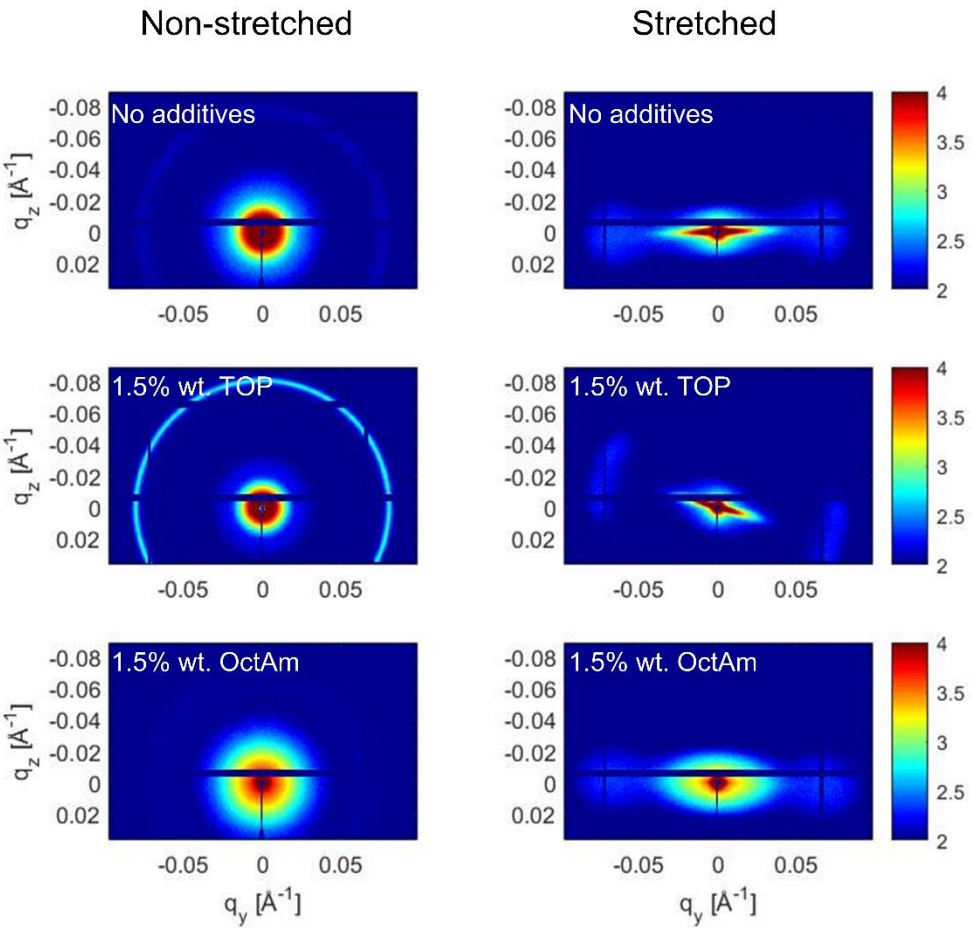

Figure 2.3. SAXS patterns of films before and after stretching with different additives. Clear differences in intensity and orientation are seen in each case.

2.3.3. Quantifying the order of nanorods in polymer films

We sought to quantify the ordering of nanorods within the polymer films by making analogy with determination of orientation factor in uniaxially oriented semi-crystalline polymer systems. To quantify the orientation, the Hermans orientation factor (S_{or}) is used and defined as follows:[12]

$$S_{or} = \frac{3\langle \cos^2 \Phi \rangle - 1}{2} \quad (4)$$

Where Φ represents the azimuthal angle of the scattering pattern—in this case it is representative of the angle perpendicular to the alignment axis. Thus for a system ordered perfectly parallel to

the alignment axis we should expect to see an orientation factor of 1 and for a disordered system we should expect to see a value of 0. From each SAXS pattern we can generate an azimuthal intensity profile, $I(\Phi)$, by measuring the scattering intensity for a fixed radius, |q|. The intensity profiles were fit with Lorenztian functions and used to calculate the $\langle \cos^2 \Phi \rangle$:

$$\langle \cos^2 \Phi \rangle = \frac{\int_{\Phi_1}^{\Phi_2} I(\Phi) \cos^2 \Phi \sin \Phi d\Phi}{\int_{\Phi_1}^{\Phi_2} I(\Phi) \sin \Phi d\Phi} \quad (5)$$

This calculation of orientation factors was used to compare aligned film containing CdSe/CdS nanorods with different sizes and aspect ratios (Figure 2.4a-c). Anisotropic particles are expected to align with respect to the stretching direction under shear force from the polymer chains. We found that small nanorods measuring 3.5 x 9.0 nm in diameter consistently demonstrated the best alignment with an orientation factor of 0.87 while larger nanorods of similar aspect ratio (6 x 19 nm) had an orientation factor of 0.82. Nanorods measuring 35 nm in length and 5 nm in diameter (aspect ratio ~7) exhibited less efficient alignment (Figure 2.4b and c, bottom). This somewhat counterintuitive result can be explained if we consider that larger force and more extensive displacement of polymer chains is required to align larger rods along the stretching direction. Hence, it is likely that the most efficient alignment of an ordered array requires that particles have a relatively small aspect ratio to efficiently respond to the mechanical force of polymer chains. Luckily, nanorods with modest aspect ratios are also optimal for achieving high quantum yield.

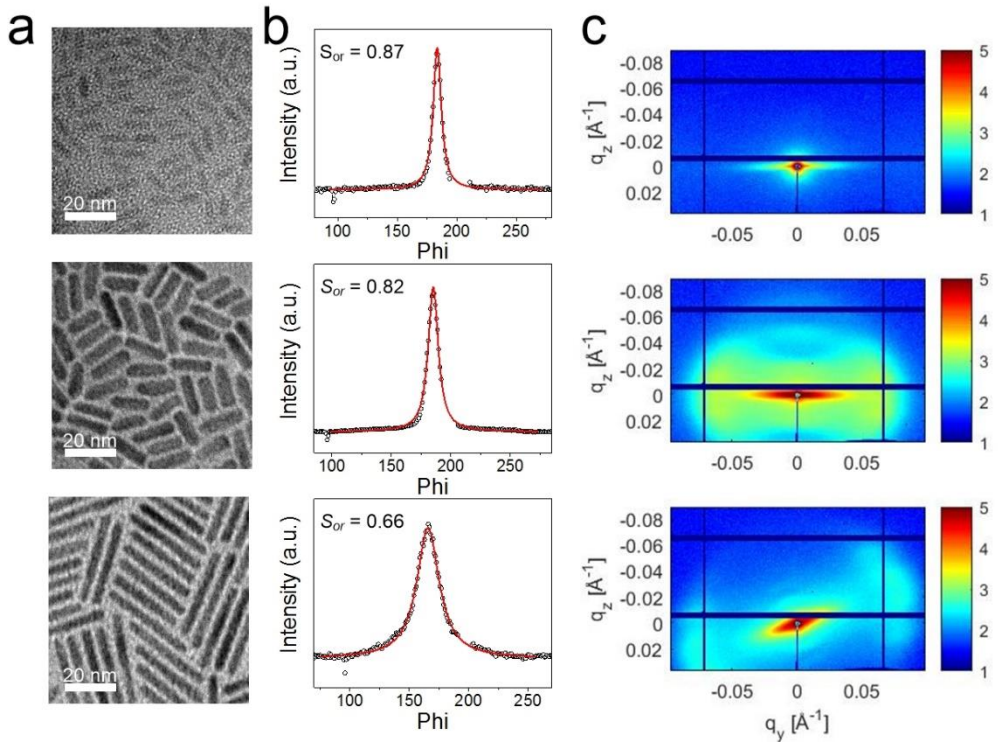

Figure 2.4. Effect of nanorod size and aspect ratio on alignment efficiency in PBiBMA-NR composite films. (a) TEM images of CdSe/CdS nanorods of with increasing size and aspect ratio. Scale bars are 20 nm. (b) Orientation factors (S_{or}) extracted from the $\langle\cos^2 \Phi\rangle$ of the circular-line integrals of two-dimensional SAXS patterns (c) measured from stretched films of each sample fitted with Lorentzian functions. In all cases, stretching of films was ~200%.

2.3.4. Lack of clear ordering in NPL GISAXs

Three types of nanoplatelets were used with similar concentrations. Each sample had a stretched and double-stretched counterpart to probe the alignment of nanoplatelet faces. Non-stretched films were trimmed from stretched samples, so there was no control for the residual force of the clamping and pulling of the sample. Double stretched films were done from duplicate sample prep for the single stretched films. In general, the same trend is observed across each type of nanoplatelets. The anisotropy of the scattering pattern is greater as films go from as prepared, to uniaxial, to biaxial stretching (Figure 2.5). Control samples all appear similar, with a slight oblate shape. It is unclear whether this is due to preferential alignment happening during dropcasting or

an artifact of the beamstop. uniaxial films have a double peak forming a cross about the beam center. It is likely that is observation indicates alignment along the longest axis, which would lead to a random distribution of edges and faces with respect to the film surface. In double stretched films, the feature is washed out and the peaks become narrower. This trend is exemplified by the normalized Lorenztian fits of the azimuthal linecuts for the 512 NPL sample (Figure 2.6).

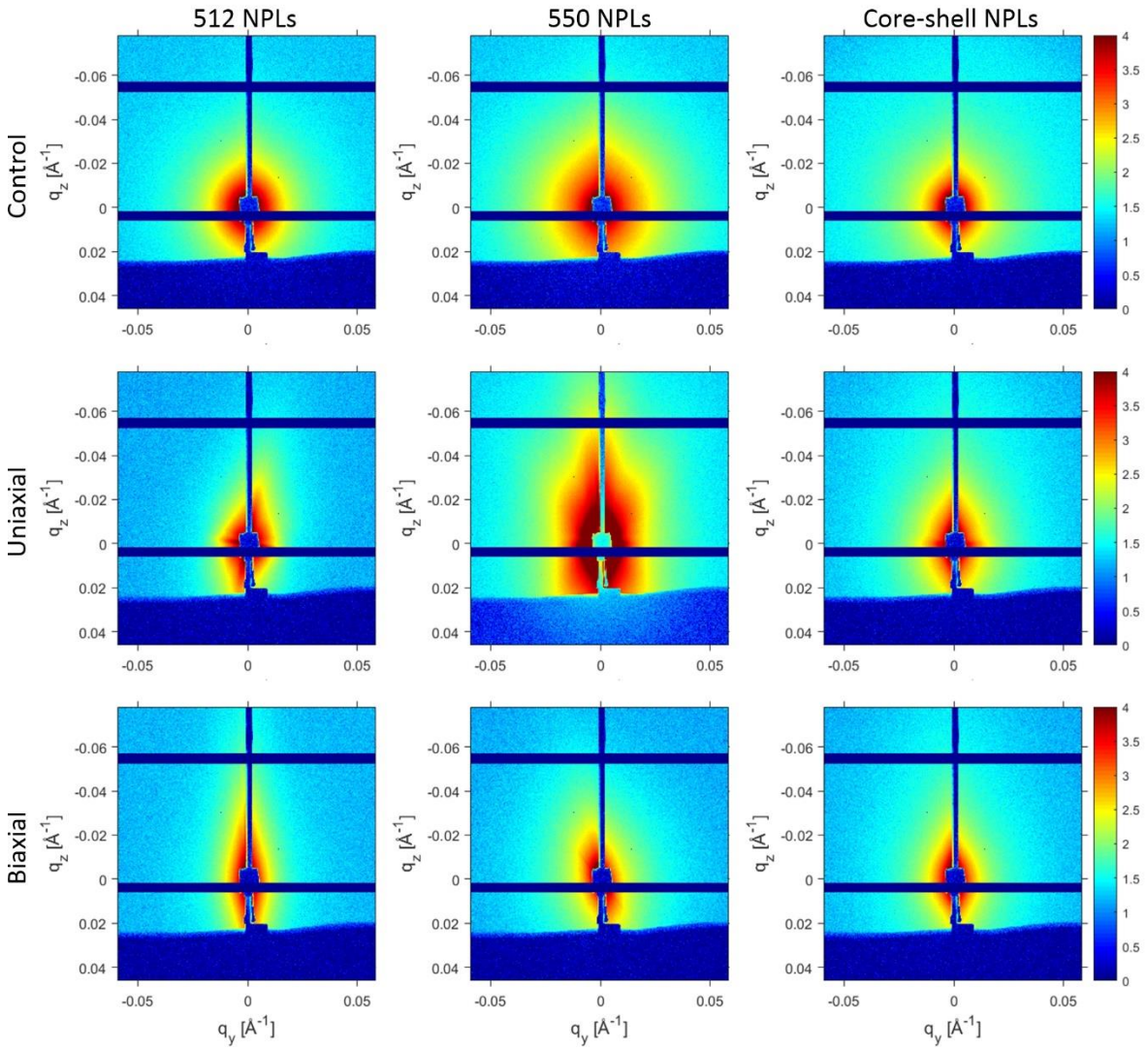

Figure 2.5. GISAXS pattern of 512, 550 and core-shell nanoplatelet films under different stretching conditions.

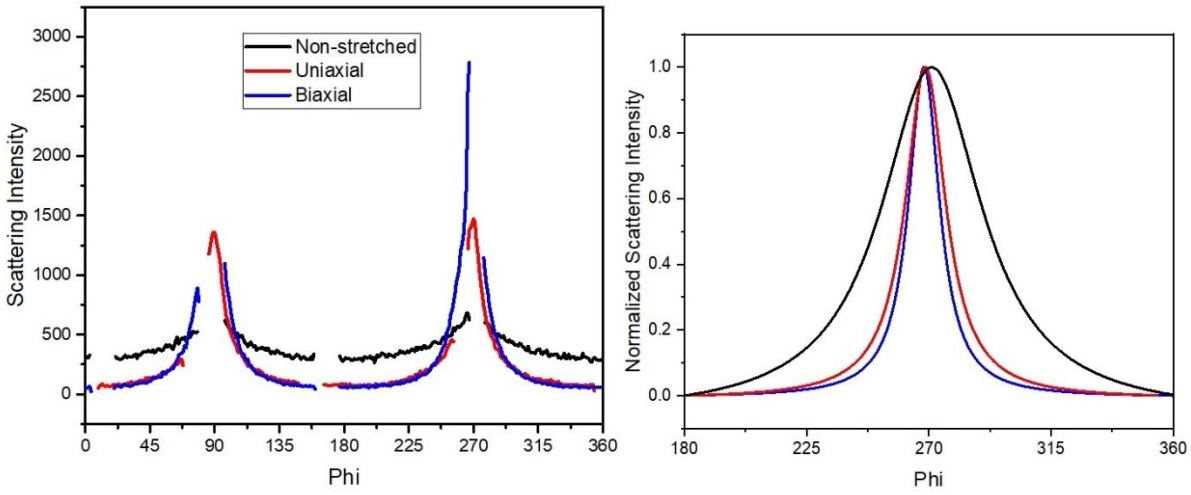

Figure 2.6. Analysis of NPL alignment from GISAXS pattern: (a) Azimuthal linecuts of 512 NPL samples. Missing data comes from the beam stop and the mask. (b) Normalized Lorentzian fits demonstrating the change in peak width with respect to different degrees of stretching.

2.4. **Absorption polarization of aligned anisotropic nanostructures**

2.4.1. Methods and errors in polarized film absorption

For measurement of absorption of polarized light, we used a Glan-Taylor Polarizer to filter out light from the UV-Vis lamp in the Cary 5000. To assure that any polarization response we measured was not an artifact, we measured the polarization dependence of an isotropic emitting film sample. The error in optical density was 0.003 throughout the spectra, leading to a larger percent error at lower optical density regions (Figure 2.7).

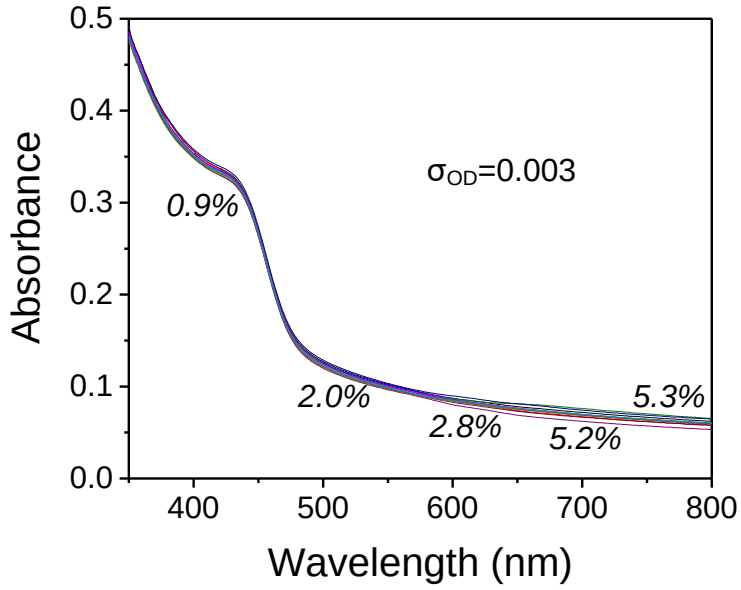

Figure 2.7. Error propagation in optical density for measurement of polarized absorbance at angles between 0-90.

2.4.2. Physical understanding of absorption anisotropy

Film absorption was used to determine the relative anisotropy of absorption. In order to probe the absorption by an array of aligned nano-heterostructures, we measured the absorption of polarized light by collecting absorption spectra for different polarization angles.[13] CdSe/CdS dot-in-rods are expected to have a perfectly anisotropic dipole moment at the first exciton with no absorption for light polarized perpendicular to the c-axis.[13] From our experimental measurements, dot-in-rods and rod-in-rods have strongly polarized transitions at the band edge with a polarization dependence that persists at higher energies due to dielectric effect of the anisotropic CdS shell (Figure 2.8a-b). To some surprise, we also found that NPLs show absorption polarization though less extreme than that of nanorod heterostructures (Figure 2.8c). Weak absorption anisotropy of ~0.13 in CdSe QDs was also measured for band-edge and high energy excitation (Figure 2.8d). It can be explained by small deviations from perfectly spherical

shape typical for wurtzite CdSe QDs.[13] Weak optical anisotropy of stretched films can also be explained by alignment of small aggregates that introduce anisotropic dielectric screening (Figure 2.9). We can see that for all of the anisotropic Cd based nanostructures, the highest absorption anisotropy is observed at the band edge, with the anisotropy being markedly lower at blue excitation wavelength (Figure 2.8d). Based on our relationship between emission and absorption anisotropy (Eq. 1.2), it is expected that if emission anisotropy remains fixed and the decrease in absorption anisotropy leads to the decrease in net optical anisotropy.

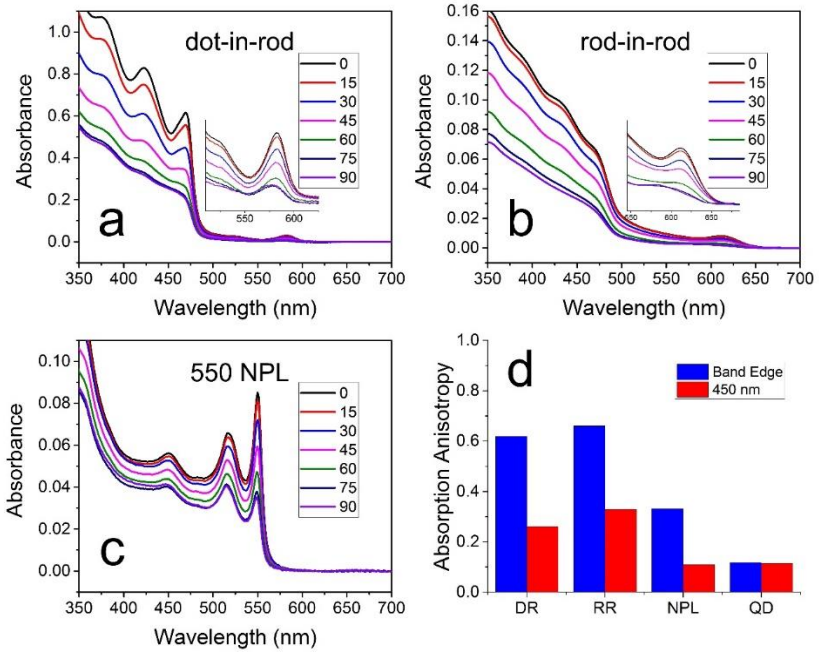

Figure 2.8. Absorption of polarized light for anisotropic nanoheterostructures aligned in stretched PBiBMA films: (a) CdSe/CdS dot-in-rods; (b) CdSe/CdS rod-in-rods; (c) CdSe NPLs. (d) Comparison of absorption anisotropy, *r*, as measured by absorption of incoming polarized light at the first excitonic maximum and practical excitation wavelength (450 nm). In this case, QDs are CdSe cores. The error in the collection of polarized absorption is shown in Figure 2.7.

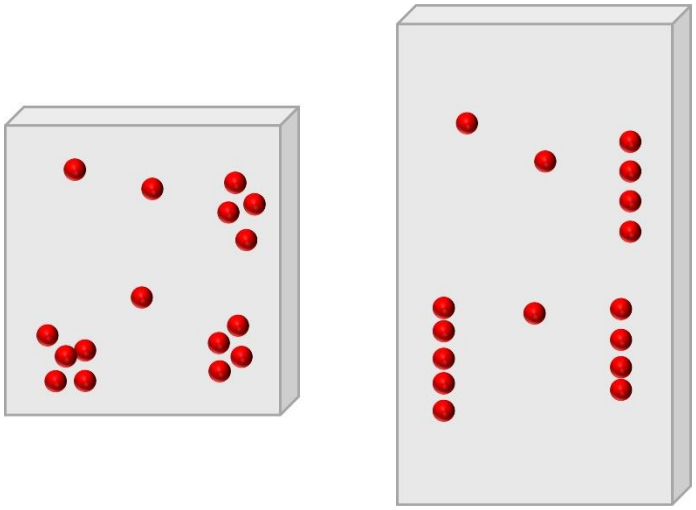

Figure 2.9. Representation of origin of dielectric screening of aggregates with respect to stretching of spherical quantum dot films.

2.5. **Emission polarization of anisotropic nanostructures in stretched polymer films.**

For display applications, the emission polarization of the emitting layer should be sufficiently high at excitations between UV and blue. Emission polarization of stretched films was measured using an optical setup with blue unpolarized excitation.

2.5.1. Measurement techniques for polarized emissions

A modified microscope (Olympus BX51) was used to measure polarized emissions (Figure 2.10). White light sources (halogen lamps) were used for excitation, but a laser was available for excitation when needed. The measurement can be done by collecting either the reflected/scattered emission (front-face excitation) or transmitted emission (back-face excitation). In a typical measurement of the transmitted emission, a blue excitation beam is created using a short-pass filter (cutoff at 492 nm) to filter the white light, and is then focused on the sample. The transmitted light passes through a polarizer before being collected by an objective. The collected light is filtered by a bandpass filter (580–660 nm), and is then sent into a spectrometer (QEPro, Ocean Optics). Proper bandpass filters are chosen for nanorods emitting in

different spectral regions. Polarized emissions can then be measured by adjusting the polarizer angle in the emission path. Another polarizer can be placed in the excitation beam path to control the excitation polarization. The relative polarization of excitation and emission can thus be controlled by adjusting the relative angles of the two polarizers.

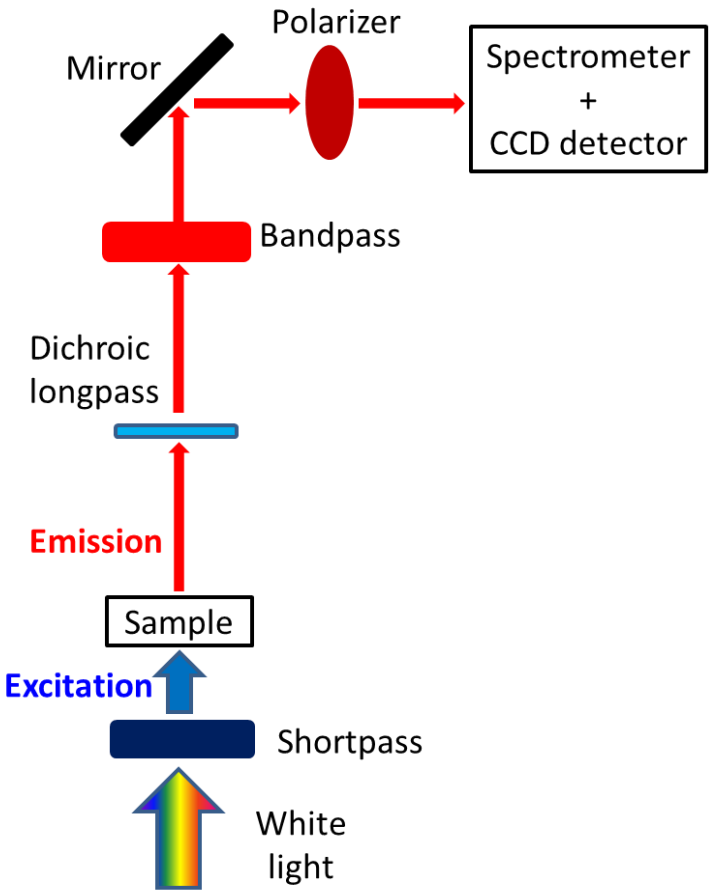

Figure 2.10. Schematic of optical microscope used in measurements of ensemble polarized emissions.

Mapping of emission polarization was performed using a microscope (Olympus IX83) with an anisotropy module (DV2 Lambda, Photometrics). Film samples were excited with polarized blue light (402/15 nm) and emission was monitored through an objective (60x, 0.65 NA) at the target wavelength (632/60 nm). The emission beam was split and directed through

parallel and perpendicular polarizers where it was detected by a CCD camera (Evolve 512 Delta, Photometrics). Polarization is calculated using two images obtained under parallel and perpendicular photoselection, corrected to account for emission depolarization caused by microscope objective.

2.5.2. Degree of polarized emission in nanorod composites

In general, the sample was excited with white light passing through a shortpass filter (blue) and the film emission passed through a polarizer filter and was collected by a spectrometer. Normalized degree of linear polarization (DOLP) is defined as $(I_{\parallel} - I_{\perp})/(I_{\parallel} + I_{\perp})$, where the intensities represent integrated areas of the emission peaks from samples excited by unpolarized light and filtered at varying polarizer angles. The $I_{\parallel}$ is defined as the area of the PL peak measured at polarization along the stretching direction and $I_{\perp}$ is defined as the area at an angle 90 degrees away. One can also relate these two parameters as a contrast ratio (CR), defined as $I_{\parallel}/I_{\perp}$. Figure 2.11a demonstrates the polarization dependence of an aligned sample of CdSe/CdS dot-in-rods; for stretched films, the measured DOLP is 0.6, whereas the measured polarization dependence for a non-stretched film is ±0.05. In dot-in-rod samples, we achieved a CR approaching 4:1 (Figure 2.11b), while for rod-in-rods CR approached 5.6 (Figure 2.11c). The electronic transitions of nanorods should be strongly polarized, with reported single particle DOLP reaching 0.83 for rod-in-rods.[14] Such arrays of nanorods begin to approach single particle values and the chief limitation of polarization approaching single-particle values is the distribution of orientation within the stretched film. Optical data also appeared to be strongly correlated with the degree of alignment in the case of nanorods—as expected, films prepared using the same nanorods had higher contrast ratios when the angular distribution of aligned nanorods was smaller (Table 2.2). Samples with larger diameter fractions of CdSe core material

are predicted and shown to have a greater optical anisotropy and emission polarization.[15] Between sufficiently aligned samples of differing compositions, films containing nanocrystals with the greatest diameter fraction of CdSe demonstrated the highest polarization despite being less efficiently aligned (Table 2.2).

2.5.3. Polarized emission in NPLs

Emission polarization with a CR of 2.5 was achieved for a stretched film containing CdSe NPLs (Figure 2.11d). Although less susceptible to efficient alignment, these NPLs still demonstrate photoluminescence polarization. Aligned arrays of NPLs could be used to achieve polarized light emission with extremely narrow spectral width. It is likely that the stretching force aligns nanoplatelets about their longest axis with a random distribution of "face out" and "edge out" normal to the film. The combination of TE modes, with linearly polarized emission from the edges and elliptically polarized emission from the faces, likely contributes to a macroscopic elliptically polarized emission in stretched NPL films.

[more about NPLs]

2.5.4. Possibility of aggregation-induced polarization

It is not possible to rule out the formation of superstructures—structures like this have been seen in NRs and NPLs alike.[15] Systematic alignment and polarization due to long-range superstructure formation would be revealed by the SAXS pattern. As nothing is seen beyond small aggregation, it is likely that the majority of the polarized emission is due to the efficient alignment of well-spaced anisotropic emitters. To further probe the distribution of these polarized emitting films, we characterized nanorod film microstructure by mapping the emission polarization of nanorods in polymer matrix (Figure 2.11e). The polarization map of an area of non-stretched film indicates a disordered sample with some possible areas of aggregation

indicated by non-zero values (Figure 2.11e). In stretched films, the polarization is high throughout the sample, with local minima of polarization indicating the presence of some higher concentration areas which are off-axis after stretching (Figure 2.11e).

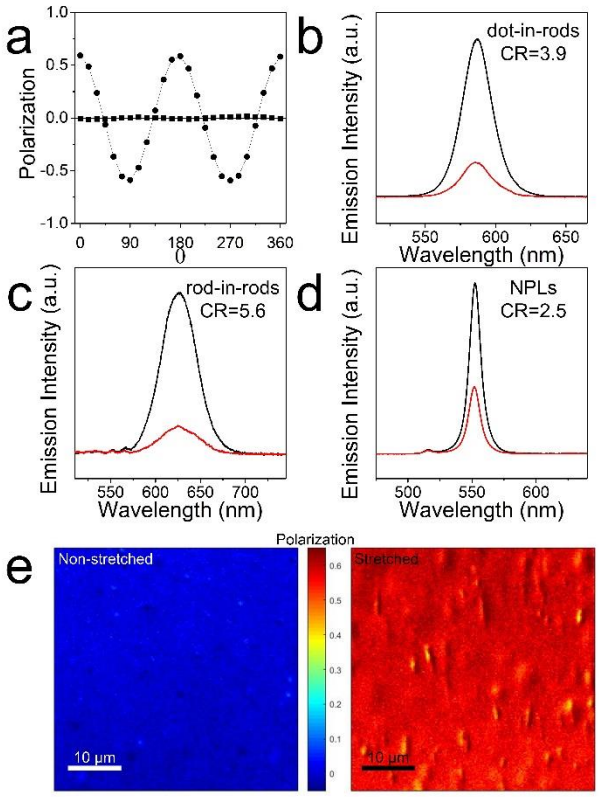

Figure 2.11. Polarized photoluminescence from stretched film composites. (a) Polarization dependence of emitted light for samples of CdSe/CdS dot-in-rods before (squares) and after (circles) stretching. (b-d) Emission with polarization photoselected parallel (black curves) and perpendicular (red curves) to the direction of stretching for three types of nanocrystals: dot-in-rods (35 x 5 nm; 3.5 nm core), rod-in-rods (5.2 x 45 nm; 3.8 x 9.0 nm core), and CdSe NPLs. (e) Mapping of fluorescence polarization for ~10^3 μm^2 areas of polymer films containing rod-in-rods before and after alignment.

Table 2.2. Summary of SAXS alignment data compared with emission polarization data

Sample ID	Dimensions of NR (nm)	S_{or}	CR	DOLP	Core Size (nm)
pdc1052	**6.5 x 12**	**0.81**	**1.93**	**0.32**	**2.3**
jp29	**3.5 x 9.0**	**0.81**	**2.39**	**0.41**	**2.1**
pdc1030	**5.1 x 35**	**0.72**	**3.91**	**0.59**	**3.8**

2.5.5. Thermal stability of polymer-nanocrystal composites

The thermal stability of these polymer films is crucial for aligned polarized emitting films due to the high local temperatures within LCD displays. We found that contrast ratios were maintained even after aging films at high temperatures well above T_g for several days (Figure 2.12). The use of polymers with higher T_g than that of PBIBMA should fully address the problem of NR misalignment at operating temperatures within an LCD stack.

A high concentration nanorod-PBiBMA composite was prepared using our typical procedure for dropcasting polymer films. The resulting film was stretched at elevated temperatures and photoselected emission spectra were recorded. The film was then placed between two glass slides and wrapped with foil and placed on a hotplate set to 90 °C. The internal temperature is estimated to be 60 °C. The film was left to age for 1 day and its emission spectra were recorded again. The film was then placed on a hotplate in the same fashion and left at an internal temperature of 100 °C for 5 days (hotplate = 130 °C). The spectra were again recorded and the appearance was noted.

After one day at mild conditions, a slight change in visible appearance was observed—the color went from slightly opaque orange to a clearer yellow. The polarization of the sample was mostly maintained with the contrast ratio decreasing from 2.75 to 2.65. After nearly a week at the harsher conditions, the film appeared to form domains where there were likely minor changes in thickness due to melting and reforming. The contrast ratio only drops to 2.22 in this case. At such harsh conditions, the alignment of nanorods is only slightly perturbed.

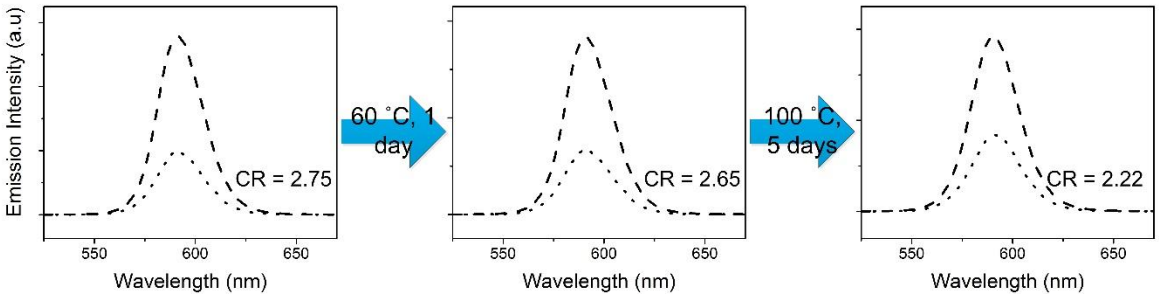

Figure 2.12. Emission spectra of stretched film of CdSe@CdS nanorods in polymer thermally aged over 6 days. Emission spectra were obtained with no photoselection (solid), polarized parallel to stretching axis (dashed), and polarized perpendicular to stretching axis (dotted).

2.6. **Directional emission from anisotropic nanostructures in stretched polymer films.**

Anisotropic nanostructures can emit photons with different probability in different directions. Understanding the directionality of light emission by anisotropic nanostructures is key for achieving efficient macroscopic polarized emitting films.

Our optical setup (Figure 2.13) was designed such that we collected emission spectra at different elevational and azimuthal angles (Figure 2.14a). The directionality of emission intensity was measured to determine the angular distribution of emission as well as any anisotropy in the directional intensity. Interestingly, in comparison with the non-stretched film which is isotropic, the stretched film demonstrates a less intense drop off in intensity (Figure 2.14b). In CdSe/CdS nanorods, the orientation of the transition dipole causes emission to propagate normal to the long axis of the nanorod, whereas emission parallel to the long axis is weak (Figure 2.14a). These far-field emission properties arise from the 1D polarization present in nanorod transitions. Conservation of angular momentum during electron-hole recombination requires emitted photon to propagate normal to the long axis of nanorod. Thus, the propagation of light occurs primarily in a cone along a plane perpendicular and bisecting the alignment (long) axis of the ensemble of nanorods; this anisotropy in distribution is consistent with our hypothesis of the increased

brightness due to stretching alignment. This cone of emission is likely useful in many flat panel display applications due to the majority of viewing being done at wide angles horizontally as opposed to vertically. We now know that this effect would be stronger NPLs with electronic structure of quantum wells, with both single particles and ensembles demonstrating nearly all of their emission normal to their flat planes.[16-17]

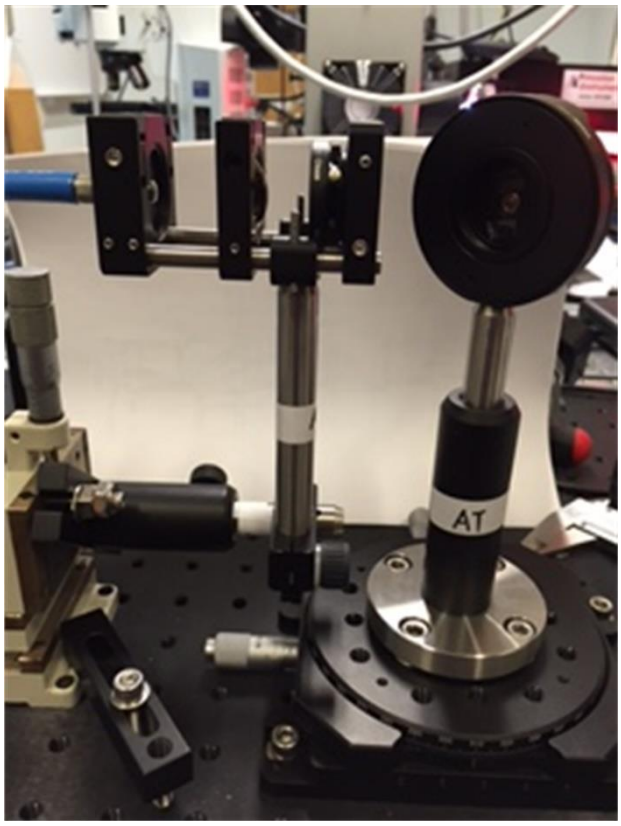

Figure 2.13. Optical setup for measuring directionality of emission in films. Film is excited from behind the sample and the holder has two rotational degrees of freedom at the base and the head. Emission is collected through focused collection optics.

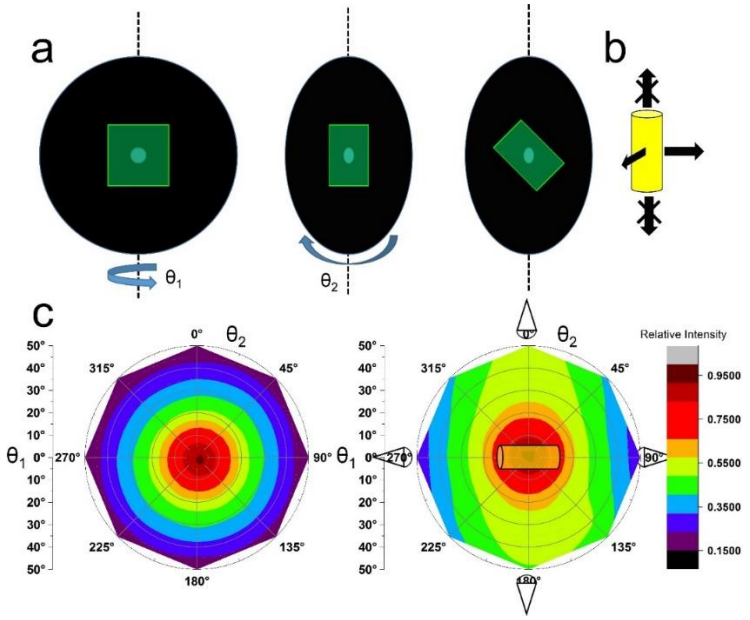

Figure 2.14. Directionality of emission in stretched nanorod films: (a) Scheme of sample holder and angular variables in our measurement setup. The detector is focused or slightly overfocused on the excitation spot and emission spectra are collected for several data points. (b) Theoretical emission directions for nanorod and nanoplatelet films. (c) Intensity profile of a film of rod-in-rods (5.2 x 45 nm; 3.8 x 9.0 nm core) before and after stretching demonstrated by a single rod as the ideal aligned film.

2.7. **Brightness enhancement in stretched nanocrystal-polymer composite films**

The ability of the polymer films containing aligned nanostructures to efficiently absorb unpolarized light and re-emit polarized light determines their utility for LCD applications. We sought to compare brightness of films before and after stretching in order to quantify the efficiency of stretched *versus* non-stretched films. Based on the directionality experiments we expected to see an anisotropic direction of emission from an aligned film of nanorods (Figure 2.15a). For a sample of nearly spherical core-shell QDs we saw minimal change in the overall brightness with respect to stretching (Figure 2.16). The small DOLP can be explained by a slight shape anisotropy of core-shells that would likely allow them to be preferentially aligned and emit polarized light due to non-zero optical anisotropy (Figure 1.9). The normalized brightness of

films, estimated by the emission intensity as a function of the film optical density, was shown to significantly increase with respect to stretching of nanorod films (Figure 2.15b). After stretching, a sample of dot-in-rods had a normalized emission which was 100% greater than that of its non-stretched counterpart (Figure 2.15b). It should be noted that applying the same normalization constants to samples of non-stretched films and isotropic emitters yield curves which overlapped with less than 5% error (Figure 2.17). Such an increase is likely achieved through more efficient absorption and emission pathways—the dot-in-rods being laid flat along the film surface emit more photons normal to the film surface. These photons are more likely to escape the film without internal reflections. It has been imagined that such directionality could serve to eliminate brightness enhancement films (BEF) and additional reflecting optics which serve to provide recycling of light not aligned with the polarizer filter.

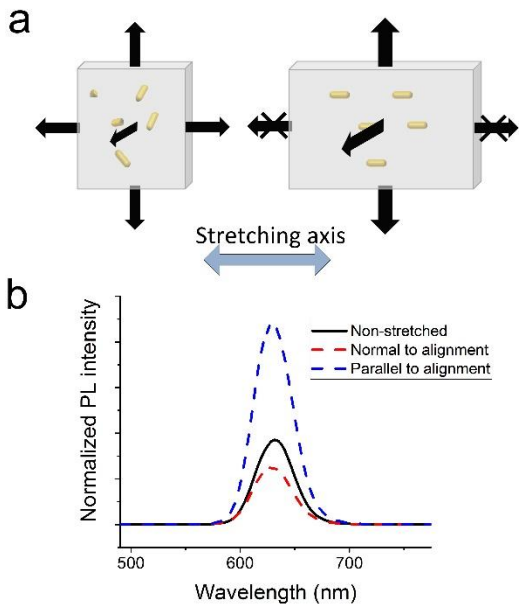

Figure 2.15. Directionality of emission after stretching alignment of CdSe/CdS nanorods: (a) Pictorial schematic of proposed mechanism. Film emission normalized to optical density with respect to non-polarized light of films before and after alignment of (b) CdSe/CdS rod-in-rods (5.2 x 45 nm; 3.8 x 9.0 nm core). Films were excited with unpolarized blue light and emission was measured normal to the film surface. Solid curve represents non-stretched film with random orientation of nanorods, with emission photoselected parallel (blue dashed) and perpendicular

Figure 2.15, continued. (red dashed) for aligned films. The normalization also factors in the optical density of the polarization filter to relate the brightness of the non-stretched component.

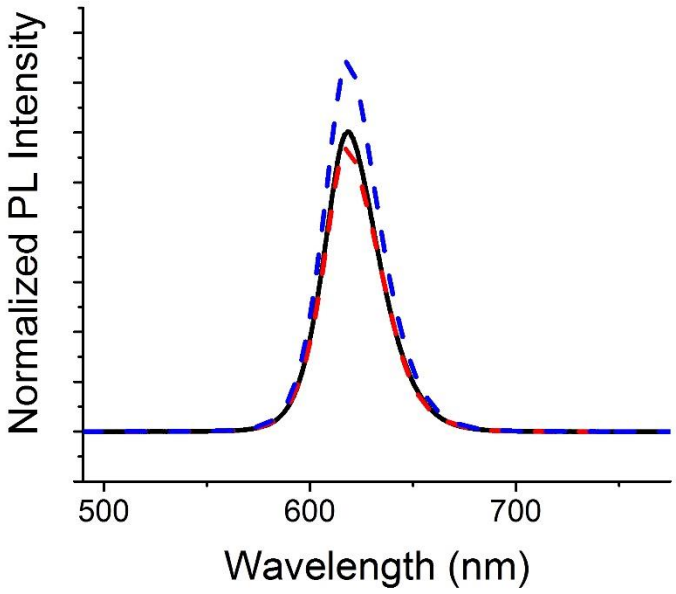

Figure 2.16. Film emission normalized to optical density with respect to non-polarized light of films before and after stretching for nearly spherical CdSe/CdS core-shell QDs. The optical anisotropy measured in solution for these QDs is shown in Figure 1.9.

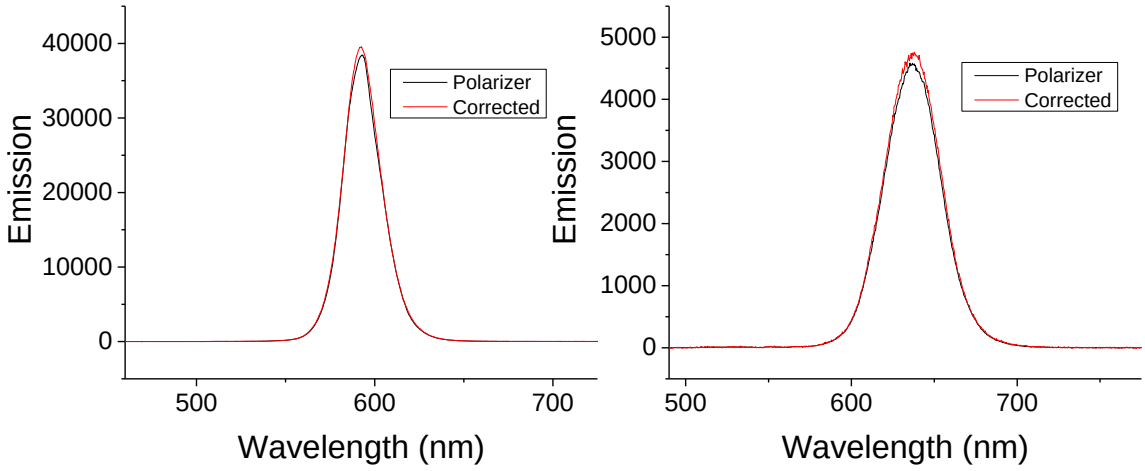

Figure 2.17. Comparison of isotropic emitting films containing disordered CdSe@CdS dot-in-rod nanostructures. Polarizer filters were placed atop films and resulting spectra were compared to those without a polarizer filter but corrected with a factor representing the transmittance of the polarizer filter.

2.8. **Conclusions**

Our results discuss the benefits of anisotropic nanostructures for LCD backlighting panel. Uniaxially aligned nanostructures with nanorod and nanoplatelet geometry provide a clear advantage as an active layer for LCD backlighting and other optoelectronic devices. Stretched polymer films can efficiently align CdSe/CdS dot-in-rod and rod-in-rod nanostructures and show more than two-fold enhancement of brightness compared to the emitter layers with randomly oriented nanostructures. This effect can be explained as the combination of linearly polarized luminescence and directional emission of individual nanostructures. The fabrication of these films for use as emissive layers could not only increase efficiency of the current quantum-dot based LCDs *via* polarized emission but also simplify the device architecture by improving directionality of photons. It is imagined that efficient use of nanomaterials with directional emission could improve the performance of other systems such as luminescent solar concentrators,[18-20] optical gain media for amplified spontaneous emission and lasing,[21-23] and light-emitting diodes.[24-25]

The following two chapters were published as an article in ACS Nano.[26]

2.9. **References**

1. Li, L. S.; Alivisatos, A. P., Semiconductor Nanorod Liquid Crystals and Their Assembly on a Substrate. *Adv. Mater.* **2003,** *15* (5), 408-411.

2. Ploshnik, E.; Salant, A.; Banin, U.; Shenhar, R., Hierarchical Surface Patterns of Nanorods Obtained by Co-Assembly with Block Copolymers in Ultrathin Films. *Adv. Mater.* **2010,** *22* (25), 2774-2779.

3. Thorkelsson, K.; Nelson, J. H.; Alivisatos, A. P.; Xu, T., End-to-End Alignment of Nanorods in Thin Films. *Nano Lett.* **2013,** *13* (10), 4908-4913.

4. Ryan, K. M.; Mastroianni, A.; Stancil, K. A.; Liu, H.; Alivisatos, A. P., Electric-Field-Assisted Assembly of Perpendicularly Oriented Nanorod Superlattices. *Nano Lett.* **2006,** *6* (7), 1479-1482.

5. Aubert, T.; Palangetic, L.; Mohammadimasoudi, M.; Neyts, K.; Beeckman, J.; Clasen, C.; Hens, Z., Large-Scale and Electroswitchable Polarized Emission from Semiconductor Nanorods Aligned in Polymeric Nanofibers. *ACS Photonics* **2015,** *2* (5), 583-588.

6. Du, T.; Schneider, J.; Srivastava, A. K.; Susha, A. S.; Chigrinov, V. G.; Kwok, H. S.; Rogach, A. L., Combination of Photoinduced Alignment and Self-Assembly to Realize Polarized Emission from Ordered Semiconductor Nanorods. *ACS Nano* **2015**.

7. Talapin, D. V.; Steckel, J., Quantum Dot Light-Emitting Devices. *MRS Bull.* **2013,** *38* (09), 685-691.

8. Pérez-Juste, J.; Rodríguez-González, B.; Mulvaney, P.; Liz-Marzán, L. M., Optical Control and Patterning of Gold-Nanorod–Poly(vinyl alcohol) Nanocomposite Films. *Adv. Funct. Mater.* **2005,** *15* (7), 1065-1071.

9. Peng, X.; Manna, L.; Yang, W.; Wickham, J.; Scher, E.; Kadavanich, A.; Alivisatos, A. P., Shape Control of CdSe Nanocrystals. *Nature* **2000,** *404* (6773), 59-61.

10. Page, K. A.; Landis, F. A.; Phillips, A. K.; Moore, R. B., SAXS Analysis of the Thermal Relaxation of Anisotropic Morphologies in Oriented Nafion Membranes. *Macromolecules* **2006,** *39* (11), 3939-3946.

11. Kamal, J. S.; Gomes, R.; Hens, Z.; Karvar, M.; Neyts, K.; Compernolle, S.; Vanhaecke, F., Direct Determination of Absorption Anisotropy in Colloidal Quantum Rods. *Phys. Rev. B* **2012,** *85* (3), 035126.

12. Murray, C. B.; Norris, D. J.; Bawendi, M. G., Synthesis and Characterization of Nearly Monodisperse CdE (E = Sulfur, Selenium, Tellurium) Semiconductor Nanocrystallites. *J. Am. Chem. Soc.* **1993,** *115* (19), 8706-8715.

13. Wang, T.; Zhuang, J.; Lynch, J.; Chen, O.; Wang, Z.; Wang, X.; LaMontagne, D.; Wu, H.; Wang, Z.; Cao, Y. C., Self-Assembled Colloidal Superparticles from Nanorods. *Science* **2012,** *338* (6105), 358-363.

14. Abécassis, B.; Tessier, M. D.; Davidson, P.; Dubertret, B., Self-Assembly of CdSe Nanoplatelets into Giant Micrometer-Scale Needles Emitting Polarized Light. *Nano Lett.* **2014,** *14* (2), 710-715.

15. Riedinger, A.; Ott, F. D.; Mule, A.; Mazzotti, S.; Knusel, P. N.; Kress, S. J. P.; Prins, F.; Erwin, S. C.; Norris, D. J., An intrinsic growth instability in isotropic materials leads to quasi-two-dimensional nanoplatelets. *Nat Mater* **2017,** *16* (7), 743-748.

16. Gao, Y.; Weidman, M. C.; Tisdale, W. A., CdSe Nanoplatelet Films with Controlled Orientation of their Transition Dipole Moment. *Nano letters* **2017,** *17* (6), 3837-3843.

17. Scott, R.; Heckmann, J.; Prudnikau, A. V.; Antanovich, A.; Mikhailov, A.; Owschimikow, N.; Artemyev, M.; Climente, J. I.; Woggon, U.; Grosse, N. B.; Achtstein, A. W., Directed emission of CdSe nanoplatelets originating from strongly anisotropic 2D electronic structure. *Nature Nanotechnology* **2017,** *12*, 1155.

18. Bronstein, N. D.; Li, L.; Xu, L.; Yao, Y.; Ferry, V. E.; Alivisatos, A. P.; Nuzzo, R. G., Luminescent Solar Concentration with Semiconductor Nanorods and Transfer-Printed Micro-Silicon Solar Cells. *ACS Nano* **2014,** *8* (1), 44-53.

19. Coropceanu, I.; Bawendi, M. G., Core/Shell Quantum Dot Based Luminescent Solar Concentrators with Reduced Reabsorption and Enhanced Efficiency. *Nano Lett.* **2014,** *14* (7), 4097-4101.

20. Meinardi, F.; Colombo, A.; Velizhanin, K. A.; Simonutti, R.; Lorenzon, M.; Beverina, L.; Viswanatha, R.; Klimov, V. I.; Brovelli, S., Large-Area Luminescent Solar Concentrators based on `Stokes-Shift-Engineered' Nanocrystals in a Mass-Polymerized PMMA Matrix. *Nat. Photonics* **2014,** *8* (5), 392-399.

21. Grivas, C.; Li, C.; Andreakou, P.; Wang, P.; Ding, M.; Brambilla, G.; Manna, L.; Lagoudakis, P., Single-Mode Tunable Laser Emission in the Single-Exciton Regime from Colloidal Nanocrystals. *Nat Commun.* **2013,** *4*.

22. She, C.; Fedin, I.; Dolzhnikov, D. S.; Demortière, A.; Schaller, R. D.; Pelton, M.; Talapin, D. V., Low-Threshold Stimulated Emission Using Colloidal Quantum Wells. *Nano Lett.* **2014,** *14* (5), 2772-2777.

23. She, C.; Fedin, I.; Dolzhnikov, D. S.; Dahlberg, P. D.; Engel, G. S.; Schaller, R. D.; Talapin, D. V., Red, Yellow, Green, and Blue Amplified Spontaneous Emission and Lasing Using Colloidal CdSe Nanoplatelets. *ACS Nano* **2015,** *9* (10), 9475-9485.

24. Hikmet, R. A. M.; Chin, P. T. K.; Talapin, D. V.; Weller, H., Polarized-Light-Emitting Quantum-Rod Diodes. *Advanced materials* **2005,** *17* (11), 1436-1439.

25. Rizzo, A.; Nobile, C.; Mazzeo, M.; Giorgi, M. D.; Fiore, A.; Carbone, L.; Cingolani, R.; Manna, L.; Gigli, G., Polarized Light Emitting Diode by Long-Range Nanorod Self-Assembling on a Water Surface. *ACS Nano* **2009,** *3* (6), 1506-1512.

26. Cunningham, P. D.; Souza, J. B.; Fedin, I.; She, C.; Lee, B.; Talapin, D. V., Assessment of Anisotropic Semiconductor Nanorod and Nanoplatelet Heterostructures with Polarized Emission for Liquid Crystal Display Technology. *ACS Nano* **2016,** *10* (6), 5769-5781.

3. **Surface-reaction-limited pathway toward ZnSe nanostructures**

3.1. **Introduction: New species of quasi-2D nanoplatelets**

For decades, colloidal semiconductor nanocrystals (NCs) have been attractive for optoelectronic applications due to their narrow emission and large absorption coefficient. It has been established that synthetic methods for Cd-based materials have tremendous control over size, shape, optical quality, and stability. Such structures have been brought to manufacturing scale and included as backlighting layers in QD-based displays. The work in the second project was primarily motivated by a goal to synthesize Cd-free anisotropic emitters in the appropriate spectral range. Future technologies may therefore use III-V semiconductors (e.g. InP) or zinc-containing II-VI semiconductors as emissive materials.

Colloidal nanocrystals (NCs) can now be synthesized with impressive control over shape.[1] A wide variety of anisotropic growth methods can be accessed due to the energetically favorable faceted growth or highly specific surface-ligand binding. Advances in synthetic control of shape have led to a variety of colloidal materials with atomically precise width, often called quasi-2D nanostructures.[2] The classic example of these structures is that of CdSe nanoplatelets (NPLs). These structures exhibit the electronic structures of quantum wells[3] with extremely narrow photoluminescence linewidth, lasing,[4] and in-plane transition dipoles that lead to intrinsically directional emission.[5-6] CdSe NPLs and their resulting core-shells have quantum yields above 80%.[7] Atomically precise platelet emitters are not only attractive for their high color purity and quantum yield—the strongly directed emission should be able to address efficiency limitations in a light-emitting diode (LED) structure.

Several distinct mechanisms have been proposed for the broad class of 2D nanomaterials. Quasi-2D CdSe materials, referred to as nanoplatelets,[3, 8-9] nanoribbons,[10-11] nanosheets,[12] and

quantum belts[13-14] are observed to form under varying reaction conditions. These structures are formed under two distinct synthetic categories, one using long-chain amine solvents at lower temperatures, yielding wurtzite structures, and one done in the presence of carboxylic acids at higher temperatures, yielding zinc-blende structures.[15]

The mechanism of 2D wurtzite CdSe growth was first hypothesized as annealing in soft colloidal templates.[12] The exact role of the template is unclear, as the presence of lamellar stacks observed *ex situ* is generally claimed to be evidence of template-controlled reaction. The amine-bilayer template, formed via dissolution of metal salt precursor in long-chain amines, is known to have lamellar structure and is hypothesized to be a planar reaction gallery in which 2D nanocrystals nucleate and grow.[12, 16] Additionally, it is suggested that this template plays a role in either stabilizing assemblies or directing nucleation of "magic-sized clusters" (MSCs).[8, 13, 17] Recent work suggests MSCs can be formed upon introduction of chalcogenide precursor in an isotropic/amorphous metal-surfactant/solvent system with lamellar mesophases subsequently acting as a stabilizing environment.[18-19]

Alternatively, 2D structure growth can be achieved in isotropic lattices when surface instabilities of different facets exist, yielding growth of different populations of quasi-2D nanoplatelets with zinc blende structure.[20] This nanoplatelet growth occurs absent a molecular template. Furthermore, the distribution of populations does not defocus but jumps sequentially between discrete monolayer thicknesses as a function of ripening.[20-21] In both wurtzite and zinc-blende synthetic recipes, it is experimentally observed is that small 0D subunits can transition shape and confinement environments to 2D structures during synthesis, indicating that the assembly or unstable growth on starting nuclei are a unifying idea for the general synthesis of anisotropic 2D structures.[22-23] This principle has been further demonstrated wherein small

purified Zn-blende CdSe spheres were reintroduced into growth mixture and formed CdSe nanoplatelets through intraparticle ripening and lateral extension as monomers were incorporated.[24] An understanding of these pathways is critical to precise control of suitable materials for optoelectronic applications

In contrast with their Cd-based counterparts, Zn-chalcogenides represent a relatively unexplored class of materials, despite being an attractive target for heavy-metal-free "green" syntheses. ZnSe is an ideal semiconductor for alternative structures that emit in the UV-blue region, with a bulk band gap of 2.7 eV. The first synthetic routes for emissive ZnSe were reported decades ago and used reactive diethyl zinc and trioctylphosphine selenium in long chain amines at high temperatures.[25] Shell-growth of ZnS can be performed to improve the photoluminescence quantum yield of these structures.[26-28]

Despite early discovery of colloidal routes to ZnSe nanocrystals and intrinsic polytypism,[29] shape control of ZnSe has been somewhat limited compared to Cd-based materials. Early examples of shape control in ZnSe structures utilized injection or addition of precursors in hot alkylamine mixtures to yield nanorods/nanowires in ordered arrays[30] or isolable oblate species with some rod-like character.[31] In the case of CdSe, emissive nanorod heterostructures can be precisely controlled by highly selective seeded-growth along the wurtzite *c*-axis.[32] These tunable structures are attractive, with near unity quantum yield[33] and ability to be incorporated in LEDs that exploit their shape. This type of control and optimization of anisotropic ZnSe nanorods remains elusive. Currently, it is proposed that ZnSe nanorods instead be formed through lower-temperature routes in which nanowires formed in alkylamine bilayer template are truncated and aged.[34] This ripening requirement leads to thermodynamic control of their width,

with recent improvements in length control realized by tuning synthesis with addition of molecular Zn_4 clusters.[35]

Less explored are synthetic routes to quasi-2D ZnSe nanostructures and their corresponding mechanisms. ZnSe nanosheets with wurtzite crystal structure have been synthesized in primary alkylamine mixture, with oriented attachment being described as driving force.[36] The same lamellar templated growth of CdSe platelets from MSC starting material has been demonstrated experimentally for ZnSe platelets.[17] The proposed MSCs often share the same optically precise doublet as platelets, highlighting the potential the importance of their role but obfuscating clear delineation of transition from 0D to 2D structures. For example, three populations of ZnSe MSCs with optical doublets and first exciton at 291, 318, and 345 nm were observed in one-pot syntheses but characterization of 0D, 1D, or 2D morphology from TEM images is ambiguous.[37]

The formation of ZnSe nanoplatelets would eventually make an attractive target for Cd-free emitters. With this target in mind, we developed an understanding of quantized growth mechanism of ZnSe that is responsible for the eventual formation of two species of quasi-2D nanostructures. Depending on the growth temperature, ZnSe nanocrystal reactions can either be brought under the diffusion-limit, where growth and/or ripening is approximately spherical/isotropic or the surface-reaction-limit, where growth is facet-specific. Unlike low-temperature growth methods for wurtzite CdSe 2D structures, our higher temperature synthesis occurs absent a template and is likely dependent on this facet-specific addition of monomer and subsequent ripening to thicker populations. The discovery of surface reaction-limited pathways had led an improved synthetic route towards atomically thin ZnSe nanoplatelets—with evidence of ripening towards a previously unreported population. These nanoplatelet species have narrow

UV photoluminescence and can be isolated in high purities. The synthetic and mechanistic information may inform the possible future synthetic routes to high-quality core or shell materials for emissive structures.

3.2. **Overview of ZnSe nanostructure synthesis**

3.2.1. Different dimensionalities obtained with the same precursors

In most standard colloidal syntheses, nanocrystals tend to grow isotropically, forming nearly spherical nanoparticles. As a consequence, the synthetic conditions that favor anisotropic shapes are often quite different from those of spheres. Starting with a solvent-surfactant consisting of primary amine(s), we can combine zinc salts (R = oleate, stearate, acetate, nitrate, and chloride) and elemental Se to generally yield ZnSe nanostructures (Figure 3.1a). Interestingly, we found that the final material isolated from the reaction mixture varies widely and is primarily dependent on addition and growth temperature. Using identical zinc and selenium precursors in primary amine solvents, ZnSe nanostructures with 1, and 2, 3-dimensional confinement can be accessed by biasing the reaction pathway with different addition temperatures. Analysis of isolated products from reactions shows that we can achieve different species with identical reagents by simply changing the temperature parameters. Combining $Zn(oleate)_2$ and elemental selenium in hot oleylamine at 250 °C yields quasi-spherical particles, with polymorphism coming from annealing events over extended growth times (Figure 3.1b). Nanowire growth can be realized through addition of precursors below 160 °C and their growth is driven by heating up to 250 °C (Figure 3.1c). When the identical set of precursors are combined at room temperature in primary amines and heated to 160 °C, quasi-2D ZnSe nanoplatelets are isolated (Figure 3.1d). By limiting the reaction temperature and growth times,

the final isolated product remains dependent on the atomically-precise starting material. These metastable phases serve as the relevant nuclei wherein the differences in the surface reactivity lead to 1 and 2-dimensional suppression of growth, subsequently driving the anisotropic growth of nanoplatelets and nanowires, respectively. When precursors are combined at high temperatures or allowed to rapidly heat, polymorphic and spherical nanoparticles are formed.

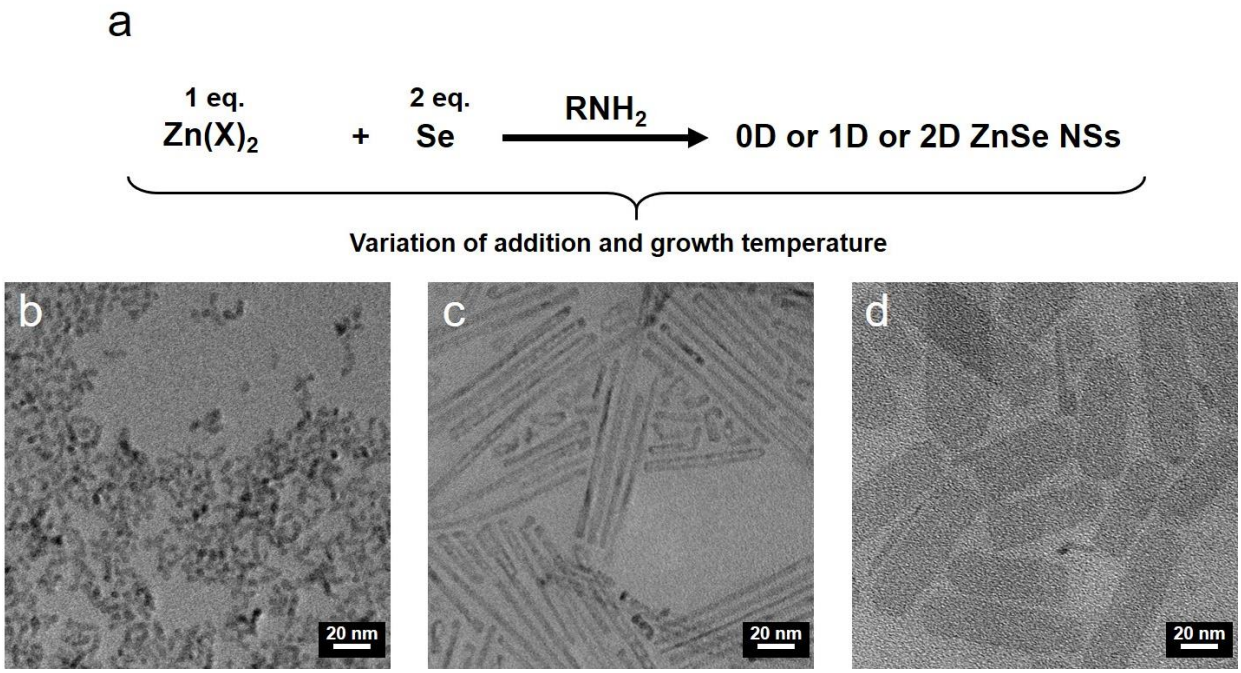

Figure 3.1. ZnSe nanocrystals of different dimensionality form starting from same precursors: (a) Generalized reaction scheme of ZnSe nanostructure formation. Variation of addition and growth temperature of one or both monomers determine dimensionality. The resulting TEM images show the products of these different pathways in the form of (b) isotropic dots, (c) nanowires and nanowire couples, (e) nanoplatelets.

3.2.2. Discussion of bifurcated reaction pathway

In classical nanoparticle nucleation and growth, reactions must overcome an activation barrier, where critical nucleus size is reached and growth occurs continuously. In a quantized growth regime, particles are seemingly “trapped” in shallow metastable potential energy wells. In our system, we observe that under similar reagent concentration, varying temperature leads to these

bifurcating reaction pathways. Traditional hot-injection growth is known to fall under diffusion-control, where at high temperatures the initial formation of monomer and subsequent nucleation is mainly limited by the mixing time of the reagents. This regime leads to classical nanoparticle growth where the critical nucleation barrier is overcome and rapid consumption of monomer drives continuous isotropic nanoparticle growth (Figure 3.2). Alternatively, quantized growth can be observed for discrete atomically-precise clusters, where nuclei formation is instead limited by the metastable "mesophase" formation[18] and for discrete nanoplatelets, where quantized growth is observed and populations sequentially jump from monolayer to monolayer.[21] Under this regime, the barrier to isotropic nucleation is likely sufficiently high due to low availability of reactive monomer or hindered reactivity of nuclei and the reaction proceeds through quantized local thermodynamic minima (Figure 3.2). These metastable phases serve as the relevant nuclei wherein the differences in the surface reactivity likely lead to 1 and 2-dimensional suppression of growth, subsequently driving the anisotropic growth of nanoplatelets and nanowires, respectively. Our reactions illustrate that different dimensionalities of nanostructures can be realized using identical reagents and simply changing the temperature parameters.

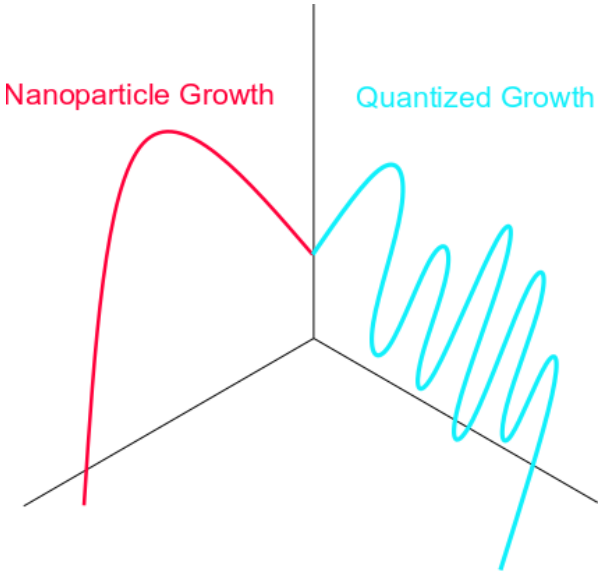

Figure 3.2. Qualitative comparison of classical nucleation leading to nanoparticle growth and non-classical nucleation leading to quantized growth.

3.3. **Nanostructures on quantized-growth pathway**

3.3.1. Absorption of species observed

The most exciting consequence of this work is that we have introduced a new set of ZnSe nanocrystals. The basic premise for the synthesis starting point was first discovered in a recipe using heat up synthesis of Zn and Se components in an oleylamine/octylamine mixture.[36] When under these synthetic conditions, the reaction proceeds with quantized growth and four kinetically trapped populations are observed (Figure 3.3a). Additionally, the populations are observed sequentially—at low temperatures we see the highest energy species with our lowest energy species forming at terminal stages of the reaction. In general, we sought to isolate and observe these populations to determine their morphology.

3.3.2. Observed morphology of atomically precise species

During the heat-up synthesis, several narrow-linewidth aliquots with optical doublets at different energies were observed. The first of these species can be observed with first absorption

at 291 nm, and isolated as 100-500 nm sized "bundles." It is believed to be indicative of magic-sized-cluster (MSC) species that are coordinated in some fashion (Figure 3.3b). The presence of these clusters has been suggested in the literature and the same set of optically-precise doublet species are often observed. Occasionally, a population of atomically-precise species is observed with first absorption around ~318 nm. When isolated, this species appears as long bundles of thin wires and is rarely observed without additional populations present (Figure 3.3c). Further along the reaction coordinate, the first set of clear quasi-2D ZnSe nanostructures appears with first absorption feature at 345 nm. This population has been demonstrated in prior literature and this is generally the most stable population, appearing as discrete platelets with rectangular aspect ratios (Figure 3.3d). Finally, we have demonstrated for the first time the isolation of another quasi-2D ZnSe nanostructure population with first absorption at ~380 nm. These species are often isolated as long nanosheets (Figure 3.3e).

3.3.3. Estimation of energy levels using quantum well electronic structure

The experimental values for first and second exciton in these species were compared with an effective band model of band energies for quantum well structures (Figure 3.3f, see paragraphs below for assumptions). Not surprisingly, the electronic structure of our two distinct platelet species better fits the model than the earlier populations observed—this fact further supports that these populations are some form of coordinated "magic-sized" clusters.

In order to estimate the excitonic energy levels in ZnSe nanoplatelets we have taken the approach described by Efros et al.[3] Briefly, the position of the bulk bands is calculated within the formalism of the eight-band Pidgeon Brown model. The bulk parameters used in the calculation are summarized in Table 3.1. Constants used in approximation of ZnSe quantum well electronic

structure. The energy of the quantum sized level was then found by scaling the band energy by the canonical energy relationship in quantum wells:

$$E_k = \frac{\hbar^2 \pi^2}{2mL_z^2}$$

Where m is the free electron mass and L_z is the thickness of the well. By solving the coupled equations of the Pidgeon Brown Hamiltonian, one obtains the positions of the conduction band (E_{hh}), the heavy hole band (E_{lh}), the light hole band (E_s), and the split off band. The energy of the optical transitions are taken as the energy difference between the energy of the conduction band and the respective hole band minus the exciton binding energy. Here we assumed exciton binding energies of 100 meV. So for example the energy of the transition associated with the heavy hole band could be expressed as:

$$E_{c-hh} = E_c - E_{hh} - E_{binding,hh}$$

Table 3.1. Constants used in approximation of ZnSe quantum well electronic structure

Constant	**Value**
a	0.35
E_g (eV)	2.7
E_p (eV)	24.2
Δ (eV)	0.43
α	0*
γ_1	4.3
γ_2	1.8
$E_{binding,hh}$ (eV)	0.1
$E_{binding,lh}$ (eV)	0.1

*Since no literature value was found this term was taken to be zero, which is a reasonable approximation given the wide bandgap of ZnSe.

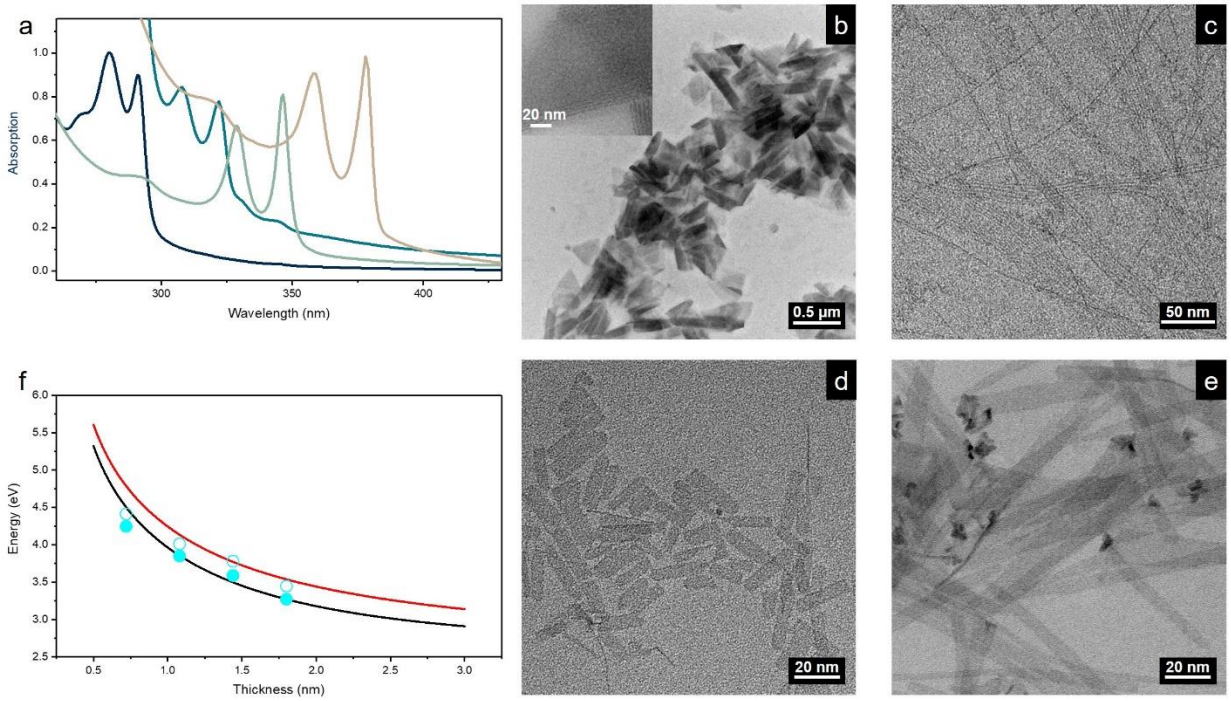

Figure 3.3. Accessible populations of atomically-precise nanostructures synthesized in heat-up protocol: (a) Absorption spectra of all populations isolated and observed at varying stages of 2D nanostructure synthesis. (b-e) TEM images of the relevant isolable species. (b) Sub-micron size triangular mesophases of species with first abs. ~291 nm, inset shows a zoom-in of lamellar-type structuring. (c) Species isolated at with first abs. ~318 nm shows long bundles of thin nanowires. (d) Nanoplatelets with first exciton of ~345 nm isolated with discrete platelet morphology. (e) Species at with first exciton at ~380 nm isolated with nanoribbon like morphology. (f) Band energy of heavy hole (black trace) and light hole (red trace) calculated from our approach below. Calculated values are plotted against experimental values for peaks observed from absorption features. The thickness values for the two highest energy species are calculated under the assumption that they are 2 and 3 monolayer species.

3.4. **Properties and isolation two pure populations of quasi-2D nanostructures**

3.4.1. Synthesis of "345 nm" or four monolayer ZnSe nanoplatelets

ZnSe nanoplatelets were grown in a similar manner to a literature recipe with several modifications.[36] To a 100 mL three-neck round bottom flask, 187 mg (0.3 mmol) of zinc stearate was added along with 10 mL of oleylamine. The flask was heated under vacuum at 100 °C for 90 mins before cooling back to room temperature under nitrogen. To the cooled flask, 5 mL of octylamine and 48 mg of selenium powder (0.6 mmol) was added under positive N_2 pressure and

resealed. After evacuating and refilling with N_2 several times, the flask was heated to 100 °C and allowed to rest for 30 mins. The flask was then heated to 170 °C, taking special care to make sure the temperature does not exceed 170 °C. The platelets proceeded with growth at 170 °C for anywhere from 5 mins to 6 hours. The generality of this approach was extended to several different ranges of temperatures, reagents, and concentrations. After completion, the mixture was cooled naturally and 2 mL of *n*-trioctylphosphine (TOP) was added to the flask at ~70 °C to quench any unreacted Se species. The resulting turbid white suspension was then transferred to a glovebox and precipitated via centrifugation. The precipitate was then redispersed in ~15 mL of methylcyclohexane at which time any insoluble side products or nanoparticles were precipitated by centrifugation without non-solvent. The supernatants contained concentrated NPL solutions and can be further purified using a small amount of ethanol before or after storage.

3.4.2. Synthesis of "380 nm" or five monolayer ZnSe nanoplatelets

Larger platelets with first absorption at 380 nm can be synthesized using a simple modification to the above procedure for 4 ML platelets. After heating the flask to 170 °C, the reaction is allowed to proceed for 20 mins. At this time, an excess of Se shot (100-200 mg) is added to the reaction flask to make available more soluble precursor. This addition induces a transition to a lower energy atomically-precise nanoplatelet—in order to ensure quantitative transition, the absorption was monitored with needle-tip aliquots injected into 5% TOP in methylcyclohexane every 10 mins until the peak at 345 disappeared. This transition typically takes 30-120 mins and it was also found that we could achieve partial transitions with more rapid increase of temperature and deliberate overshoot to 180 °C. However, care should be taken to avoid the formation of larger polymorphic-species that often form as a result of this transition.

Full transitions could also be achieved with higher concentrations of starting reagent and longer reaction times, which will be discussed in future ripening experiments.

3.4.3. Optical properties of ZnSe quasi-2D nanostructures

A consequence of this quantized-growth pathway is that we have demonstrated two populations of colloidally-stable nanoplatelets with narrow absorption and emission linewidth which are well dispersed in solution and have 2D morphology (Figure 3.4a-c). The first absorption for these species was found at 345 nm with negligible Stokes shift in the emission (Figure 3.4a). The FWHM of the emission in these species was found to be 4.0 nm (41 meV). The first absorption for the next observed species was found at 380 nm with similar properties of a 2D-quantum well emitter (Figure 3.4a). The FWHM of the emission in these species was found to be 4.4 nm (39 meV). Although emission was observed in the case of the species observed blue of the NPLs (~320 nm), the FWHM of these species was 5.0 nm (60 meV) and such broadening of the linewidth is likely due to lack of true 2D structure. This lack of quantum confinement in one dimension only is observed as morphological structure of extremely thin wires (Figure 3.3c).

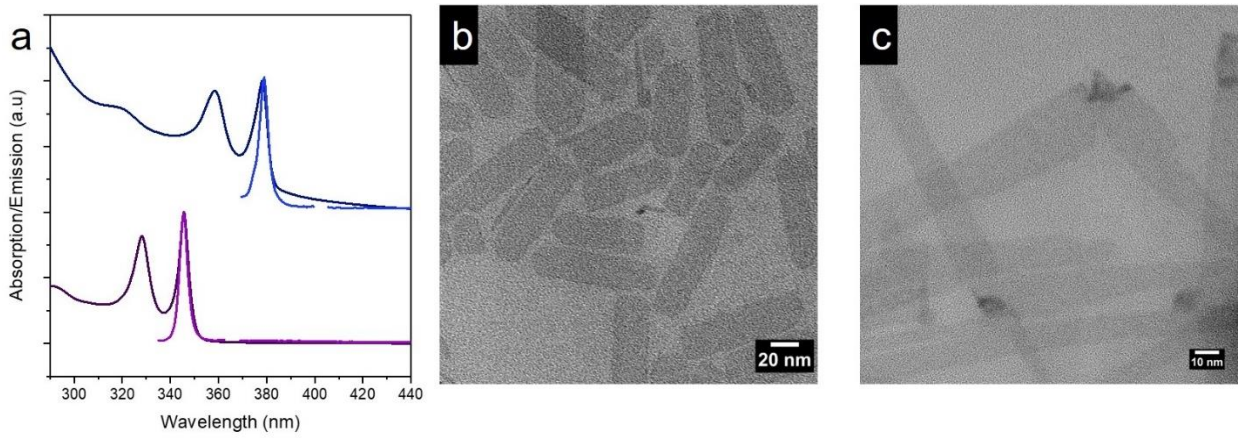

Figure 3.4. Two populations of discrete quasi-2D ZnSe nanostructures: (a) Absorption and emission spectra of showing extremely narrow linewidth in the UV. TEM images showing morphology of species with (b) absorption at 345 nm and species with (c) absorption at 380 nm.

3.4.4. Determination of number of monolayer thickness of 2D structures

When high precursor concentration is maintained, the platelets undergo a well-defined kinetic transition to a population which is hypothesized to be one additional monolayer in thickness (Figure 3.3e). The thickness of platelet was measured through TEM analysis of platelets that were stacked on their side. The thickness of "345" NPLs was measured to be 1.47 ± 0.17 nm (Figure 3.5). This is consistent with previously reported value of 1.4 nm.[36] The thickness of "380" NPLs was experimentally determined to be 1.84 ± 0.20 nm (Figure 3.5). Using the reasonable assumption that the NPLs are comprised of an integer multiple of monolayers (MLs), we hypothesized that this population "jumped" sequentially with m to m + 1 monolayers:

$$m_{345} + 1 = m_{380}$$

As the number of monolayers should have equal heights then can then derive the following relationship:

$$\frac{m_{345}}{m_{345} + 1} = \frac{l_{345}}{l_{380}} = 0.8$$

Based on this relationship and the ratio of the experimental values, we can estimate that the "345" and "380" populations are 4 and 5 ML, respectively.

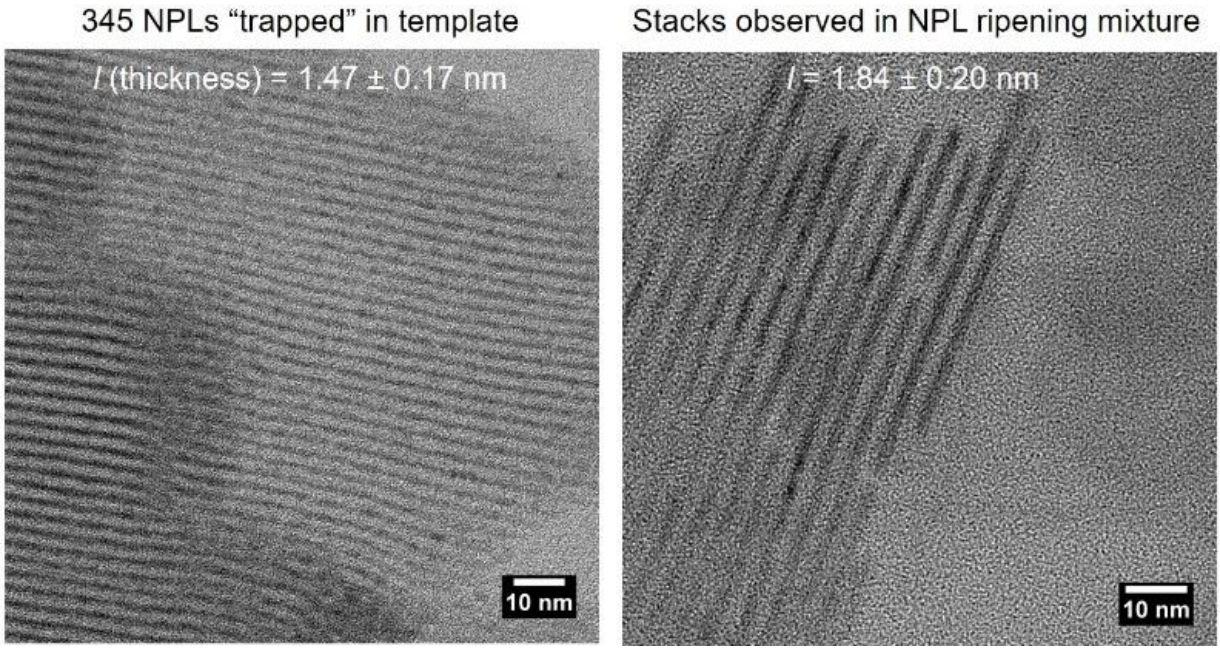

Figure 3.5. TEM analysis of controlled stacks of each platelet population.

3.4.5. Difference in crystalline phase between 4- and 5-ML species

The crystalline phase of large-scale syntheses of ZnSe nanoplatelet samples was characterized using powder X-ray diffraction (Figure 3.6). In the case of 4 ML platelets, the wurtzite reflections were very clear with enhanced (002) peak and suppressed (110) and (112) (Figure 3.6, black). Surprisingly, in pure 380 NPLs, we consistently see peaks that are characteristic of cubic Zn-blende structure (Figure 3.6, red). No strong reflections from (102) and (103) are observed, but there is a (100) peak from wurtzite structure. The observation of a phase change is supportive of separate nucleation and subsequent growth modes of 5 ML structures. This apparent phase change supports our below mechanism 5 monolayer platelets grow from different zinc-blende nuclei and do not simply grow through addition of monolayer on an existing large 345 NPL.

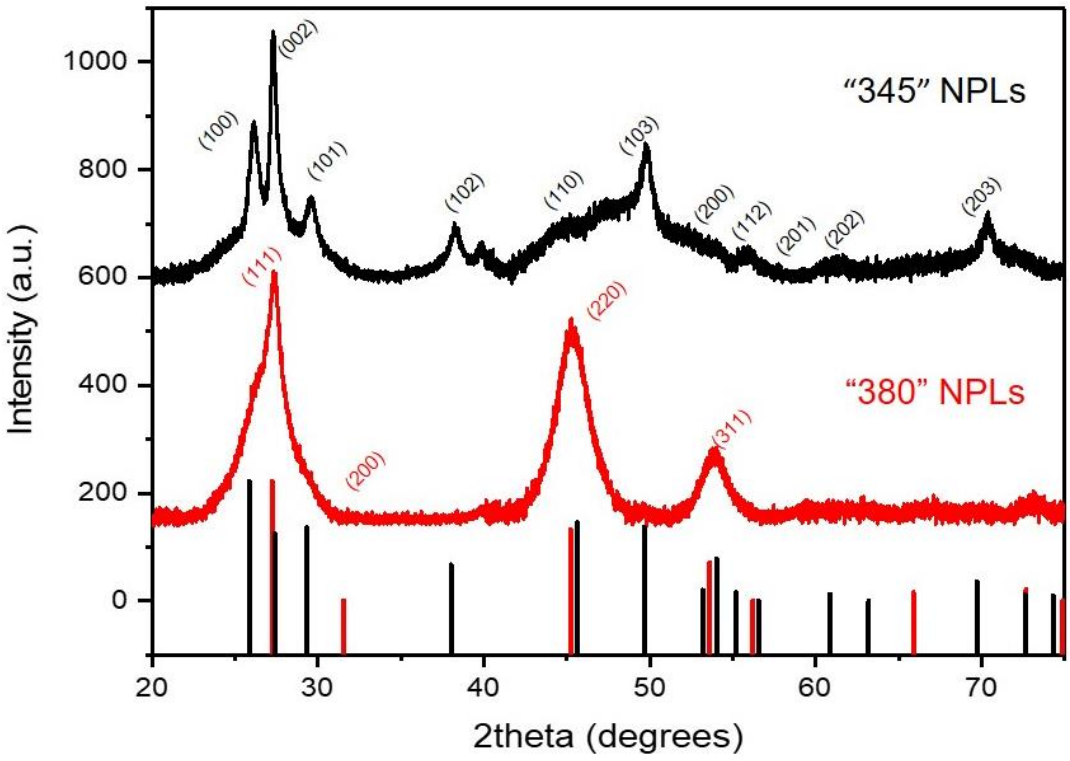

Figure 3.6. Powder X-ray diffraction patterns of 4 ML "345 nm" ZnSe NPLs (black) and 5 ML "380 nm" ZnSe NPLs (red) compared with the bulk reflections for wurtzite and Zn-blende, respectively.

3.4.6. Observations from ZnSe nanowire synthesis

Our initial strategy was based on the wire growth for pure ZnSe structures. The protocol employed involves a multi-step heat-up synthesis where we combine precursors at 160 °C and generate ZnSe nuclei/wire precursors (Figure 3.7a). The resulting set of structures has a preferred wire-like orientation, likely due to the specific binding of the cluster-like intermediates. Here we notice that first absorption of these pre-wire species is narrow and nearly identical to that of "3 ML" wire species. This set of nuclei may play an important role in direction the surface reactivity of these wire nuclei. Through heating and growth and aging processes, we can generate a variety of rod and wire-like structures and in a typical synthesis, we see redshift of the

absorption spectra to species with a broad peak at ~400 nm (Figure 3.7a-b). Some minor changes in temperature, concentration, and zinc precursor have yielded dramatic changes in the final 1D species morphology (Figure 3.7c). Because of the reaction-controlled process in which wires form, the "growth" of rod-like structures is heavily dependent on the initial shape, followed by a material diffusion/aging process. Unlike CdS, the most successful example of rod-like shells, which relies on epitaxial growth kinetically overdriven along the c-axis of wurtzite CdSe, ZnSe nanorod growth is instead achieved by having cluster-like monomers which crystallize into wires and then ripen to form thicker species.

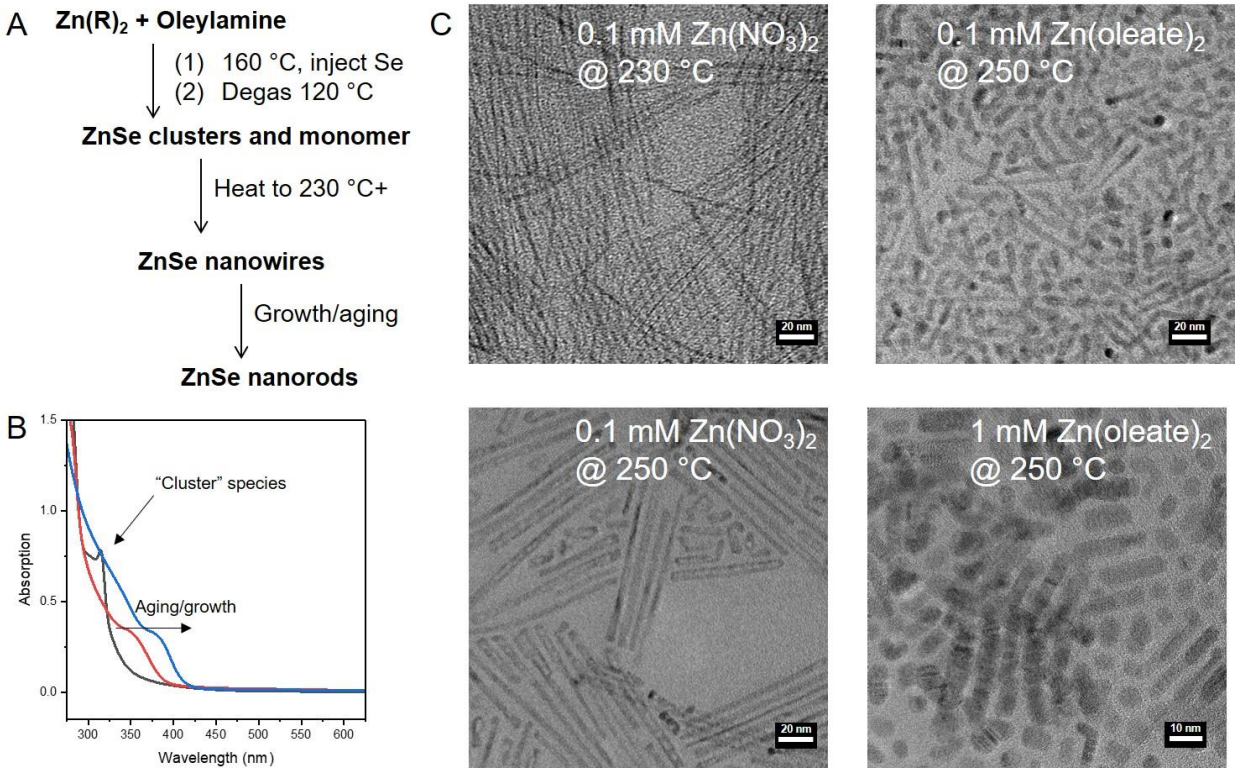

Figure 3.7. General strategy towards synthesis of ZnSe nanowires and nanorods: (a) idealized scheme representing different stages of the ZnSe reaction. (b) Absorption spectra of ideal synthesis showing evolution of narrow "magic-sized" species followed by redshift indicative of thickening of the nanowires into rods. (c) TEM images of various isolated species from synthetic protocols with different zinc precursors and concentrations.

3.5. **Mechanism of 4 ML platelet formation**

3.5.1. Suggested mechanisms for platelet formation

Previous work has suggested the role of a "soft-colloidal template" in which shape and crystallization of wurtzite metal-chalcogenide platelets is directed.[12-13, 16] This growth model suggest that anisotropically structured metal-amine precursor serves as a template for the growth of flat nanocrystals. In the case of ZnSe, the literature indicates that these structures could be formed from a template of MSCs.[17] These low temperature preparations likely have a stabilizing effect due to stacking of the large structures, making it difficult to elucidate the exact nature of template *in situ.* The early species generated in our synthetic protocols resemble MSCs with nearly identical first absorption peaks to those in the literature.[37] We observe that our possible MSCs that are indeed coordinated in lamellar mesophases in the early stages of synthesis (Figure 3.3b-c). The growth and stability of various NPL populations in zinc-blende CdSe has been alternative treatment by the Norris group.[20-21] Their model and experimental data reveal that the growth of these platelets are not dependent on a template, but rather governed by differences in facet-specific growth kinetics at the nanoscale.

3.5.2. Ripening experiments

Instead of addition of Se shot, we used a larger concentration of precursor (200 mM Zn, 400 mM Se) in order to analyze the temporal evolution of platelet species. Zinc oleate was used in order to ensure complete dissolution of zinc precursor to leave the saturation of selenium as the only uncontrolled variable. In the high concentration synthesis, we expect to maintain a reservoir of precursor and monomer and could examine the evolution of each species as reactions were held at constant temperature (100, 125, 150 ºC) in order to reveal the kinetic aspects of the

reaction mixture. The absorption was monitored with needle-tip aliquots injected into 5% TOP in methylcyclohexane and representative samples were analysis in TEM.

3.5.3. Formation of 4 ML at low temperatures

Here we sought to reconcile the growth of our ZnSe nanoplatelets with either one or both of these models by assessing the path-dependence of our model. The time-evolution of the absorption spectra was used to analyze and isolate the intermediate species and identify critical temperature points. In our first stages of the reaction, quantitative formation of the "291 nm" species is observed when the reaction is held at 100 or 125 °C (Figure 3.8a-b). These intermediate aliquots are solution-soluble large-scale mesophases that stabilize some form of atomically precise species (Figure 3.8b). Extended reaction times finalize the transition of "291 nm" species into 4 ML nanoplatelets with first exciton at 345 nm (Figure 3.8a-b). In aliquots containing both sets of species, we observed the presence of both 100-500 nm sized mesophases and free-standing platelets (Figure 3.8c). This observation likely indicates that species stabilized within these mesophases may be responsible for forming the relevant nuclei for 4 monolayer platelets. The difference in size and shape of platelets versus their intermediate mesophases called into question the presence of an annealing process of platelets within a planar reaction gallery. Thus, the state of the metal-amine precursor at high temperatures was determined using small-angle X-ray scattering experiments (SAXS). Concentrated templates of the relevant amines (oleylamine and octylamine) within the reaction mixture were prepared and added to capillaries where they were subject to slow-heating. Both zinc-amine complexes had lamellar structure with a set of (00*l*) peaks that scaled with the size of the amine chain (Figure 3.8d). Interestingly, the sharp lamellar peaks disappear into broad peaks at temperatures less than or equal to 60 °C, indicating that templates completely disappear and form a glassy/disordered state

in the Zn-amine complex (Figure 3.8d-e). A more detailed analysis is available in the next section.

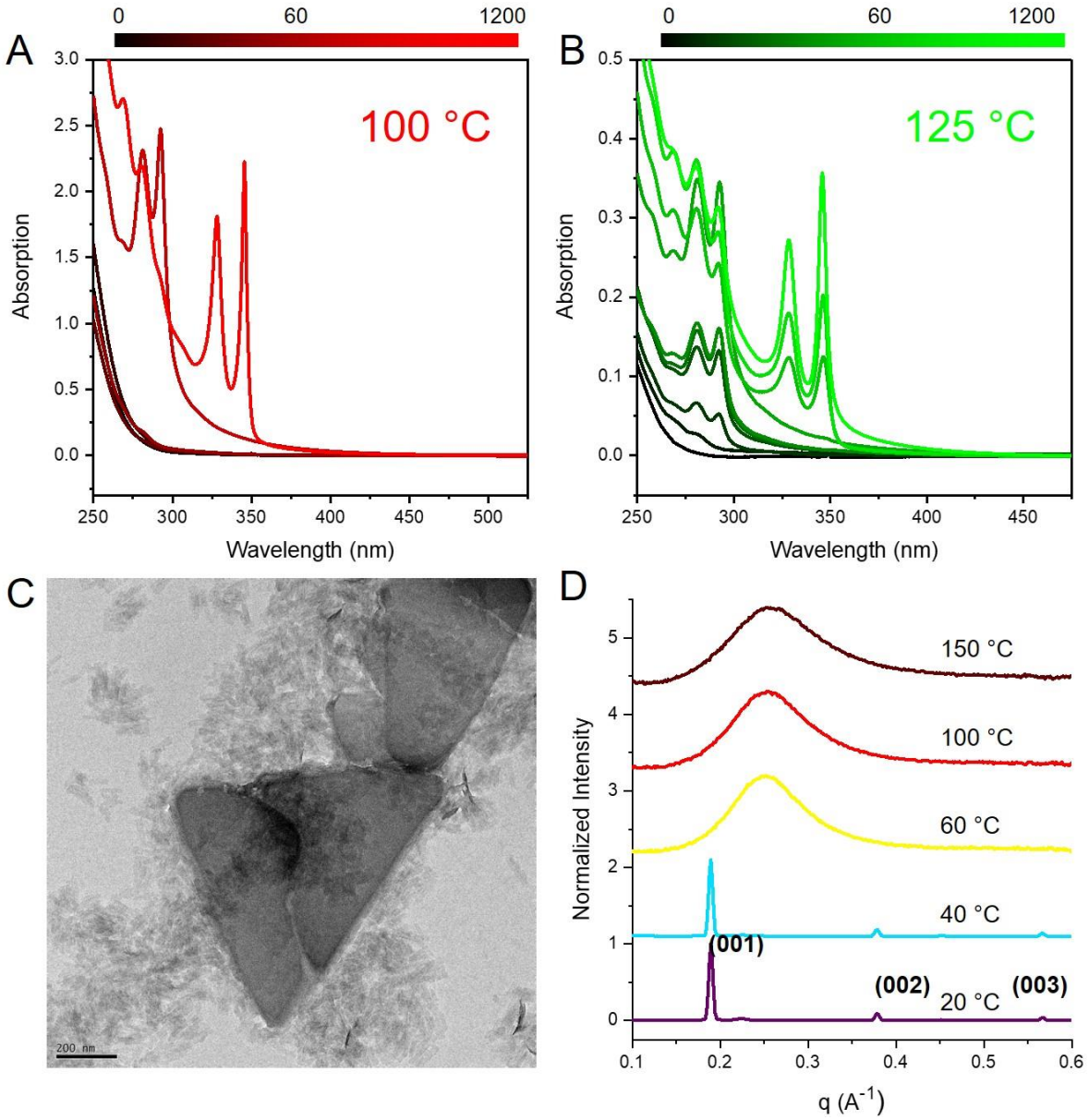

Figure 3.8. Nanoplatelet species are formed without the dependence on a metal-amine bilayer reaction template: (a-b) Temporal evolution of atomically precise species in absorption spectra after heating reaction mixture to (a) 100 °C and (b) 125 °C. Here time (mins) is color coded and shown in an approximately log scale. (c) TEM image of mixed system of "291 nm" and "345 nm" first absorption shows dual-presence of a mesophase and discrete platelets. (d) X-ray scattering experiments revealing that lamellar-structured Zn-amine complexes become isotropic at relevant reaction temperatures (100 °C).

3.6. **Additional SAXS analysis of template**

The role of an amine-bilayer template has often been suggested in the synthesis of various 2D nanostructures. In one such example, PbS was described to crystallize within the "reaction gallery" of a metal-amine bilayer template. Alternatively, room temperature methods for CdSe MSCs suggests that these clusters form within lamellar mesophase templates and are subsequently annealed and exfoliated to form free-standing 2D structures. The presence of a metal-amine bilayer is easily conceivable in low-temperature or amphiphilic—these mesophases likely induce high local concentrations of their metal compound. The lack of amine-bilayer lamellar structure reveals that the template is likely not responsible for directing shape of our platelet species. Instead, we propose that the cluster species formed in the early stages of the reaction are stabilized by a self-assembled mesophases. The equilibrium concentration of free clusters then increases with reaction temperature and free-clusters and behave as both nuclei and monomer for the anisotropic nanoplatelet growth.

In order to probe the role of this template in our high temperature Zn-based system, we studied the dissolved Zn complexes using *in situ* SAXS experiments. The experimental preparations are detailed below.

3.6.1. Preparation of $Zn(OAc)_2(RNH_2)$ species:

In inert atmosphere, 92 mg (0.5 mmol) of zinc acetate (anhydrous) was added to a 4 mL vial along with either 267 mg (1 mmol) of oleylamine, 129 mg (1 mmol) of octylamine, or 0.5 mmol of each. The resulting mixtures were heated on a hotplate at a minimum temperature required to give transparent solutions (~100 °C). The resulting solutions were added to capillaries directly from hot solution and allowed to cool within the capillary. The SAXS patterns of capillaries were then collected on SAXSLab Ganesha instrument with Cu Kα

radiation. The same preparation was also used to prepare synthetically relevant concentration of 0.2 M solutions of $Zn(OAc)_2$ in various amine mixtures. At these concentrations, solutions were transparent free-flowing liquids at room temperature.

3.6.2. Existence of lamellar phases in 1:2 metal-amine gels.

As expected, the metal-amine complexes dissolved at high concentrations were solids at room temperature. These complexes are known to form lamellar structures composed of 2D arrays of $MX_2(RNH_2)_2$ stoichiometry. For both oleylamine and octylamine derived structures, we observed (00*l*) peaks due to lamellar structuring (Figure 3.9a). Here we demonstrate clear evidence that $ZnOAc_2$ combined with 2 equivalents of primary amine yields a lamellar phase. Additionally, the octylamine complex shows multiple doublet peaks in the wider angle (higher q) regions of the scattering pattern (WAXS) (Figure 3.9a). This observation is likely owing to incomplete solubility of zinc acetate and/or formation of oxide species. The secondary peaks observed for oleylamine can likely be attributed to other primary amine species, which we expect to be present in some meaningful concentration in technical grade surfactant.

Amine-bilayer templates probed in the medium-angle region of X-ray scattering pattern or "MAXS" region demonstrated sharper resolution of the lamellar peaks for oleylamine complex (Figure 3.9b). Clear lamellar peaks are demonstrated and small broad peaks likely correspond to the common primary amine impurities in oleylamine (Figure 3.9b). Because of the sharpness of the features, MAXS region was utilized for the diagnostic *in situ* studies in Figure 3.8d. Unfortunately, this region of the spectra would only demonstrate one sharp peak for octylamine and would not definitively show erosion of lamellar type peaks.

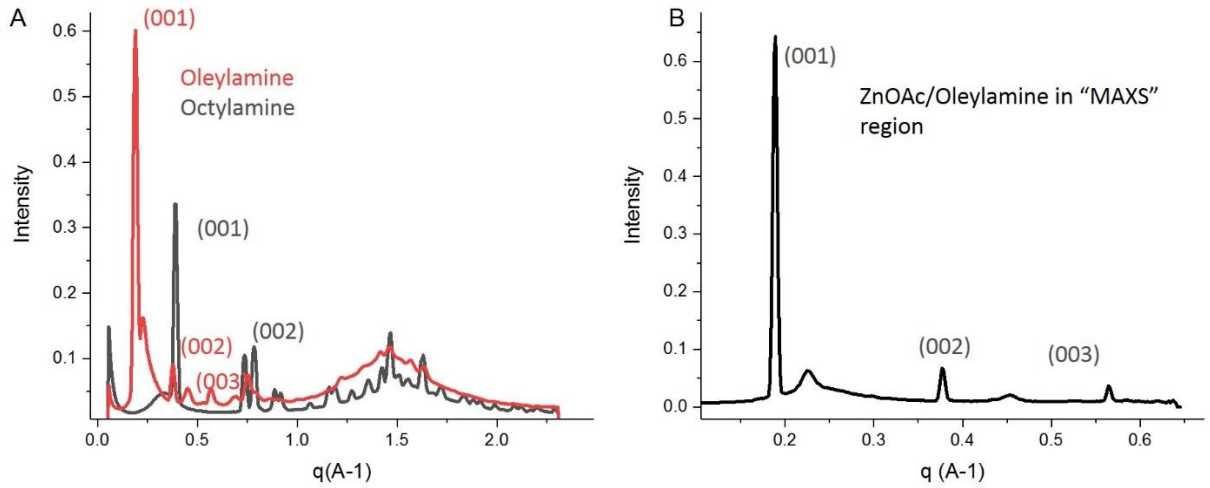

Figure 3.9. Evidence for formation of metal-amine bilayer complexes from X-ray scattering patterns: (a) WAXS pattern of gel-complexes shows impurities from other amines and other metal complex species. Indexes of lamellar peaks are added for each of the representative peaks. (b) X-ray pattern in the "medium-angle" or MAXS region for oleylamine shows sharper resolution of (00*l*) peaks with impurities likely from zinc complexed with C12-C16 primary amine impurities.

3.6.3. Additional in situ heating experiments of Zn-amine lamellar phases

The concentrated gels were first measured at room temperature (25-50 °C) to determine if there was lamellar structuring. In general, capillaries were slowly heated using a Linkam HFS Probe Stage at a rate of 5 °C/min and briefly scanned upon reaching their final temperature. The samples were allowed to equilibrate for ~10 mins when heating and cooling before measuring the representative scan at each temperature point. Our preliminary measurements on 1:2 Zn-amine gels demonstrated that, in both octylamine and oleylamine, the sharp lamellar features dissolve into a single broad background feature (Figure 3.10). This transition occurs at some temperature above 50 °C but below 100 °C (Figure 3.10). From Figure 3.8d we know that for an oleylamine complex, this transition occurs at around 60 °C, indicating that even at high concentration of zinc, a templated structure is not observed at synthetically relevant temperatures.

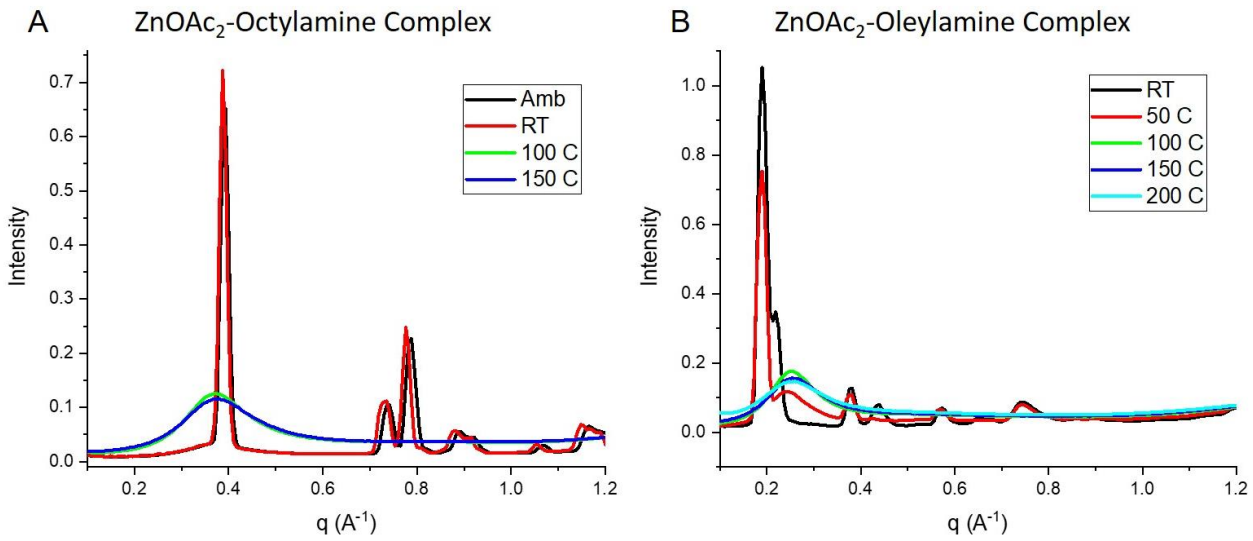

Figure 3.10. In situ heating profiles from wide angle X-ray scattering patterns of $Zn(OAc)_2$ complexed in two molar equivalents of primary amine complexes: (a) octylamine and (b) oleylamine.

Furthermore, the absence of clear lamellar structured templates is supported by experiments done at synthetically relevant concentrations. In our highest concentration synthesis, we typically use 0.2 M concentration of $Zn(X)_2$. In WAXS pattern, these dissolved complexes appear as very broad peaks with additional solvent component (Figure 3.11). The broad peaks likely correspond to the irregular shape of the metal-amine complex and their peak position of qualitatively scales with the molecular length of whatever mixture is present (Figure 3.11). Negligible change is observed in the feature profile upon heating of one sample—the peaks broaden and shift to lower q indicating some increasing disorder of the dissolved complex (Figure 3.11).

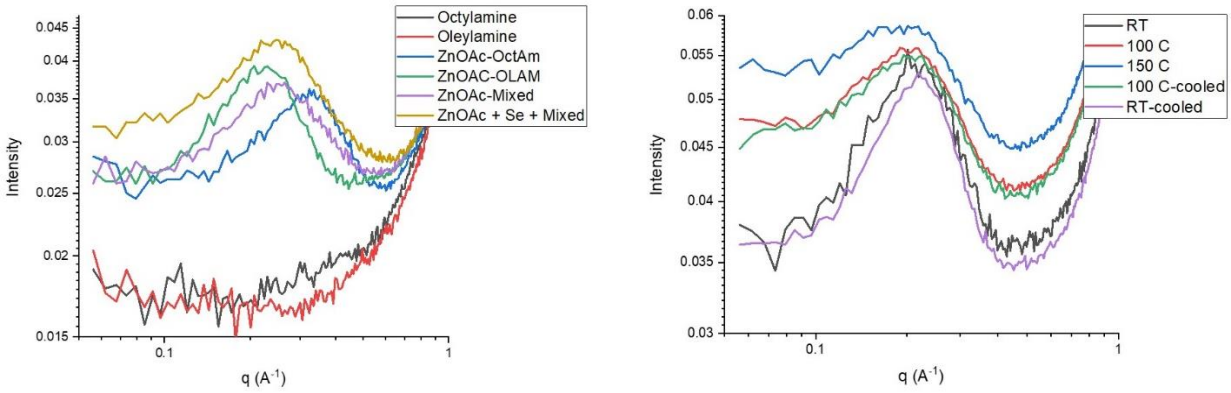

Figure 3.11. Wide angle X-ray scattering patterns of $Zn(OAc)_2$ dissolved in 0.2 M concentration for various amines: (a) Uncorrected structural peaks from Zn-amine complex shown at room temperature with neat oleylamine and octylamine shown for reference. (b) Uncorrected structural peaks for oleylamine sample heated and cooled to 150 °C and back to room temperature.

3.7. **Sequential ripening from 4 to 5 ML platelets**

As we increase reaction temperature, a more rapid transition to 4 ML platelets can be achieved. This protocol is typically employed for batches of colloidally stable platelets. Interestingly, when high concentration is maintained, we often see a transition to 5 ML nanoplatelet species. For this system, the time evolution of the absorption spectra reveals that 291 nm species are formed and then a high concentration of 4 ML species is rapidly observed upon heating to 150 °C (Figure 3.12a). Once saturation of 4 ML species is reached, we begin to see the formation of 5 ML species until they are only species present after 20 hours Figure 3.12a). Similar to the Norris model for sequential ripening,[21] a stage of the reaction is observed where the normalized absorption of 4 and 5 ML species is in steady-state (Figure 3.12b). This stage is believed to be in the regime where 5 ML species have nucleated from dissolving 4 ML species and where rate of lateral growth for the 4 ML species is equal to the rate of dissolution to generate new species. This effect can be observed through TEM of the aliquots along this stage of the reaction (Figure 3.12c). Interestingly, these images show increasing lateral growth with

increasing presence of species which have unique morphology, indicative of formation of 5 ML quasi-2D structures (Figure 3.12c). In summary, our current model interprets the quantized-growth of platelets as a surface-reaction limited pathway where the formation of initial atomically precise species governs the thermodynamic ripening process into subsequent populations.

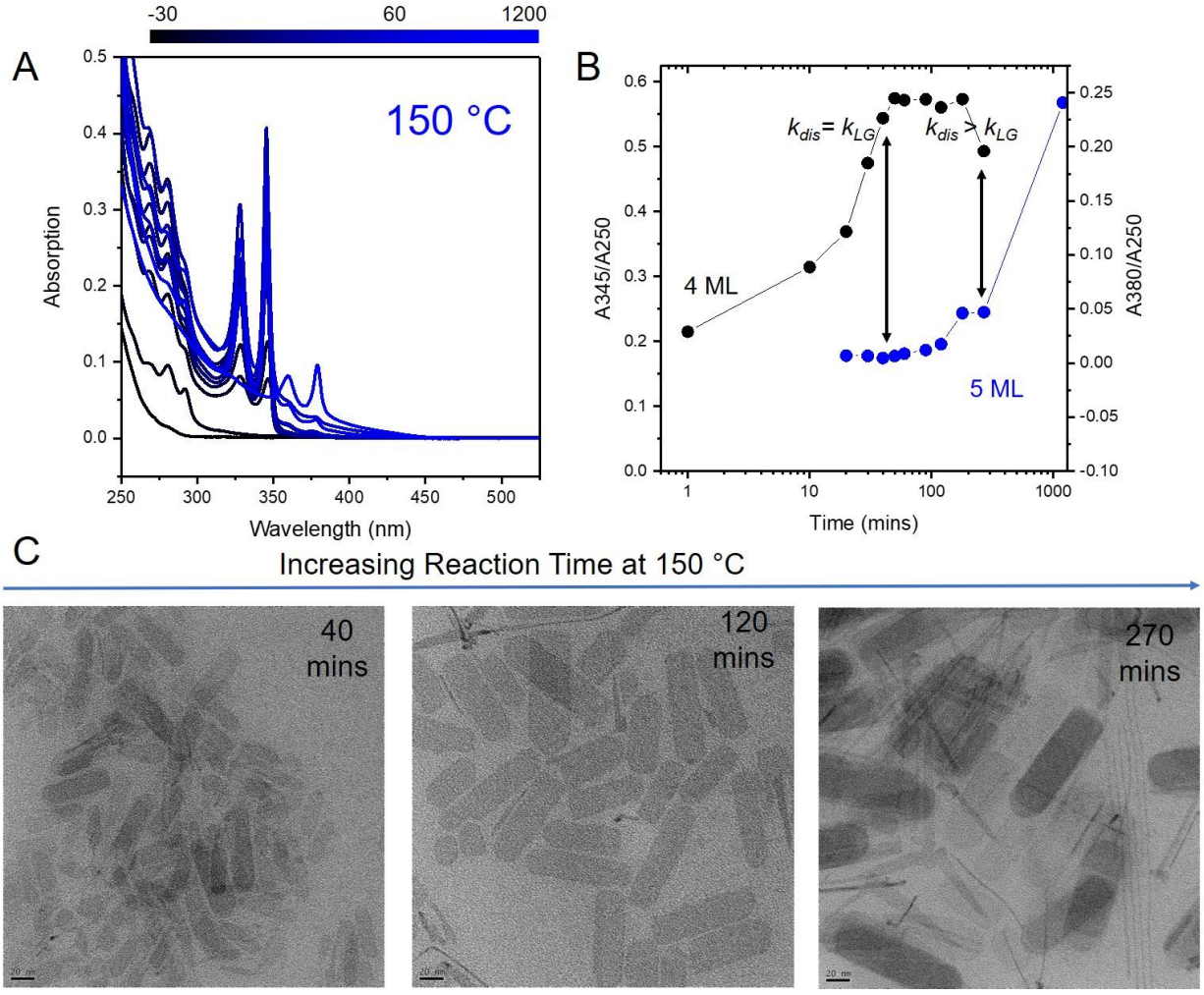

Figure 3.12. High temperature lateral growth and sequential ripening of 4 ML platelets: (a) Temporal evolution of atomically precise species in the absorption spectra. (b) Analysis of absorption features for 4 and 5 ML populations normalized to their absorption at 250 nm with respect to reaction time. (c) TEM analysis of populations containing both sets of 4 and 5 ML species demonstrates lateral platelet growth and increased presence of new species.

Kinetic studies of heat-up synthesis to higher temperatures reveal evidence that we bypass the critical temperature for surface-reaction-limited pathway and eventually destroy the atomically precise features in the absorption spectra (Figure 3.13a). Unsurprisingly, we see polymorphic species resembling small dots and wires with neglible platelet morphology present (Figure 3.13b). The pathway to metastable 5 ML platelet formation is likely bypassed at these temperatures such that when the next sequential set of nuclei form, the reaction falls under diffusion-control.

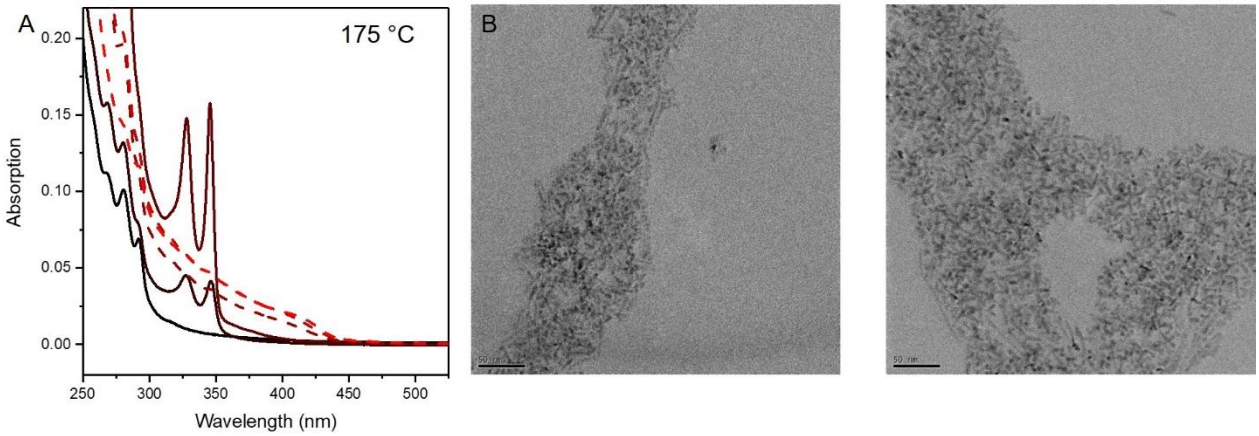

Figure 3.13. Highest temperature heat-up synthesis: (a) Temporal evolution of absorption spectra shows initial formation of atomically precise species and subsequent loss of atomic precision. (b) TEM images of final samples.

3.8. **Temperature dependence of anisotropic growth**

We sought to come up with a general explanation for these different end products. From prior knowledge, it is known that nanoparticle growth takes place in two distinct steps, and is therefore dependent on two rates. The first is rate of diffusion from solution to particle surface. The second is the reaction of monomer at the surface of the nanoparticle. Thus, if the rate of diffusion is limited, the rebecomes dependent on the diffusion of reactants within the solution. Alternatively, if the diffusion process is faster than the reaction, the reaction is controlled by the

surface reactivity of the substrate. The kinetics of diffusion- and surface-reaction-limited has been given impressive treatment by Norris et. al. as an explanation for why some reaction conditions lead to quantum dots and other conditions lead to nanoplatelets.[20] In this two-step process, diffusion from solution to the crystal surface *i*, can be described in the following equation:

$$r_{diff,i} = -D\frac{(c_{surf,i} - c_{\infty})}{\delta}$$

Where D, δ, cinf, and csurfi, represent the diffusion coefficient in solution, the diffusion-layer thickness, the monomer concentration far from the surface, and monomer concentration at the surface, respectively.

The surface reaction itself can be given by a general *n*th-order reaction:

$$r_i = c_{surf,i}^{n} k_{surf,i}$$

Where $k_{surf,i}$ is the surface-reaction constant. This discussion by Norris indicates that in the diffusion-limited case, the growth rates for all surfaces are given by $D\frac{c_{\infty}}{\delta}$. Whereas for the surface-reaction-limited case we have a reaction rate for any generic facet *i:*

$$r_i = c_{\infty}^{n} k_{surf,i}$$

Although this treatment explains the existence of facet-specific growth in certain rate-limited regimes, we must account for the apparent temperature dependence of the two processes. If these steps are limiting regimes of the kinetics, then there must exist a crossover where, depending on experimental conditions, particle nucleation and growth falls under diffusion- or surface-reaction-control. In the case of ZnSe nanocrystals, the presence of some critical temperature where crossover from anisotropic to isotropic growth has been demonstrated experimentally (Figure 3.1). For a generic nanocrystal reaction, we expect the nucleation and growth pathways to follow simple theory for an activated complex. Thus, both rate constants for diffusion and

surface reactions can be idealized using a generic Arrhenius-type relationship, with a linear relationship of the logarithm of rate constant on inverse temperature (Figure 3.14). For a given set of monomers and concentrations, it is proposed that both steps of the reaction have different activation energies and could be characterized by the slope of their Arrhenius plots (Figure 3.14). The intersection of the two plots would reveal the critical temperature in which both rates are identical. Ultimately, when the reaction remains below the critical temperature, particles have facet-specific growth, leading to quasi-2D structures. Consequently, as temperature is increased, the rate limiting step of the reaction is diffusion to the nanocrystal surface and has no facet-specificity. This crossover also suggests there is a region where both reactions are relevant, leading to thermodynamically favorable diffusion-controlled ripening/aging pathways in anisotropic starting materials.

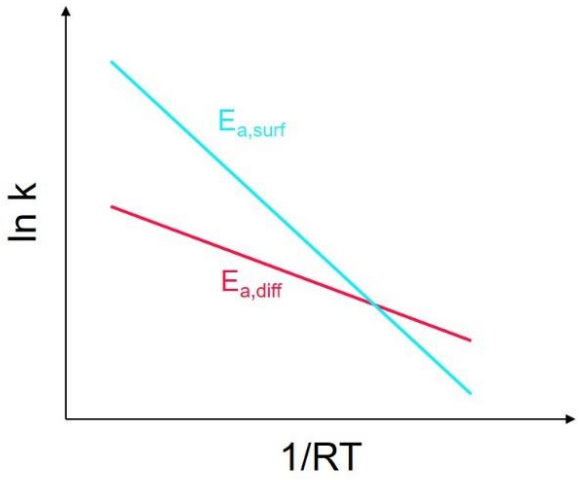

Figure 3.14. Idealized Arrhenius plot for two distinct steps in nanocrystal synthesis. The slopes reflect a difference in activation energy for each step and a temperature crossover.

3.9. **Supporting mechanistic evidence**

Various pieces of information helped govern our understanding of the system. Often the presence of "nanojunk," loss of morphological control, and intractable powders served to improve our understanding of the existing parameter space and the dead ends going forward.

3.9.1. Discovery of the new species

Our first indication of the transition from 4 ML to 5 ML species came from our first observed reaction where we obtained "impurities." In most synthesis, the 4 ML species with first exciton demonstrated at 345 nm were obtained in relatively high purity with increasing yields at longer reaction times. However, the route to another batch of platelets was discovered when the temperature was allowed to rapidly overshoot. The batches obtained by attempting to reproduce this synthesis yield a similar set of species but with a mixture of our original "345 nm" and new "375 nm" species (Figure 3.15a). Our first discovery of the possible phase change was discovered by comparing PXRD patterns between our standard population of wurtzite platelets and both of these new batches obtained by faster heat up synthesis (Figure 3.15b). Surprisingly, evidence of a phase change from the hexagonal wurtzite structures to cubic zinc-blende species was observed (Figure 3.15b). This prompted us to consider what parameters and mechanisms were responsible for the formation of these species. The primary evidence for our previously discussed ripening mechanism came from this phase change as well as very different appearance of the final "375 nm" platelet products (Figure 3.15c). From this data, we posited that the rapid increase in temperature for this heat-up synthesis changed the growth parameters by increase the relative concentration and subsequent reactivity of selenium species.

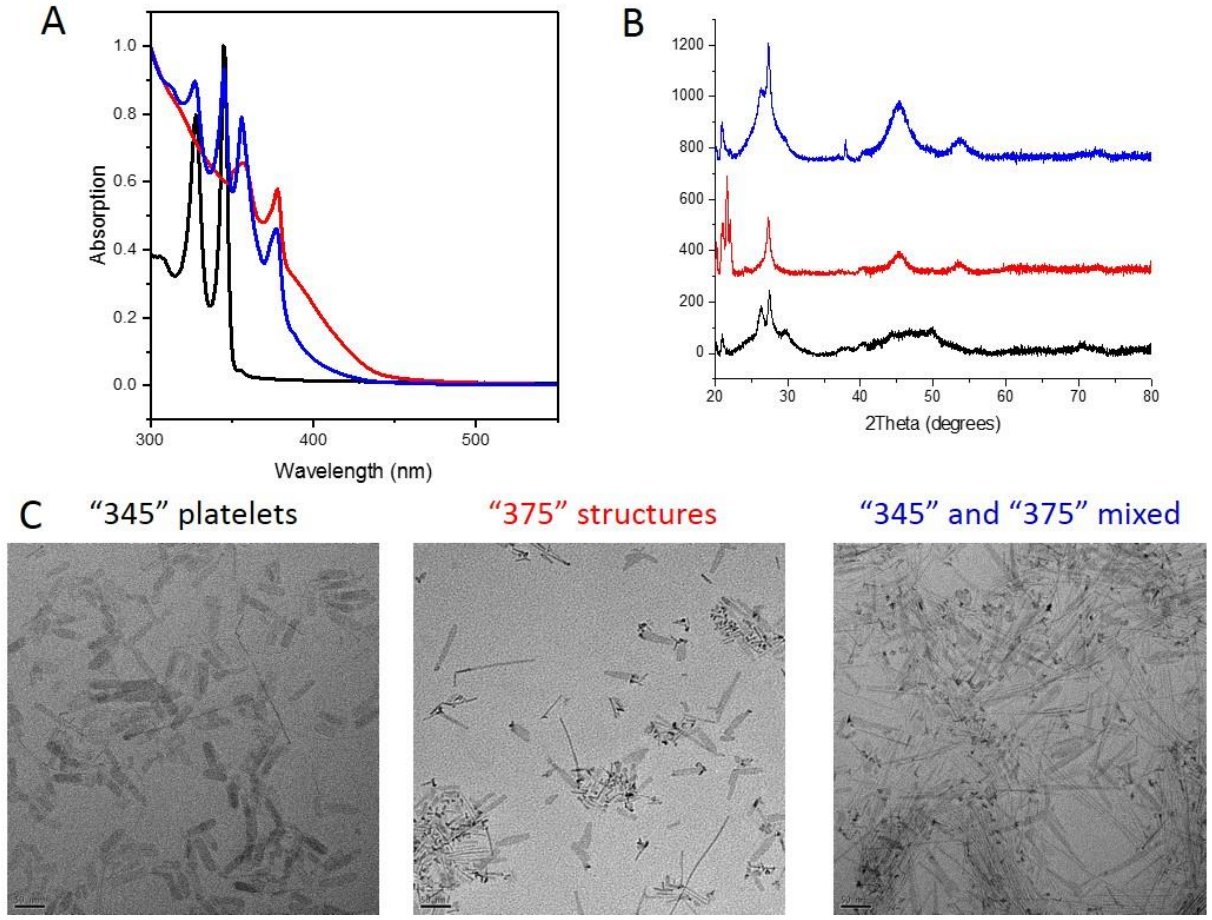

Figure 3.15. Different mixtures of platelets discovered due to accidental overshoot of "standard" reaction temperature: (a) Absorption spectra demonstrate various mixtures of the different populations of platelets obtained. (b) Powder X-Ray diffraction patterns (coded by color to spectra in (a) show key differences in crystal structure indicating phase difference between two species. (c) TEM of each different isolated set of populations from each synthesis.

3.9.2. Active selenium species determines growth pathway.

The typical heat up synthesis relies on one or both of the species become active upon reaching some critical temperature. The conversion to the active precursor drives the forward pathway of that reaction and the subsequent conversion to monomer nucleation or growth.[38] Thus, for our reaction we have several pathways to consider. First, the Zn species must be dissolved and complexed by the surrounding amine mixture, which is done in a facile manner at

moderately low temperatures. However, this synthesis is reliant on the introduction of elemental selenium into the reaction mixture:

$ZnX_2 + Se{:}(NH_2R) \rightarrow (ZnSe)_n(NH_2R)$

$Se\ (s) + NH_2R \leftrightarrow Se{:}NH_2R$?

Our reaction suspected to occur with two equivalents of selenium because our dispersed selenium behaves in the following reaction with amine mixture:

$2Se\ (s) + NH_2R\ (l) \leftrightarrow Se{=}CRNH_2\ (l) + H_2Se\ (l)$

This pathway is postulated in the literature on dissolution of sulfur in primary amines.[39] In this case we form selenoamide byproducts and our active hydrogen selenide which is likely complexed with surrounding media. It is unknown if this highly reactive species has rapid diffusion from the solution or if further side reactions proceed to species like selenium clusters. It most likely that this adduct behaves as the active species for our heat up synthesis of ZnSe nanoparticles.

With this hypothesis, it was proposed to introduce additional selenium to the reaction mixture after 4 ML platelets had formed. This introduction would likely induce an infusion of active selenium species and potentially react with the platelets and remaining Zn-complex in solution. Somewhat surprisingly, this infusion created quasi-2D structures with very narrow absorption at 380 nm and a final sample containing some larger “nanojunk” species (Figure 3.16). We sought to understand the kinetics and favorable conditions for this selenium addition.

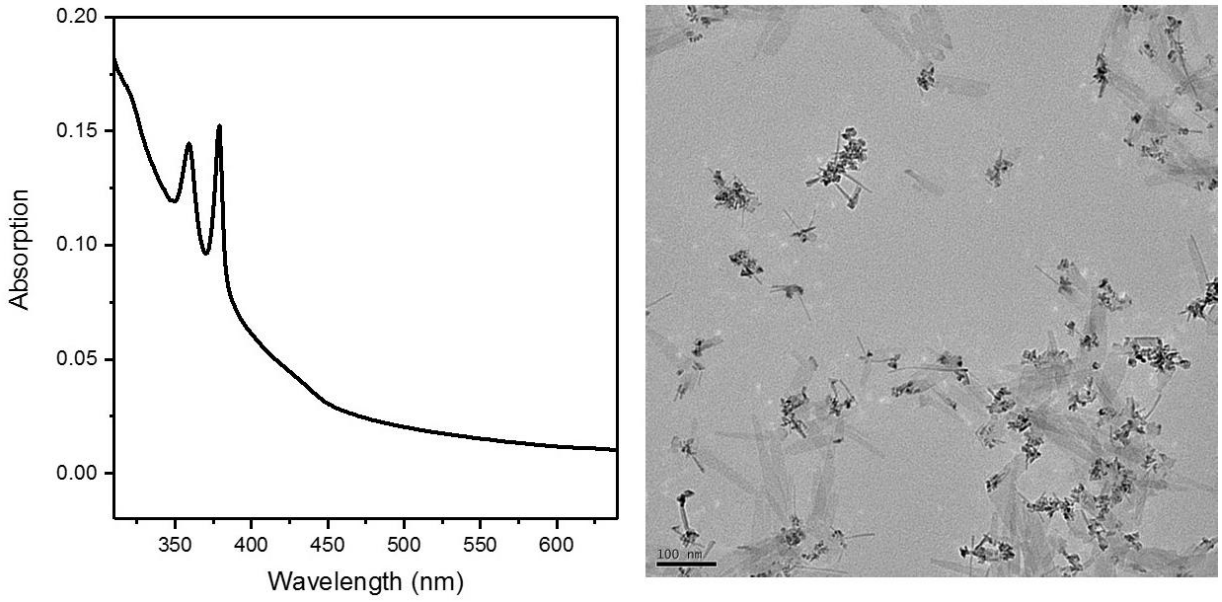

Figure 3.16. First evidence that pure nanoplatelets with exciton at 380 nm can be synthesized in a controllable manner. Absorption spectra shows narrow features with a broad onset and corresponding TEM image shows high contrast areas with a large fraction of "nanojunk."

An understanding of the role of selenium introduction was further probed in order to understand its role in the transition to 5 ML NPLs. Some reactive intermediate is likely responsible for this transition and we sought to understand the identity of this intermediate to better tailor the kinetics for the formation of monodisperse NPLs. In one such case, we preformed 345 NPLs and added TOP in order to slow the reactivity of any selenium species. Interestingly, we noticed two sharp peaks at 270 and 280 nm (Figure 3.17a). Se was then introduced to the system and we saw the decrease in optical density of these peaks relative to the sharpness of the scattering tail (Figure 3.17a). The decrease in the concentration of the intermediate is connected to the increase in concentrate of the 380 species. We sought to understand the identity of this species by dissolving our two precursors separately in primary amine at high temperatures. By dissolving Se in oleylamine, we see that these two peaks are indicative of some reactive Se cluster or intermediate (Figure 3.17a). We also dissolved zinc

stearate in oleylamine at high temperature, to confirm that the features were coming from Se only. The Zn precursor in oleylamine shows negligible features (Figure 3.17b). These pre-formed species can be combined and immediately yield atomically precise ZnSe species (Figure 3.17b). The influx of this species is likely responsible for kinetically driven growth of additional monolayers.

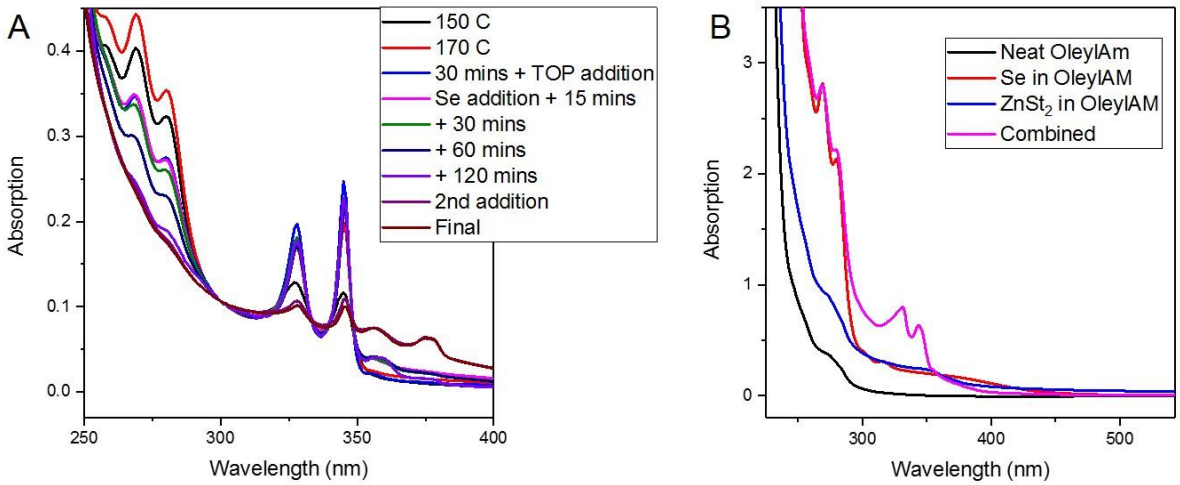

Figure 3.17. Role of dissolved selenium in NPL transition: (a) Observation of depleting features are 280 nm coinciding with the formation of the next set of 5 ML nanoplatelets. (b) Dissolution of individual precursors compared to reaction mixture and neat oleylamine.

We sought to study this in a more systematic way by measuring the temporal evolution with respect to added selenium. When we add selenium shot in large excess, transition to 5 ML platelets occurs in less than 4 hours, with large tail coming from junk species (Figure 3.18a). The presence of bulk ZnSe in the solution can be observed by the yellow color that evolves (Figure 3.18a, inset). When that excess is doubled yet again, we see an even faster transition in 80 mins (Figure 3.18b). This observation means that it is likely the dissolution kinetics of added selenium or presence of heterogenous selenium powder which plays some effect in concentrating growth. It was also observed that the faster transition lead to less tail in the absorption and optically clear

solutions (Figure 3.18b and inset). When we compare relative peak evolution as a proxy for the kinetics for this transition we clearly see that the reaction goes to completion on a faster time scale (Figure 3.18c). However, when another set of high concentration addition was attempted, we noticed less reproducible timescales, likely due to the differences in the amount of reactive selenium already available in solution.

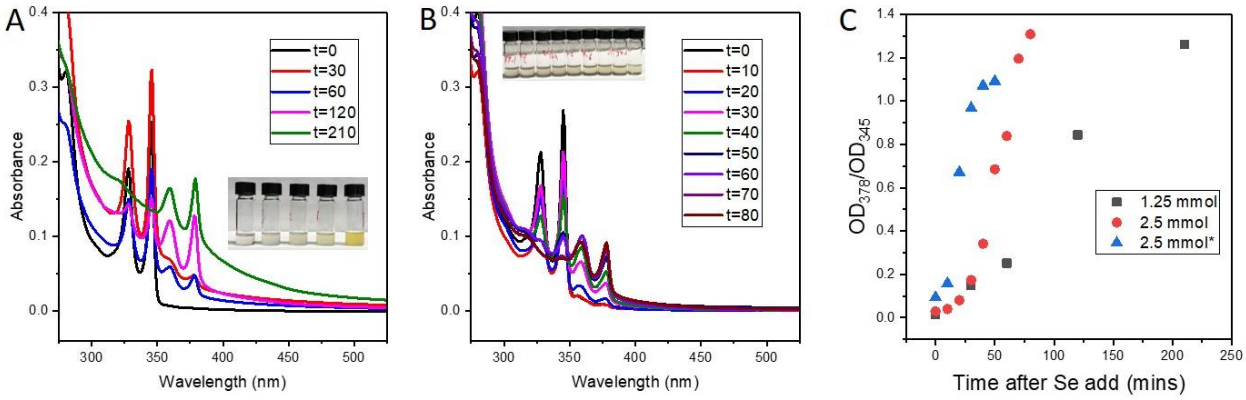

Figure 3.18. Addition of selenium shot yields transition which is faster with respect to the amount added: (a) Evolution of 380 nanoplatelets after addition of 100 mg (4 eqs w.r.t. starting Zn) Se shot. Inset shows photo of aliquots at each time point. (b) Same evolution after addition of 200 mg Se shot with similar inset photo. (c) Time dependence of the relative optical density of "380" NPLs versus the starting "345" NPLs.

3.9.3. Possible effect of Zn-precursor and counter-ion

Another synthetic attempt was performed using $Zn(NO_3)_2$, which should be more labile and avoid the presence of carboxylates in synthesis. During our synthesis, we first see our atomically precise intermediate form with absorption and 290 nm (Figure 3.19a). During the ramp to 170 °C and subsequent growth, we see a quantitative transition to strictly 345 nm species (Figure 3.19a). At the completion of this phase, 0.5 mmol of Se powder in 1 mL octylamine was injected over the course of 5 mins. After this injection, we see negligible transition and after allowing the reaction to proceed for 1 hr we see peaks beginning to form. At this time and

identical injection was added slowly and reaction was allowed to proceed for 18 hrs. Surprisingly, we do not see a complete transition after a full 18 hours (Figure 3.19a). The resulting mixture shows the presence of long wires and ribbons morphologies (Figure 3.19b). It is likely that there are very specific kinetic parameters that are necessary to achieve and complete reaction in a way that preserves the nanoplatelet morphology. It cannot be ruled out that impurities in Zn-based precursors may play some sort of role (acid-catalysis, other cations disrupting growth). In order to further understanding all mechanisms of formation and subsequent transitions for ZnSe-based structures, the nature of the reactive intermediates, as well as the temperature, time, and concentration dependence of each of these processes must be targeted in the future.

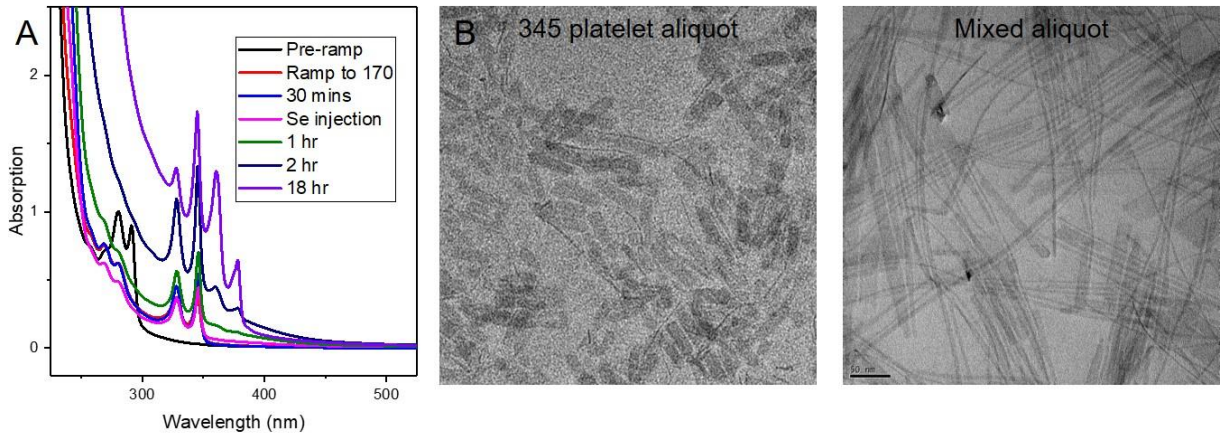

Figure 3.19. Characterization of attempted 380 synthesis with $Zn(NO_3)$ over 18 hours reaction time: (a) Absorption spectra showing a slow and incomplete transition from 345 to 380 nm species. (b) TEM images of the resulting structures of the pure "345 nm" aliquots and the final mixed end product.

3.10. **Conclusions**

Using the same simple set of precursors, ZnSe nanostructures of varying dimensionality can be grown depending on differences in the temperature profiles of the reaction. In the lower

temperature modes of the pathway, quantized growth is observed and the kinetically trapped products can be isolated as cluster mesophases, wires, and two species of quasi-2D nanostructures. The discrete 2D nanostructures have narrow PL linewidth and can be added to the available group of narrow linewidth NPL emitters with potential for display applications (Figure 3.20). Understanding the growth and mechanism is important to the optimization of their synthetic protocols for these applications. In this work, we determined that growth and ripening processes are determined by a surface-reaction-limited pathway in the range of 100-170 ºC. This growth occurs absent a template and is part of a complex reaction coordinate in which the likely thermodynamic end product is bulk ZnSe.

This chapter and future work detailing the mechanistic understanding of nucleation and growth mechanisms in ZnSe nanostructure synthesis are currently a manuscript in preparation.

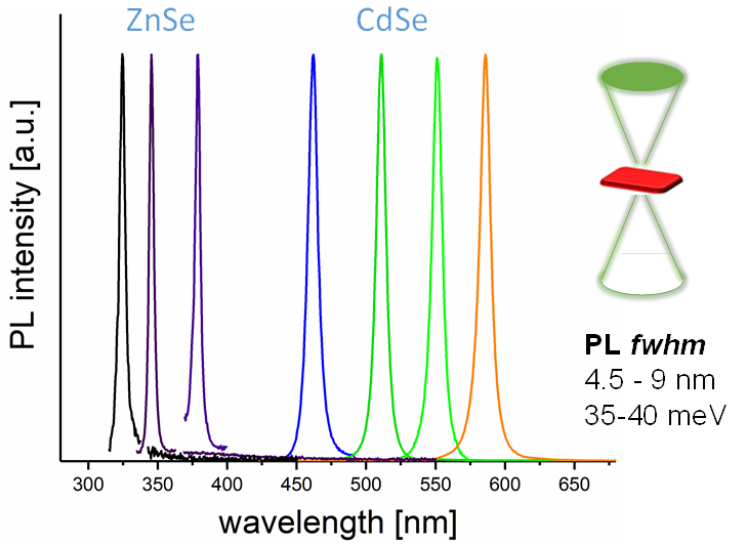

Figure 3.20. Emission spectra of ZnSe and CdSe nanoplatelets. The development of ZnSe NPLs can be added to the existing class of narrow emitting materials. The atomistic precision along the direction of quantum confinement allows achieving unprecedentedly narrow emission spectra. In addition to high color purity, NPLs support the in-plane orientation of the transition dipole favorable for light outcoupling in the direction normal to NPL surface.

3.11. **References**

1. Yin, Y.; Alivisatos, A. P., Colloidal nanocrystal synthesis and the organic–inorganic interface. *Nature* **2004,** *437*, 664.

2. Nasilowski, M.; Mahler, B.; Lhuillier, E.; Ithurria, S.; Dubertret, B., Two-Dimensional Colloidal Nanocrystals. *Chemical Reviews* **2016,** *116* (18), 10934-10982.

3. Ithurria, S.; Tessier, M. D.; Mahler, B.; Lobo, R. P. S. M.; Dubertret, B.; Efros, A. L., Colloidal nanoplatelets with two-dimensional electronic structure. *Nature Materials* **2011,** *10*, 936.

4. She, C.; Fedin, I.; Dolzhnikov, D. S.; Demortière, A.; Schaller, R. D.; Pelton, M.; Talapin, D. V., Low-Threshold Stimulated Emission Using Colloidal Quantum Wells. *Nano letters* **2014,** *14* (5), 2772-2777.

5. Scott, R.; Heckmann, J.; Prudnikau, A. V.; Antanovich, A.; Mikhailov, A.; Owschimikow, N.; Artemyev, M.; Climente, J. I.; Woggon, U.; Grosse, N. B.; Achtstein, A. W., Directed emission of CdSe nanoplatelets originating from strongly anisotropic 2D electronic structure. *Nature Nanotechnology* **2017,** *12*, 1155.

6. Gao, Y.; Weidman, M. C.; Tisdale, W. A., CdSe Nanoplatelet Films with Controlled Orientation of their Transition Dipole Moment. *Nano letters* **2017,** *17* (6), 3837-3843.

7. Tessier, M. D.; Mahler, B.; Nadal, B.; Heuclin, H.; Pedetti, S.; Dubertret, B., Spectroscopy of Colloidal Semiconductor Core/Shell Nanoplatelets with High Quantum Yield. *Nano letters* **2013,** *13* (7), 3321-3328.

8. Wang, Y.; Zhang, Y.; Wang, F.; Giblin, D. E.; Hoy, J.; Rohrs, H. W.; Loomis, R. A.; Buhro, W. E., The Magic-Size Nanocluster (CdSe)(34) as a Low-Temperature Nucleant for Cadmium Selenide Nanocrystals; Room-Temperature Growth of Crystalline Quantum Platelets. *Chemistry of Materials* **2014,** *26* (7), 2233-2243.

9. Ithurria, S.; Dubertret, B., Quasi 2D Colloidal CdSe Platelets with Thicknesses Controlled at the Atomic Level. *J. Am. Chem. Soc.* **2008,** *130* (49), 16504-16505.

10. Joo, J.; Son, J. S.; Kwon, S. G.; Yu, J. H.; Hyeon, T., Low-Temperature Solution-Phase Synthesis of Quantum Well Structured CdSe Nanoribbons. *Journal of the American Chemical Society* **2006,** *128* (17), 5632-5633.

11. Yu, J. H.; Liu, X.; Kweon, K. E.; Joo, J.; Park, J.; Ko, K.-T.; Lee, D. W.; Shen, S.; Tivakornsasithorn, K.; Son, J. S.; Park, J.-H.; Kim, Y.-W.; Hwang, G. S.; Dobrowolska, M.; Furdyna, J. K.; Hyeon, T., Giant Zeeman splitting in nucleation-controlled doped CdSe:Mn2+ quantum nanoribbons. *Nature Materials* **2009,** *9*, 47.

12. Son, J. S.; Wen, X. D.; Joo, J.; Chae, J.; Baek, S. i.; Park, K.; Kim, J. H.; An, K.; Yu, J. H.; Kwon, S. G.; Choi, S. H.; Wang, Z.; Kim, Y. W.; Kuk, Y.; Hoffmann, R.; Hyeon, T., Large-Scale Soft Colloidal Template Synthesis of 1.4 nm Thick CdSe Nanosheets. *Angewandte Chemie International Edition* **2009,** *48* (37), 6861-6864.

13. Liu, Y.-H.; Wang, F.; Wang, Y.; Gibbons, P. C.; Buhro, W. E., Lamellar Assembly of Cadmium Selenide Nanoclusters into Quantum Belts. *Journal of the American Chemical Society* **2011,** *133* (42), 17005-17013.

14. Liu, Y.-H.; Wayman, V. L.; Gibbons, P. C.; Loomis, R. A.; Buhro, W. E., Origin of High Photoluminescence Efficiencies in CdSe Quantum Belts. *Nano letters* **2010,** *10* (1), 352-357.

15. Wang, F.; Wang, Y.; Liu, Y.-H.; Morrison, P. J.; Loomis, R. A.; Buhro, W. E., Two-Dimensional Semiconductor Nanocrystals: Properties, Templated Formation, and Magic-Size Nanocluster Intermediates. *Accounts of Chemical Research* **2015,** *48* (1), 13-21.

16. Morrison, P. J.; Loomis, R. A.; Buhro, W. E., Synthesis and Growth Mechanism of Lead Sulfide Quantum Platelets in Lamellar Mesophase Templates. *Chemistry of Materials* **2014,** *26* (17), 5012-5019.

17. Wang, Y.; Zhou, Y.; Zhang, Y.; Buhro, W. E., Magic-Size II–VI Nanoclusters as Synthons for Flat Colloidal Nanocrystals. *Inorganic Chemistry* **2015,** *54* (3), 1165-1177.

18. Nevers, D. R.; Williamson, C. B.; Savitzky, B. H.; Hadar, I.; Banin, U.; Kourkoutis, L. F.; Hanrath, T.; Robinson, R. D., Mesophase Formation Stabilizes High-Purity Magic-Sized Clusters. *Journal of the American Chemical Society* **2018**.

19. Hsieh, T.-E.; Yang, T.-W.; Hsieh, C.-Y.; Huang, S.-J.; Yeh, Y.-Q.; Chen, C.-H.; Li, E. Y.; Liu, Y.-H., Unraveling the Structure of Magic-Size (CdSe)13 Cluster Pairs. *Chemistry of Materials* **2018,** *30* (15), 5468-5477.

20. Riedinger, A.; Ott, F. D.; Mule, A.; Mazzotti, S.; Knusel, P. N.; Kress, S. J. P.; Prins, F.; Erwin, S. C.; Norris, D. J., An intrinsic growth instability in isotropic materials leads to quasi-two-dimensional nanoplatelets. *Nat Mater* **2017,** *16* (7), 743-748.

21. Ott, F. D.; Riedinger, A.; Ochsenbein, D. R.; Knüsel, P. N.; Erwin, S. C.; Mazzotti, M.; Norris, D. J., Ripening of Semiconductor Nanoplatelets. *Nano letters* **2017,** *17* (11), 6870-6877.

22. Ithurria, S.; Bousquet, G.; Dubertret, B., Continuous Transition from 3D to 1D Confinement Observed during the Formation of CdSe Nanoplatelets. *Journal of the American Chemical Society* **2011,** *133* (9), 3070-3077.

23. Liu, Y.; Zhang, B.; Fan, H.; Rowell, N.; Willis, M.; Zheng, X.; Che, R.; Han, S.; Yu, K., Colloidal CdSe 0-Dimension Nanocrystals and Their Self-Assembled 2-Dimension Structures. *Chemistry of Materials* **2018,** *30* (5), 1575-1584.

24. Chen, Y.; Chen, D.; Li, Z.; Peng, X., Symmetry-Breaking for Formation of Rectangular CdSe Two-Dimensional Nanocrystals in Zinc-Blende Structure. *Journal of the American Chemical Society* **2017,** *139* (29), 10009-10019.

25. Hines, M. A.; Guyot-Sionnest, P., Bright UV-Blue Luminescent Colloidal ZnSe Nanocrystals. *The Journal of Physical Chemistry B* **1998,** *102* (19), 3655-3657.

26. Chen, H.-S.; Lo, B.; Hwang, J.-Y.; Chang, G.-Y.; Chen, C.-M.; Tasi, S.-J.; Wang, S.-J. J., Colloidal ZnSe, ZnSe/ZnS, and ZnSe/ZnSeS Quantum Dots Synthesized from ZnO. *The Journal of Physical Chemistry B* **2004,** *108* (44), 17119-17123.

27. Wang, A.; Shen, H.; Zang, S.; Lin, Q.; Wang, H.; Qian, L.; Niu, J.; Song Li, L., Bright, efficient, and color-stable violet ZnSe-based quantum dot light-emitting diodes. *Nanoscale* **2015,** *7* (7), 2951-2959.

28. Shen, H.; Wang, H.; Li, X.; Niu, J. Z.; Wang, H.; Chen, X.; Li, L. S., Phosphine-free synthesis of high quality ZnSe, ZnSe/ZnS, and Cu-, Mn-doped ZnSe nanocrystals. *Dalton Transactions* **2009,** (47), 10534-10540.

29. Yeh, C.-Y.; Lu, Z. W.; Froyen, S.; Zunger, A., Zinc-blende--wurtzite polytypism in semiconductors. *Physical Review B* **1992,** *46* (16), 10086-10097.

30. Panda, A. B.; Acharya, S.; Efrima, S., Ultranarrow ZnSe Nanorods and Nanowires: Structure, Spectroscopy, and One-Dimensional Properties. *Advanced materials* **2005,** *17* (20), 2471-2474.

31. Cozzoli, P. D.; Manna, L.; Curri, M. L.; Kudera, S.; Giannini, C.; Striccoli, M.; Agostiano, A., Shape and Phase Control of Colloidal ZnSe Nanocrystals. *Chemistry of Materials* **2005,** *17* (6), 1296-1306.

32. Carbone, L.; Nobile, C.; De Giorgi, M.; Sala, F. D.; Morello, G.; Pompa, P.; Hytch, M.; Snoeck, E.; Fiore, A.; Franchini, I. R.; Nadasan, M.; Silvestre, A. F.; Chiodo, L.; Kudera, S.; Cingolani, R.; Krahne, R.; Manna, L., Synthesis and Micrometer-Scale Assembly of Colloidal CdSe/CdS Nanorods Prepared by a Seeded Growth Approach. *Nano Lett.* **2007,** *7* (10), 2942-2950.

33. Coropceanu, I.; Rossinelli, A.; Caram, J. R.; Freyria, F. S.; Bawendi, M. G., Slow-Injection Growth of Seeded CdSe/CdS Nanorods with Unity Fluorescence Quantum Yield and Complete Shell to Core Energy Transfer. *ACS Nano* **2016,** *10* (3), 3295-3301.

34. Jia, G.; Banin, U., A General Strategy for Synthesizing Colloidal Semiconductor Zinc Chalcogenide Quantum Rods. *Journal of the American Chemical Society* **2014,** *136* (31), 11121-11127.

35. Ning, J.; Liu, J.; Levi-Kalisman, Y.; Frenkel, A. I.; Banin, U., Controlling Anisotropic Growth of Colloidal ZnSe Nanostructures. *Journal of the American Chemical Society* **2018**.

36. Park, H.; Chung, H.; Kim, W., Synthesis of ultrathin wurtzite ZnSe nanosheets. *Materials Letters* **2013,** *99*, 172-175.

37. Zhang, L.-J.; Shen, X.-C.; Liang, H.; Yao, J.-T., Multiple Families of Magic-Sized ZnSe Quantum Dots via Noninjection One-Pot and Hot-Injection Synthesis. *The Journal of Physical Chemistry C* **2010,** *114* (50), 21921-21927.

38. Kwon, S. G.; Piao, Y.; Park, J.; Angappane, S.; Jo, Y.; Hwang, N.-M.; Park, J.-G.; Hyeon, T., Kinetics of Monodisperse Iron Oxide Nanocrystal Formation by "Heating-Up" Process. *Journal of the American Chemical Society* **2007,** *129* (41), 12571-12584.

39. Davis, R. E.; Nakshbendi, H. F., Sulfur in Amine Solvents. *Journal of the American Chemical Society* **1962,** *84* (11), 2085-2090.

4. Core-shell formation and future perspectives

4.1. Introduction: Cd-free nanostructures for outcoupled blue-emission

For decades, colloidal semiconductor nanocrystals (NCs) have been attractive for optoelectronic applications due to their narrow emission and large absorption coefficient. Surface engineering and shell-growth optimization has allowed for the scaled production of stable CdSe-based quantum dots (QDs) with near unity quantum yield and ensemble linewidths limited by homogeneous broadening only. These QDs have already made their way into commercial display technologies. However, one major limitation for use of Cd-based emitters in consumer electronics is the intrinsic toxicity of the Cd^{2+} ions. Despite potential modifications of surface shell and ligand, or encapsulation leading to safe usable Cd-based QD optoelectronics, many national and international governing bodies strictly regulate the use of Cd in consumer electronics. Thus, nanocrystals without toxic heavy metal constituents (Cd, Pb, Hg) are much more likely to seamlessly penetrate the market for mass-produced electronics.

The applications of luminescent colloidal nanostructures in optoelectronic devices (LCD displays, LEDs, etc) requires integration of individual nanostructures in polymer films or multilayer device stacks. Due to internal reflections, refractions and other losses, only a fraction of the emitted light is able to leave the device to the outside world. The reason is that light is generated in a region with higher refractive index than the substrate and ambient air. This applies to QLEDs and other nanocrystal-based optoelectronic devices. Understanding and maximizing the light outcoupling efficiency for nanocrystal-based LCD and LED devices is therefore of great importance for achieving high EQE values, comparable to those in best OLED devices, with superior color purity of quantum dot emitters.

As detailed in previous sections, two-dimensional NPLs should improve the light outcoupling efficiency. According to our analysis, both quantum mechanical and dielectric effects force NPL to emit light in the direction normal to the NPL plane, which is optimal for efficient light outcoupling. The literature confirms our belief in the potential for light outcoupling in spectroscopic studies of the directional emission from CdSe NPLs.[1] The observed directed emission is related to the anisotropy of the electronic Bloch states governing the exciton transition dipole moment and forming a bright plane. The strongly directed emission perpendicular to the platelet is further enhanced by the optical local density of states and local fields. Such situation is optimal for a significant increase of the radiative outcoupling efficiency in displays or LED devices and should reduce the losses associated with coupling of emitted light to the waveguide and surface plasmon modes.

Shifting the emission of ZnSe NPLs from 380 nm to 440 nm required for blue QLED pixels corresponds to 445 meV redshift. Such shift is feasible, if we consider that CdSe/CdS NPLs show even larger red shifts. In fact, the effect of biaxial strain on the bandgap of ZnSe/ZnS NPLs is expected to be more pronounced compared to that in CdSe/CdS core-shells because of slightly larger lattice mismatch between ZnSe and ZnS (4.6% vs. 4.3% for CdSe/CdS) and significantly larger difference in the volume deformation potentials for the lowest energy conduction band minimum and the highest energy valence band maximum for Zn chalcogenides compared with Cd chalcogenides (e.g., -5.8 eV for ZnTe vs. -3.4 eV for CdTe – see ref [2]).

Section 3 demonstrated new routes to ZnSe 2D materials that can potentially be useful as cores in the next generation of emissive core-shells. Since the bulk band gap of ZnSe is very close to the blue spectral locus heavily quantum confined ZnSe will be shifted into the near UV. Indeed, our system yields 4 and 5 ML nanostructures with sub-visible emission wavelengths of

345 and 380 nm, respectively. If growth can be optimized to form discrete platelets with 380 nm first absorption, a useful scaffold for shell growth can be obtained. Since these platelets have narrow, defect free emission in the near-UV, we analyzed the efficacy of ZnS shell-growth to determine the extent of redshift into the technologically relevant wavelength.

4.2. **Synthetic control over lateral dimensions**

In the literature it is well known that large lateral dimensions in CdSe lead to higher number of surface traps and therefore lower quantum yield with respect to increasing volume.[3] However, we had limited success in finding a clear way to control particles using reaction growth times. Particle sizing was used to determine the monodispersity of lateral dimensions in ZnSe NPLs. For 345 NPLs, we measured length and width on TEM images for samples cast "face-up" from dilute methylcyclohexane (Figure 4.1a). From 125 unique platelets, it appeared that there was a small correlation between width and length—the linear fit showing an r-squared value of ~0.25 (Figure 4.1b). The sample seemed to be clustered tightly together in size with some outliers that are likely attributed to oriented attachment or fragmenting. The width, length and aspect ratio measured over 125 platelets was 13 ± 2 nm, 40 ± 13 nm, and 3.3 ± 0.9, with relative standard deviation of 17%, 30%, and 27%, respectively (Figure 4.1b). This suggests that much of the growth in the latter stages of synthesis is unidirectional.

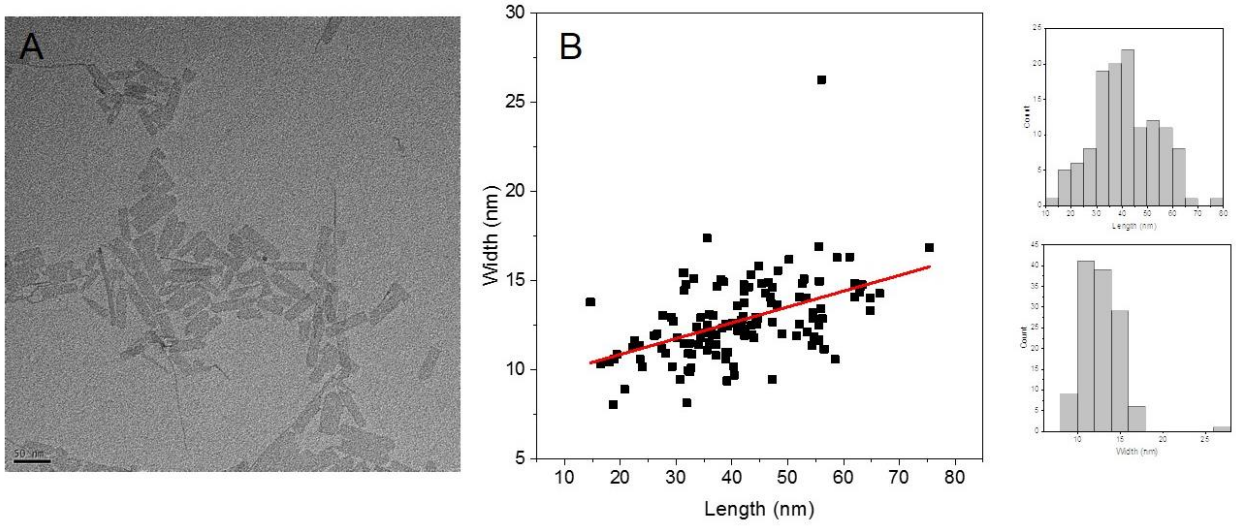

Figure 4.1. Size of lateral dimensions determined for a discrete set of well-defined 4 ML platelets: (a) TEM image of platelets used in imaging shows typical distribution of sizes. (b) Width plotted as a function of length for 125 measured platelet aspect ratios with small plots demonstrating the distribution of length and widths. The average width, length and aspect ratio were 13 ± 2 nm, 40 ± 13 nm, and 3.3 ± 0.9.

In order to better understand how to control the formation of these platelets, it was decided to determine the effect of different additives along with the Se addition to see if we can control size, purity, and shape of the platelets. It was hypothesized that the addition of $ZnCl_2$ could help provide additional precursor influx and the Cl^- anions could have some effects on the growth modes. The 345 NPLs are formed at 170 °C, as expected (Figure 4.2). TOP is added in order to quench the Se species present before further addition. After Se addition, we see no formation of 380 peaks (Figure 4.2). Additionally, the scattering tail of the synthesis increases drastically and absorbance of similar sized aliquots increases (Figure 4.2). It is likely that the addition of $ZnCl_2$ along with Se shot only contributes to the lateral or new growth of 345 NPLs. It is speculated that the $ZnCl_2$ actively consumes and Se species generated and has either rapid lateral growth or the growth of new nuclei. The final particles are practically insoluble in MCH, as demonstrated by the portion of particles that remain in supernatant at low speed

centrifugation. This supports the fact that particles have either grown sufficiently large or become bundled due to the $ZnCl_2$ addition. TEM of these species confirm increased stack as evidenced by finding them in higher contrast islands (Figure 4.3). The platelets seem to be much more monodisperse and growth along the c-axis is potentially truncated (Figure 4.3). This result has consequences on both the formation of monodisperse 345 NPLs as well as the formation of 380 NPLs. To date, we have not determined a meaningful way to control NPL size in either 4 or 5 ML platelets. Future studies should focus on tuning the reactivity and counter ions of various precursors.

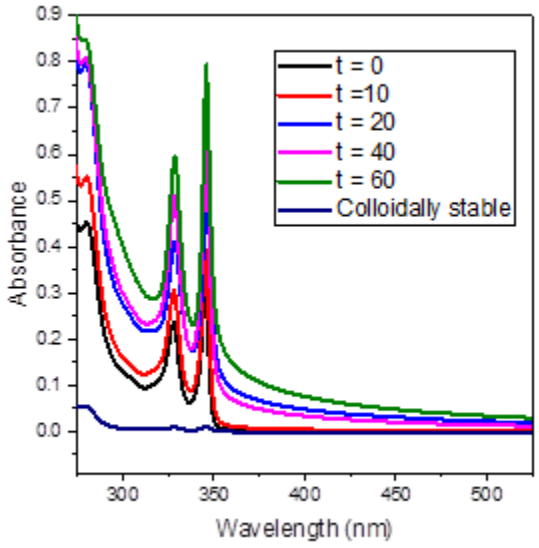

Figure 4.2. Temporal evolution of absorption after addition of Se shot immediately followed by 0.5 mmol $ZnCl_2$ in 1 mL oleylamine.

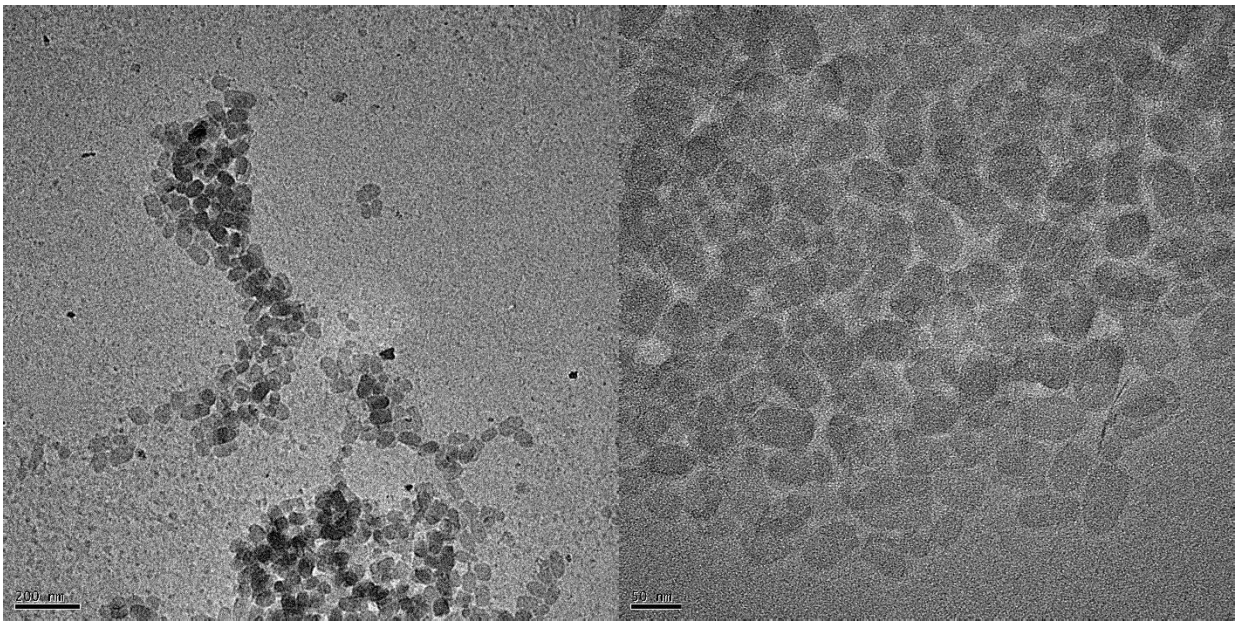

Figure 4.3. TEM images of platelets grown through $ZnCl_2$ addition after adding more Se shot.

4.3. **Theoretical band-gap analysis of core-shell structures**

In order to obtain an estimate of the possible redshift of ZnSe platelet upon growth of a ZnS shell we need to consider both the effect of strain when creating the heterostructure as well as the relaxation in confinement energy as the charge carriers can delocalize into the shell. We have thus performed a detailed analysis.

4.3.1. Effect of strain

The mismatch in the lattice constant of ZnSe and ZnS can be expected to give rise to strain in ZnSe/ZnS heterostructures. The nature of this strain will depend on the specific geometry of the heterostructure. Since the bulk lattice constant of ZnS (0.541nm) is smaller than that of ZnSe (0.567), the ZnSe core is expected to experience a contraction when overcoated with ZnS. For spherical particles this contraction will be isotropic, leading to the situation of hydrostatic strain. In contrast for ZnSe/ZnS core shell platelets the contraction in the plane of the platelet can be expected to be partly relaxed by extension along the short axis of the platelet, i.e.

the axis of quantum confinement. We can estimate the distribution of the strain using a simple continuum theory.

As a starting point we can assume the ZnSe layer is compressively strained in a symmetric fashion in the plane of the well (along the y and z axes), while it experiences strain in the axial direction (along the x axis). We can then note the strain as:

$$\varepsilon_{yy} = \varepsilon_{zz} = \varepsilon_{\parallel} \quad \varepsilon_{xx} = \varepsilon_{\perp}$$

Likewise, we assume there to be no shear stress/strain the system, such as

$$\varepsilon_{xy} = \varepsilon_{xz} = \varepsilon_{yz} = 0$$

Under these conditions the axial strain can be related to the in-plane strain using the following relationship, where c_{11} and c_{22} are elastic constants of zb-ZnSe:

$$\boldsymbol{\varepsilon_{xx} = -2\frac{c_{12}}{c_{11}}\varepsilon_{yy}}$$

As a limiting case we can study the case where a thin central ZnSe core is encased in a thick ZnS shell. Under these conditions to a first approximation we can assume that the ZnSe layer will be epitaxially matched in the lateral plane to the bulk crystal structure of ZnS. However, in the axial direction the ZnSe will be free to expand in order to relax in order to partially relieve the strain energy. Under those conditions the lateral and axial strain in the ZnSe layer will be

$$\varepsilon_{yy} = \frac{a_{ZnS} - a_{ZnSe}}{a_{ZnSe}} = -0.0459$$

$$\varepsilon_{xx} = -2 \times \frac{0.498}{0.826} \times -0.0459 = 0.0553$$

4.3.2. Shift to the band gap due to the tetragonal distortion.

We can then calculate the shift in the energy bands that will arise from this distortion. In a treatment derived in the formalism of the Bir-Pikus Hamiltonian[4], the strain will cause a shift in the relative position of the conduction band to the heavy hole band in ZnSe as given by the following relationship

$$\Delta \mathbf{E_{BG}} = \mathbf{2a}\left(\frac{\mathbf{c_{11}} - \mathbf{c_{12}}}{\mathbf{c_{11}}}\right)\boldsymbol{\varepsilon}_{\parallel} - \mathbf{b}\left(\frac{\mathbf{c_{11}} + \mathbf{c_{12}}}{\mathbf{c_{11}}}\right)\boldsymbol{\varepsilon}_{\parallel}$$

The first term accounts for the hydrostatic strain in the system and it has a positive contribution, while the second term accounts for the tetragonal distortion and it will have a negative sign. Taking the limiting case of the strain as discussed above (i.e. $\varepsilon_{yy} = 0.0428$), we obtain $\Delta E = 109meV$. The net effect is that the bandgap is still expected to increase, but less so than if only hydrostatic strain existed.

4.3.3. Contribution of the confinement energy due to the tensile strain in ZnSe core.

In addition to the shift of the band gap the energy of the exciton will also be affected by the change in the confinement potentials caused by the strain. Here we will only consider the change in confinement caused by the change in the ZnSe core, leaving the effect of delocalization into ZnS for the next section. The tensile strain in the ZnSe core along the confinement direction means that the effective width of the well will increase.[5] We can then obtain the confinement energy of the exciton from the canonical energy expression for quantum wells:

$$\boldsymbol{E_{conf}} = \frac{\hbar^2\boldsymbol{\pi}^2}{\mathbf{2}\boldsymbol{\mu}}\left(\frac{\boldsymbol{n}}{\boldsymbol{L}}\right)^2$$

In the case of the 4ML platelets, the change energy in the confinement energy in changing L by the estimated strain gives ΔE_{Conf} =-140meV

This value is slightly greater than the predicted increase in the bandgap energy, suggesting that the net effect in these platelets is to decrease the energy of the exciton by about 30meV. It is worth pointing out that such a cancellation would not happen for spherical particles, which highlights the fact that having a quasi-2D system is helpful in this case to obtain a larger redshift upon shell growth.

4.3.4. Change in confinement energy from charge delocalization into ZnS shell.

Finally, we can try to estimate the additional delocalization that will occur when growing a thicker ZnS shell. In order to get a quick estimate of the expected degree of relaxation we can split the energy of the exciton into its main contributions:

$$E = E_{band\ gap} + E_{Coulomb} + E_{confinement,hole} + E_{confinement,electron}$$

Next, we need to know the band alignment in in the heterostructure. According to all sources the valence band of ZnS lies significantly below that of ZnSe while conduction bands are much closer with estimates of the CBO ranging from 0-300meV. As a result, the heterostructure can be classified as either type-I or quasi-type-II, such that the hole will be strongly confined to the ZnSe core, while the electron can partially or completely delocalize into the ZnS shell. In light of this situation, we can largely estimate the change in the energy of the exciton simply through the reduction of the electron confinement energy upon delocalization into the

$$\boldsymbol{E_{confinement,electron} = \frac{\hbar^2 \pi^2}{2 m_e^*} \left(\frac{n}{L}\right)^2}$$

In order to obtain a rough estimate of the effect of charge delocalization we can take the simple expression above and assume the case of degenerate conduction bands (i.e. a CBO of 0) as has been used for ZnSe/ZnS epitaxial quantum wells. The result of this treatment is shown in Figure 4.4 below, which shows the expected decrease in the confinement energy of the electron and the estimated change in the optical bandgap. In this simplified scenario it appears that just a few monolayers of ZnS would suffice to push the wavelength of the platelets into a region well suited for visible display applications. In reality this redshift may happen more slowly if the conduction band offset is larger and/or if the assumptions of the simple model we used above are insufficient. However, it's known from studies of ZnSe/ZnS QDs that a significant redshift does occur upon shell growth.[6] This fact, together with the strong hypothesis that the redshift will be larger for platelets than for QDs does suggest that it can be possible to push the PL band to ~430nm by growing a thicker ZnS shell and possibly starting from a thicker ZnSe platelet (e.g. the 380nm population vs. the 345nm population).

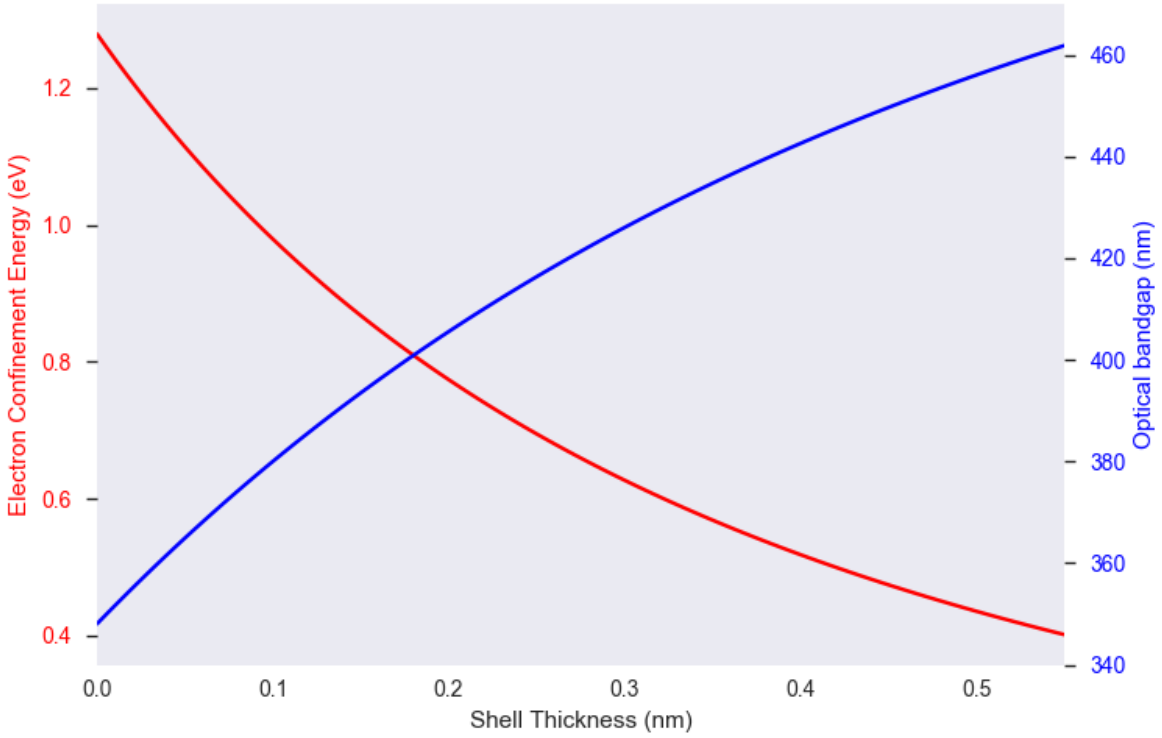

Figure 4.4. Change in electron confinement energy and the optical band gap of ZnSe/ZnS heterostructures upon ZnS growth assuming the canonical energy equation for a quantum well and an CBO of 0 eV.

Constants used:

For ZnSe:

a_0=0.567nm

a = 5.4eV[7]

b = 1.2eV[7]

c_{11} = 0.826 × 10^6kg/cm^2 [7]

c_{12} = 0.498 × 10^6kg/cm^2 [7]

For ZnS:

a_0=0.541nm

4.3.5. Acknowledgement

Special thank you to Dr. Igor Coropceanu for his help the above section.

4.4. **High-temperature ZnSe overcoating and ZnS shell growth**

Based on the above analysis, it is feasible to imagine that ZnS shell growth will not only passivate the surface of ZnSe nanocrystals to achieve higher quantum yield, but shift the emission peak into blue spectral locus. Indeed, spherical ZnSe/ZnS core-shells presented in the literature and available commercially have emission in the useful range of 430-450 nm. Additionally, it was anticipated that the techniques employed for growth of II-VI wide band gap shells on CdSe nanoplatelets would likely be translatable for a ZnSe nanoplatelet. The results from these explorations are detailed below.

4.4.1. Synthetic methods for luminescent ZnSe/ZnS core-shell spheres

Despite the initial success in synthesizing core-shells with NPL morphology, more careful optimization studies were needed. We first looked to the synthesis of spherical core-shells to better understand the limitations of our current methodologies. We opted to prepare a batch of ZnSe@ZnS spherical core-shells using a two-pot approach with syringe-pump growth and annealing. ZnSe cores were prepared by co-injection of $ZnEt_2$ and TOPSe into oleylamine followed by further syringe pump injection of the same precursors. The cores were washed and stored in the glove box and had a first exciton of 362 nm with an emission peak around 368 nm (Figure 4.5a-b). About 0.5 mL of core stock solution (20 mg nanoparticles) of in toluene was added to flask containing $ZnSt_2$, TOP, and ODE and degassed first at RT and then at 120 °C for 2 hours. Aliquots after heating to 200 °C indicated an etch of the particles with the peak position now at 352 nm (Figure 4.5a). At this point, TOPSe in ODE was added slowly while heating to

300 °C. Once the temperature had reached 300 C, there was a bright green coloration in the flask. Indeed, most of the redshift of the particles had occurred in the first 20 mins of precursor addition (Figure 4.5a-b, green curve). After completion of TOPSe addition, TOPS was slowly added. About halfway through addition of TOPS, we began addition additional Zn precursor in the form of $ZnOl_2$. The particles had a final emission peak position of 430 nm, approaching the blue spectral locus (Figure 4.5b). These facile shell-growth experiments showed that we can easily achieve bright emissive ZnSe@ZnS particles using slow-annealing of precursors.

Quantum yield with respect to time of growth and washing was measured to determine quality of the particles and long-term stability. After synthesis, we determined the brightest aliquot to crude solution in toluene after conclusion of synthesis. We measured the absolute quantum yield of 40% in the integrating sphere and compared this peak to the relative PL of several other aliquots from the synthesis (Figure 4.6). Any ZnS shelling immediately increased quantum yield from about 5-10% to 20-30% (Figure 4.6). It is possible that the cooling of the solution and small amount of Zn precursor that crashed out caused some unnecessary oxidation and/or ligand stripping. A week after isolating with toluene/methanol:butanol, acetone/hexane, and methycyclohexane/ethanol solvent pairs, the stock solutions were at least an order of magnitude quenched with respect to the brightest aliquots (Figure 4.6). Going forward, care must be taken when isolating particles with non-solvent. Precipitation with previously tested anhydrous solvents in the glovebox may be necessary to avoid issues with stability of PL. It cannot be ruled out that the oxophilicity of Zn will create quenching with respect to minimal moisture and oxygen exposure.

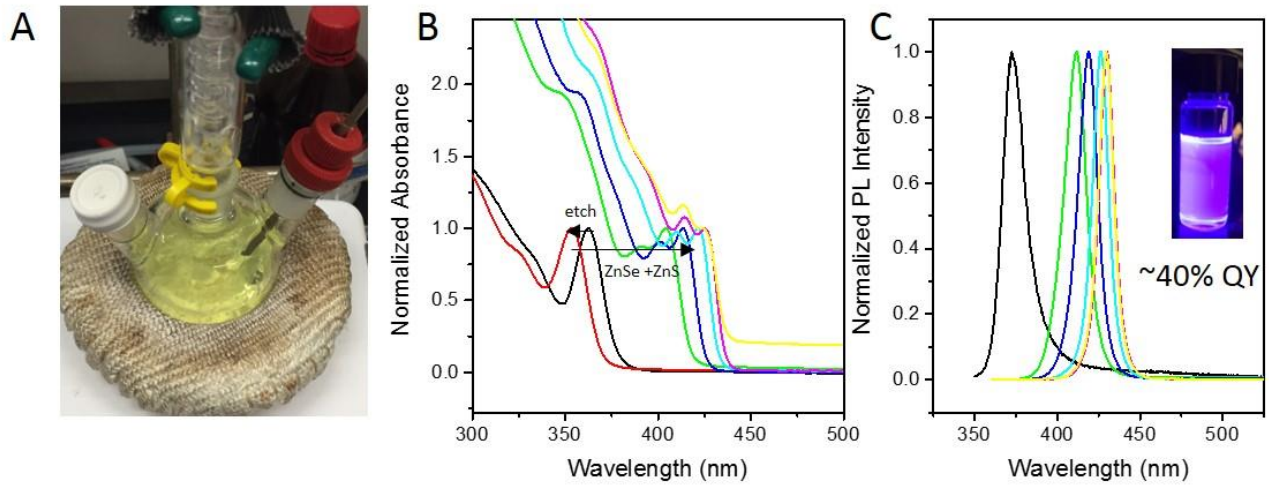

Figure 4.5. Demonstration of high quality synthesis of ZnSe/ZnS spherical core-shells: (a) Change in coloration of flask at high temperatures goes from clear to pale green as shells grow. Absorption (b) and emission (C) of ZnSe cores monitored during etch and shell growth of ZnSe and ZnS. The resulting particles were highly emissive and showed bright deep blue-violet emission under UV excitation (inset, panel c).

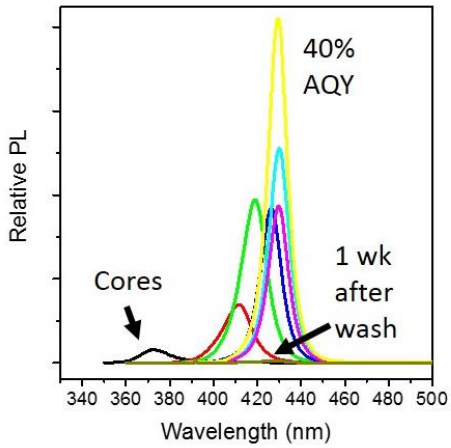

Figure 4.6. PL intensity normalized with respect to optical density and compared with highest quantum yield aliquot as measured in an integrating sphere (yellow curve).

4.4.2. Comparative studies of ZnSe and ZnS overgrowth on dots and platelets

We attempt to reproduce previous shell growth experiments using TOPSe and TOPS injection into flasks with cores, ODE, TOP, lauric acid, and $ZnSt_2$ (Figure 4.7). In both of these cases we used identical preparations with infusion over hours with a temperature rise from 170 to

250 °C. In the case of spheres, we saw a mild etch of the original starting cores with a blueshift to 376 nm (Figure 4.8a). After completion of the growth, there was a redshift of the absorption to 405 nm. The emission shifted from 390 to 415 nm with a two-order of magnitude increase in emission intensity (Figure 4.8b). The formation of these core-shells reveals that temperatures of 300 °C are not necessary for high optical quality.

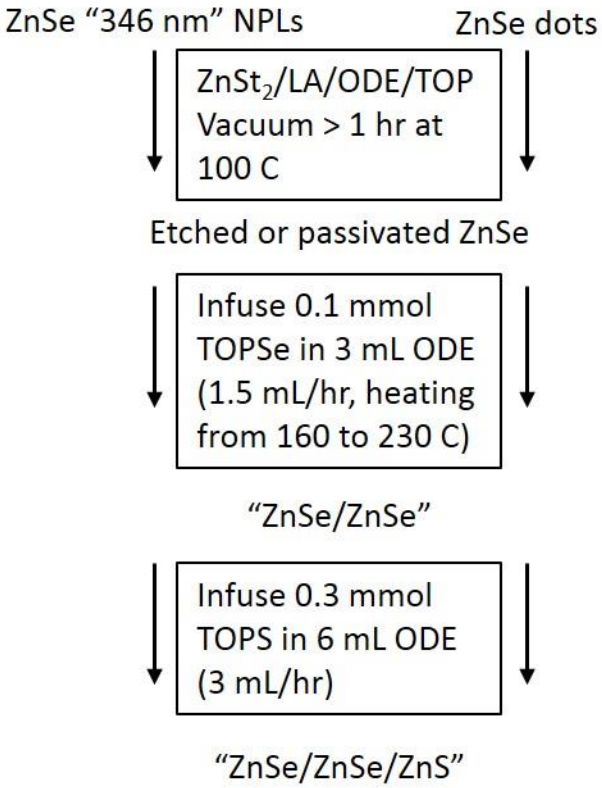

Figure 4.7. Reaction scheme used for comparative study of ZnS shell growth on spheres and nanoplatelets.

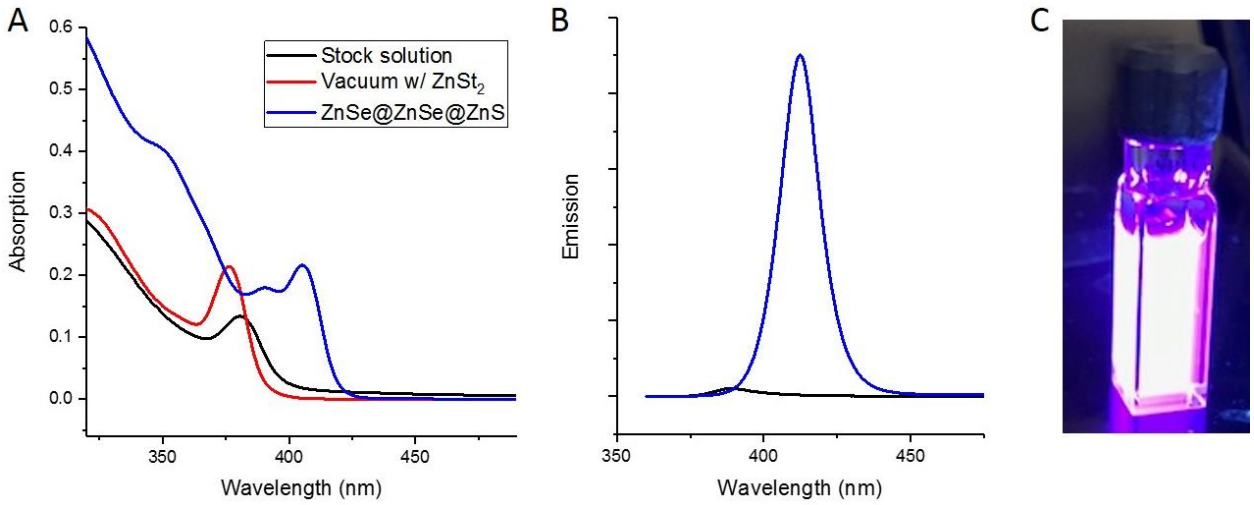

Figure 4.8. Evolution of absorption and emission along the shell growth pathway of ZnSe and ZnS on ZnSe: (a) Absorption of shell growth on spherical Zn-blende ZnSe dots. (b) Bright core-shells are obtained as evidenced by large increase in relative emission intensity. (c) Purple emission demonstrated under UV excitation.

The same protocol used on platelets revealed continued difficulty in achieving slow isotropic growth. After vacuum, the platelets redshift likely due to $ZnSt_2$ capping on the surface (Figure 4.9a). However, after a couple minutes of TOPSe infusion, there appeared a shoulder with no shift of original NPL peaks. It is likely that small nuclei are formed either on the platelet or separately and then attach. The same infusion yields one sharp peak at 420 nm in the absorption (Figure 4.9a). The PL is redshifted to 420 nm but quenches by a large magnitude (Figure 4.9b). This loss of PL is consistent with previous high temperature methods involved ZnSe addition. The morphology of these platelets shows small dots nucleated on the edges (Figure 4.10). The dot-on-plate morphology is formed almost exclusively under the conditions with one or two precursor infusion.

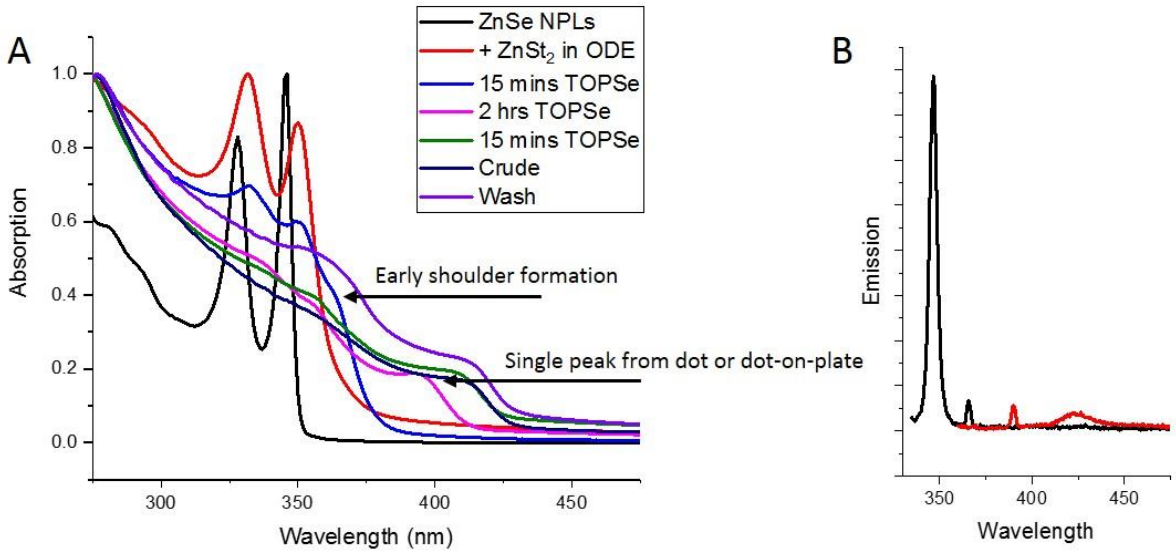

Figure 4.9. Optical characterization along the shell growth pathway of ZnSe and ZnS on ZnSe nanoplatelets: (a) Absorption of platelet species at different stages of TOPSe and TOPS overcoating. (b) Emission spectra before and after shell growth normalized to the intensity of the absorption wavelength used in excitation.

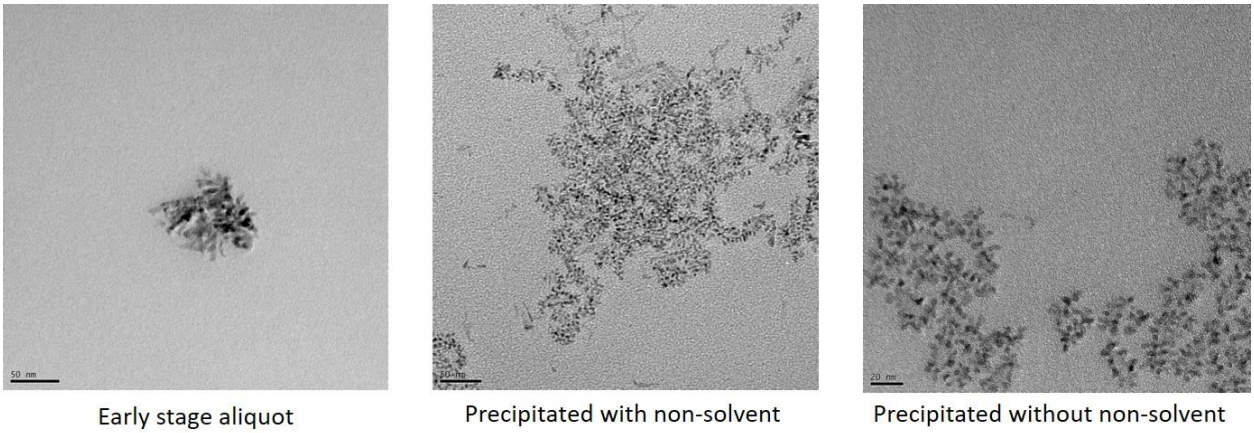

Figure 4.10. TEM of aliquots from shell-growth overcoating screening in Figure 4.9 shows dot-on-plate morphology.

4.4.3. Survey and issues of available high-temperature growth methods

It has been demonstrated that applying the successful high-temperature overcoating methods of ZnSe/ZnS spheres with ZnSe NPLs has several shortcomings. First, the nature of the surfaces and stability of ZnSe platelets were significantly different from spheres. For example,

we attempted to perform high temperature growth of thick-shell ZnS on ZnSe nanoplatelets using an establish protocol[8] by simply replacing cadmium oleate with zinc oleate.

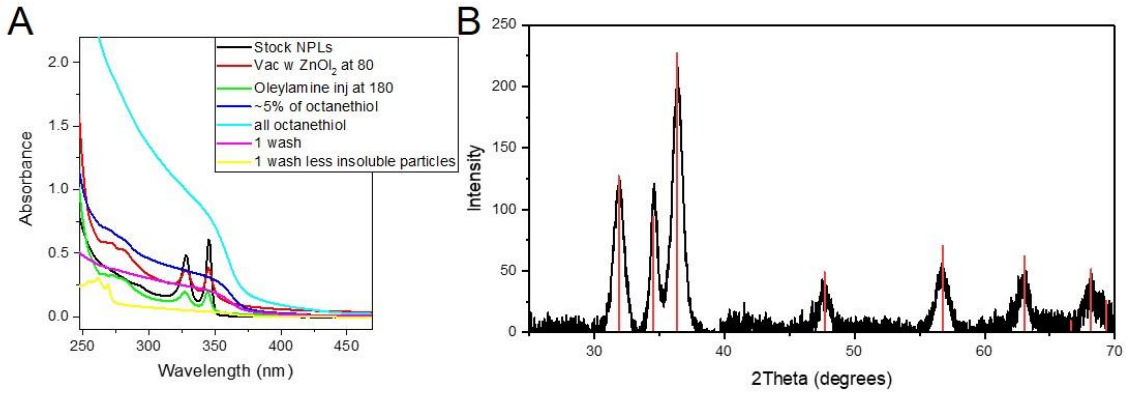

Figure 4.11. Protocol from ZnS shell growth adapted for ZnSe nanoplatelets: (A) Temporal evolution of absorption with respect to different reaction stages. (B) PXRD of majority product from reaction indexed with zinc oxide.

ZnSe/ZnS core-shell platelet growth was attempted using a modified procedure from Dubertret's group.[9-10] ZnSe NPLs were the same as used in experiments above and except precipitated twice from solution and resuspended in chloroform. About 2 mL of NPLs in chloroform (~10% of synthesis) was added to a vial and 100 mg of thioacetamide (TAA) in 1 mL octylamine was added to solution. An immediate change in the turbidity of the solution was observed, potentially due to the addition of octylamine creating bundling of nanosheets. To the solution, 500 uL of 0.2M $Zn(NO_3)_2$ in ethanol was added and the solution was stirred at RT for 2hrs. After noticing minimal change in excitonic peaks from starting material, the vial was gently warmed to 50 °C and spectra were collected after 8 and finally 24 hours (Figure 4.12a). The resulting particles were washed twice with a small volume of ethanol and subsequently resuspended in chloroform. To a 3-neck round-bottom flask, half of the resulting particles in chloroform were added along with 1 mL of 0.5 M $Zn(oleate)_2$ in oleic acid and 10 mL of

trioctylamine (TOA). The flask was vacuum degassed at 70 °C for 30 mins and then heated to 300 °C under nitrogen and allowed to grow for 30 mins. After annealing, the particles were isolated from the growth mixture and dispersed in methylcyclohexane.

Surprisingly, the particles showed bright cyan emission under UV excitation. The emission of these annealed platelets is likely indicative of emission coming from the defects of these ZnSe/ZnS structures. The initial emissive peak at 346 nm in ZnSe is around 50 meV whereas the peak broadens to 450 meV in the case of the annealed heterostructures (Figure 4.12b). The morphology of the structures appears to be monodisperse platelets in the starting material (Figure 4.12c). However, after shell-growth and annealing, the structures appeared to have irregular growth leading to non-uniform shapes (Figure 4.12d). The broad PL and irregular shape of the nanocrystals in TEM indicates that this technique was too harsh for the clean epitaxial growth on ZnSe nanosheets. One possibility is that the introduction of shorter chain primary and ternary amines during shell-growth can begin to dissolve cluster subunits that are responsible for the templated growth in this case.

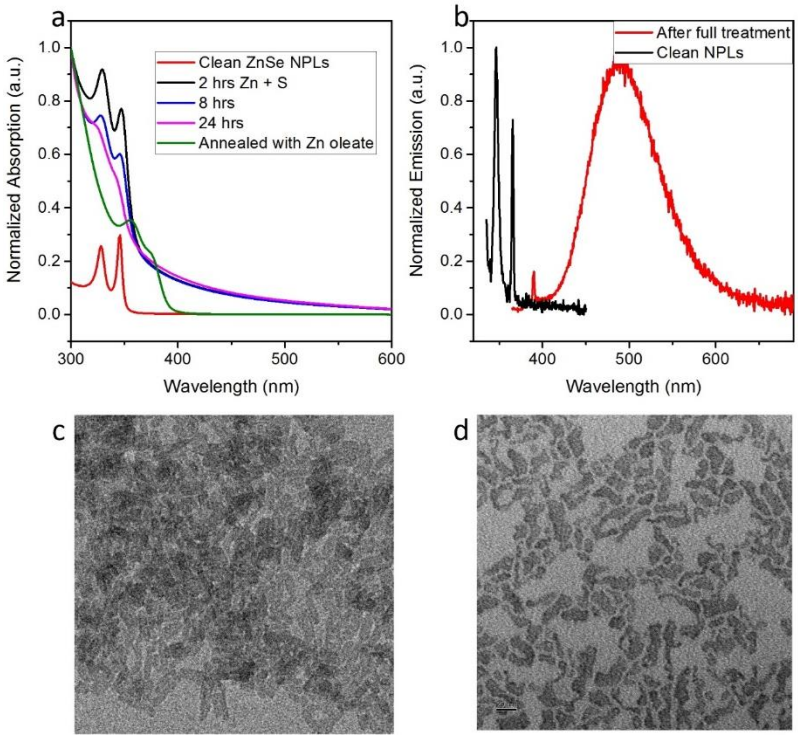

Figure 4.12. Two-step approach to growth of ZnS on ZnSe NPLs to yield thick-shelled composites: (a) Absorption spectra of particles along each step of shell-growth. (b) Emission of NPLs before and after shell-growth and annealing. (c-d) TEM of particles before shell-growth (c) and after high-temperature annealing (d).

Further attempts have yielded mixed results with respect to platelet quality. In many techniques, platelet quality is preserved even at temperatures above 200 ºC. Our first attempt of shell growth on 380 NPLs had secondary nucleates with some patchy shells grown (Figure 4.13a). However, the small absorption features present in the range of ZnSe structures showed a redshift all the way to 410 nm. 345 NPLs often allowed for cleaner shells due to the smaller monodisperse surfaces (Figure 4.13b-d). In this case, SILAR growth gave the cleanest deposition of 1 monolayer which yielded redshift to 380 nm (Figure 4.13b,e). Single precursor decomposition of Zn-dithiocarbamates has been successful in previous methods for CdSe/ZnS platelets.[11] This method appeared to give a mixture of structures with cleanly deposited cores and also platelets covered with dots (Figure 4.13c). The first exciton redshifted to 370 nm and did not

seem to complete the growth (Figure 4.13e). Finally, platelets can simply be heat-up in the presence of reactive TMS_2S and $ZnOl_2$, maintaining their morphology with apparent shell growth (Figure 4.13d). The corresponding platelets had the lowest energy feature at 385 nm (Figure 4.13e). These limited methods demonstrate that there are suitable and stable surfaces on ZnSe NPLs for clean shell-growth. The deposition of what is likely 1-2 ML yields comparable redshifts approaching visible spectrum. Despite showing promise for clean deposition and redshift, almost all species had negligible emission. Further optimization of shell growth on 380 NPLs is necessary to reveal the potential of ZnSe/ZnS core-shell NPLs.

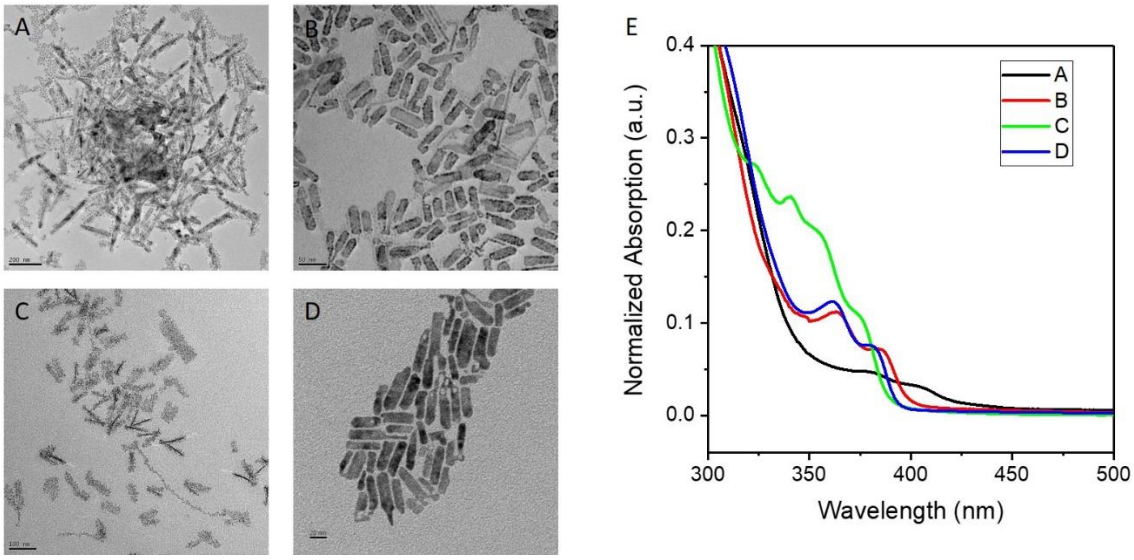

Figure 4.13. Morphological characterization and varying redshift in several ZnS shell growth methods. TEM images of varying shell-growth protocols: (a) One pot shell growth on 380 nm platelets; (b) "1 ML" of ZnS grown through layer-by-layer growth with $ZnOl_2$ and TMS_2S; (c) Single precursor decomposition of Zn-thiocarbamates on ZnSe platelets; (d) Rapid heating-up of TMS_2S and $ZnOl_2$ in the presence of platelets. (e) Absorption spectra of each of the final products from shell-growth protocols.

4.4.4. Future prospects and targets for ZnSe NPL based core-shells

To date we have only yielded one promising sample our first example of violet blue-emitting anisotropic nanostructures. The platelets had a sharp absorption onset with broader

features but relatively narrow emission at 405 nm (Figure 4.14a-b). However, these platelets were sufficiently compromised in terms of their structure, yielding patchy platelet-like structures (Figure 4.14c-d). Successful shell growth may involve significant alloying and restructuring in order to achieve uniform growth on the platelet surface. Additionally, methods of redshifting by growing additional ZnSe or using different additives could be attempted.

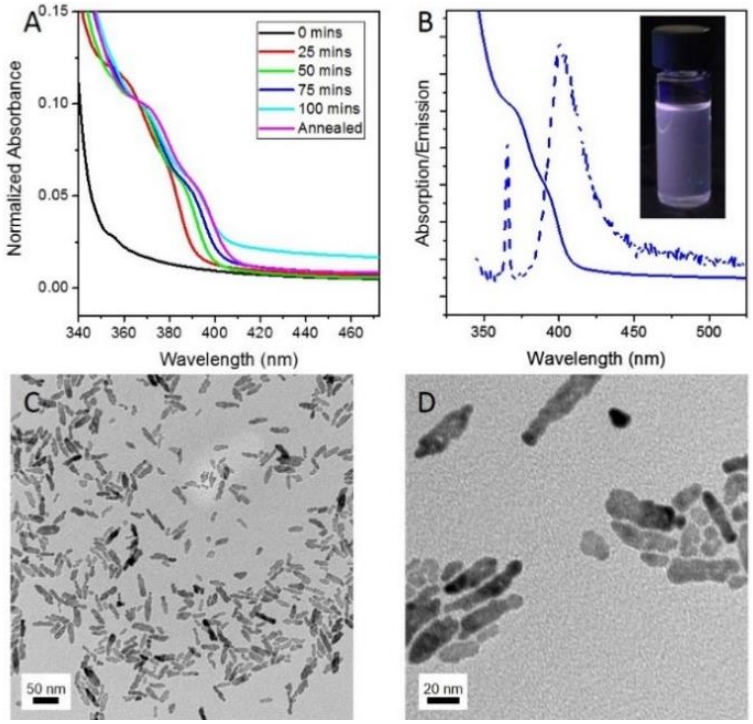

Figure 4.14. Attempted ZnS shell growth on ZnSe platelets using reactive $ZnEt_2$ and TMS_2S in a syringe pump injection: (a) Absorption monitored prior to adding precursor and at different subsequent growth times reveals an initial large redshift followed by small shifts to ~400 nm. (b) Final absorption and emission spectra of washed products with weak violet emitter shown under UV excitation (inset). (c-d) TEM of patchy core shell platelets.

4.5. **Colloidal atomic layer deposition on ZnSe**

Our group has developed demonstrated and applied the concept of c-ALD to colloidal nanomaterials.[12] The c-ALD process used self-limiting half-reactions coupled to the phase transfer of NCs or molecular precursors between immiscible nonpolar and polar phases. The phase

transfers facilitated the removal of unreacted molecular precursors and prevented accumulation of reaction byproducts. This procedure is very commonly used for the growth of CdS, ZnS, or alloyed shells on CdSe NPLs. It was our belief that many of these protocols could be used for ZnSe.

4.5.1. Test cases for two phase c-ALD as an established protocol

Because of the stoichiometric surfaces in ZnSe wurtzite platelets, it was hypothesized that ligand exchange was necessary to yield a metal rich surface. Our preliminary studies indicated that growing monolayers of ZnS or CdS using two-phase solution c-ALD is not facile for wurtzite ZnSe NPLs. Based on the literature, it is likely that these wurtzite quantum belts have stoichiometric (110) faces.[13] Upon ligand exchange with S^{2-}, the sulfide atoms will likely displace any datively bound amine ligands and form a quarter of a monolayer on each face of the nanoplatelet. After removal of excess precursor and addition of $Zn(OAc)_2$, another quarter monolayer is grown on each face in the ideal case. This would lead to two half-monolayers of ZnS on each nanoplatelet face. However, it is unclear if there is a driving force which would lead to complete S^{2-} exchange on neutral surfaces. Therefore, we hypothesized that ligand exchange with metal oleate complexes might yield Zn-rich surfaces for complete S^{2-} on the surfaces. It has recently been demonstrated that Cd and Zn oleate complexes can cleanly exchange and passivate amine-capped quantum belts, resulting in large excitonic shifts due to addition of 0.5 monolayers of metal atom.[13] We hypothesized that the metal rich surfaces would allow for clean exchange of sulfide in the first half reaction of c-ALD. The ZnSe platelets easily exchanged with metal oleate ligands, shifting their excitonic features (Figure 4.15a). Unfortunately, in the case of Zn oleate capped platelets, the sulfide exchange generally resulted in poor colloidal stability and aggregation at the interface. Any attempts to deposit another layer of Zn resulted in the formation of secondary nucleates and blue-shift of peaks back to their original position. Therefore, we opted to grow CdS

on Cd-oleate platelets as a test case for growing clean monolayers. In contrast to ZnS shells, the CdS monolayers yielded nice colloidal solutions. After just one monolayer of shell growth the absorption spectra becomes featureless likely due to type II band alignment of ZnSe/CdS (Figure 4.15b). The PL intensity is very weak after passivation and 1 ML growth but bright trap emission is observed after just 2 ML growth (Figure 4.15c). More importantly, we monitored the morphology with respect to the supposed deposition of each monolayer. Unfortunately, after just one monolayer of growth we begin to see the formation of small nucleates around the edges of the platelets (Figure 4.15d). Subsequent growth reveals a consistent preferential deposition of CdS as small dots around the edges of each platelet (Figure 4.15d). This selective nucleation appears to indicate that the edges of the platelet are more susceptible to attack by highly charged sulfide species. It is possible that the energetic surface reconstruction is high enough at room temperature to evenly deposit charged ligands on the neutral wurtzite surface. Passivation of these wurtzite structures grown from magic-sized nucleates can likely not be achieved using highly-charged species at room temperature.

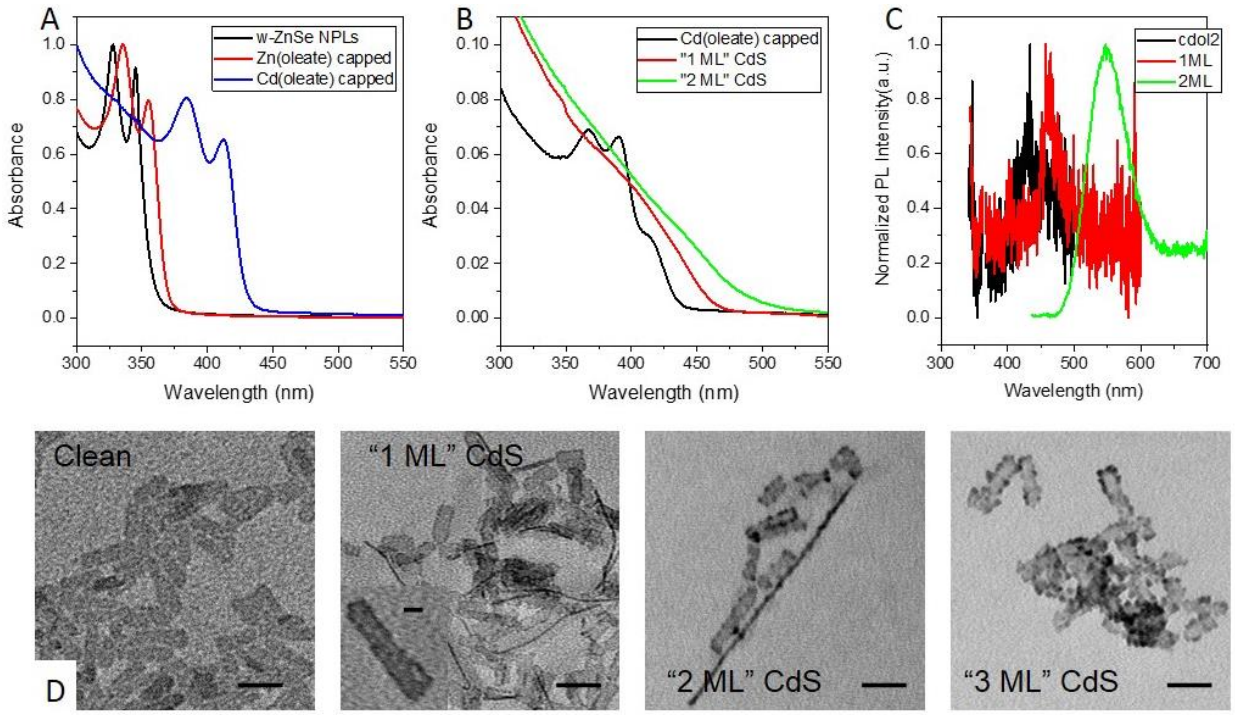

Figure 4.15. Ligand exchange and two-phase colloidal ALD to form ZnSe/CdS heterostructures: (a) Excitonic shifts monitored by absorption spectra with respect to ligand exchange using zinc and cadmium oleate. (b) Absorption and (c) emission spectra of ZnSe after ligand exchange with Cd oleate and subsequent monolayer growth of CdS. (d) TEM images used to monitor growth after each supposed monolayer deposition. Standard colloidal-ALD technique was adapted from ref.[14] Scale bar is 20 nm.

4.5.2. Z-type ligand exchange for metal-rich surface

After synthesizing ZnSe NPLs, the particles were transferred to the glove box and precipitated without non-solvent. After dissolving in 20 mL methylcyclohexane, the excess metal carboxylate was precipitated by slow centrifugation over half an hour. The resulting supernatant was precipitated with 10 mL ethanol and redispersed in 12 mL methylcyclohexane. To perform ligand exchange with $ZnOl_2$, 4 mL of stock solution was precipitated with 4 mL ethanol and redispersed in 2 mL toluene. To the solution in toluene, 2 mL of a 0.1 M solution of $ZnOl_2$ in ODE was added and allowed to stir for 1 hr at 60 °C. The solution was diluted to 10 mL with

toluene and the particles were precipitated with 5 mL methanol. The resulting precipitate was redispersed in methylcyclohexane and stored for later use.

The as-synthesized platelets had a first excitonic feature at 346 nm with weak narrow emission at 347 nm (Figure 4.16a). The $ZnOl_2$ capped particles had a small redshift to 353 nm likely associated with increasing the confinement dimensions of the ZnSe nanoplatelets (Figure 1a). The peak widths had minimal change, indicating nearly complete passivation of the nanoplatelet surface. Previous attempts at exchange at room temperature with lower concentrations of $ZnOl_2$ yielded similar shifts with much broader peaks. NPL morphology was preserved with respect to the exchange (Figure 4.16b). Scale up of $ZnOl_2$ exchange is a facile way to ensure that particles are metal rich. It is also believed that this will protect particles at high temperatures and allow them greater solubility in suitable high-boiling solvents like ODE.

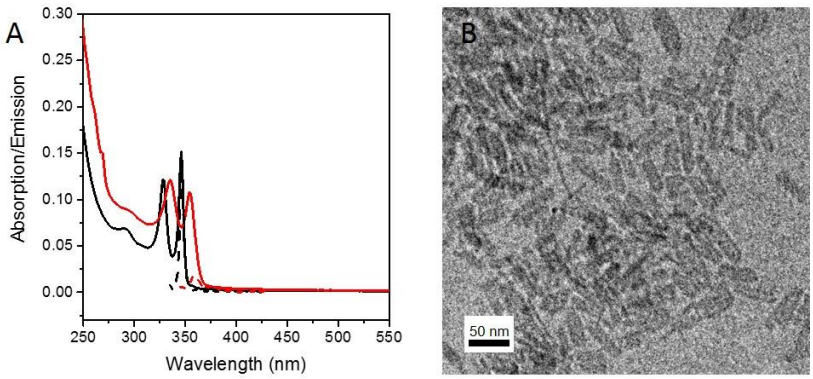

Figure 4.16. Z-type ligand exchange as a standard procedure for post-synthetic manipulations. (a) Absorption (solid) and emission (dashed) spectra of as-synthesized ZnSe NPLs (black curves) and $ZnOl_2$ washed and capped NPLs (red curves). (b) TEM image of $ZnOl_2$ capped platelets.

4.5.3. Nonpolar phase c-ALD

We report a method using layer-by-layer approach to growing ZnSe monolayers on ZnSe NPL structures. The approach used deposition of TMS_2Se followed by washing and sonication

with $Zn(OAc)_2$ for extended periods of time. It yielded large redshifts indicative of monolayer growth of ZnSe on ZnSe.

First, we compared one monolayer growth on as-synthesized vs. $ZnOl_2$ capped ZnSe. It is hypothesized that the Zn-capped particles will enable more reactive metal rich sites at the surface to install Se in the first layer deposition. Both sets of ZnSe NPLs were diluted in methylcyclohexane (200 uL stock solution + 1 mL solvent) and 50 uL of TMS_2Se was added. The solutions were stirred at room temperature for 1 hour and the NPLs were precipitated with a small amount of ethanol. After redispersion in methylcyclohexane, 0.5 mL of a 0.1 M solution of $ZnOl_2$ in ODE was added to complete the layered growth. The solutions were stirred at 75 °C for 30 mins and precipitated with ethanol. Final samples were redispersed in methylcyclohexane.

For as-synthesized particles, "1 monolayer" growth of ZnSe redshifts absorption to 393 nm with very broad peaks (Figure 4.17a). In comparison, "1ML" growth of ZnSe on $ZnOl_2$ capped solutions yields the same redshift to 393 nm with preservation of narrow peaks with another monolayer of growth pushing the first exciton to 405 nm (Figure 4.17b). The washing out of hh-lh peaks in the case of oleylamine capped platelets can likely be attributed to undercoordinated Zn sites after the first deposition of Se. It is possible that addition of Zn precursor in the second step of layer-by-layer growth does passivate some of these undercoordinated sites, but it is more facile to react with Se deposited via TMS_2Se rather than charge neutral amine-capped Se. The $ZnOl_2$ molecules likely coordinate two Se sites in the z-type exchange, allowing for a pseudo Zn-rich surface that can effectively react with TMS_2Se the first step. All overgrowth of these platelets preserved morphology, with the only indicator of growth being a slightly higher contrast in TEM (Figure 4.17c). More precise characterization of the nature of this crystallization is needed to understand the mechanism of ZnSe overcoating

using half reactions at the nanoplatelet surface. None of the initial structures demonstrated any PL, indicated that shelling and subsequent solvent annealing is necessary to obtain photoluminescence.

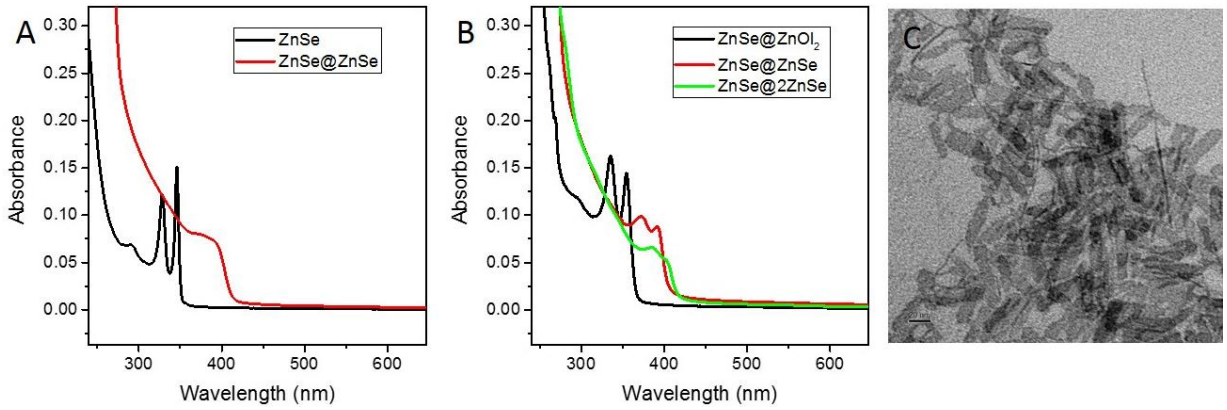

Figure 4.17. ZnSe monolayer growth on ZnSe using single nonpolar phase with reactive TMS_2Se. (a) Absorption spectra before and after 1 monolayer of ZnSe growth on amine-capped ZnSe NPLs. (b) Absorption spectra before and after 1 and 2 monolayers of ZnSe growth on $ZnOl_2$ capped ZnSe NPLs. (c) TEM image of ZnSe@ZnSe from panel B. The particles morphology is preserved.

Several challenges arise when using this approach to redshift of these NPL structures with c-ALD. The first is the scalability and stability of more concentrated solutions. When the concentration of reaction mixtures in the first step is increased three-fold, two issues arise. The solutions stirred with TMS_2Se become very turbid over time and after adding the Zn-layer, the solutions are not colloidally stable as indicated by the large scattering tail in the absorption spectra. Additionally, the exact redshift of the absorption wavelength was not strictly reproducible. This difference indicates that at the higher concentrations, some amount of stacking or instability hinders the clean deposition of 1 monolayer of ZnSe. Another challenge with this approach is washing required to remove highly reactive precursors and isolate NPLs

before growth. During these procedures, only one round of non-solvent precipitation was employed to try and minimize potential quenching of PL.

Ultimately, the c-ALD approach needs to yield highly emissive structures. It is unclear the effect of strain states or defects created by these layered growth approaches. This approach can be used to maintain the monodisperse platelet width, but such structures will likely need to be capped with ZnS and solvent-annealed to eliminate defects and passivate surfaces.

4.6. **Alternative strategies for blue emitters.**

Despite our conclusion that ZnSe/ZnS platelet structures can achieve blue-emission based on reduction of confinement energy, we only demonstrated limited success in growing core-shells. In parallel with the formation of ZnSe/ZnS nanoplatelet structures, we continue to explore several alternative possibilities. The inclusion of ZnTe into anisotropic structures could provide a facile way to blueshift the emission. Recently, it was reported that ZnTe/ZnSe nanodumbells can be synthesized and reach quantum yields between 30-40%.[15] We expect a similar strategy can be applied either in the doping of Te to form alloyed structures, or in the formation of core-crowns, dot-on-plates, or standalone ZnTe plates.

There remains the possibility for the use of III-V structures for the formation of Cd-free nanomaterials. InP based-emitters have comprised the majority of high QY, stable Cd-free structures. The difficulty in synthesizing anisotropic structures of such material is the preferred cubic phase at temperatures suitable for colloidal synthesis. However, future applications may utilize InP as an emissive material in the form of small clusters. Recently, work from Banin's group detailed the synthesis of magic-sized InP clusters with first excitons at 365 and 395 nm.[16] These clusters can be synthesized and potential included as co-synthons in ZnSe NPL prep. This

could potentially yield dot-in-plate, dot-rod, or core-crown structures. Additionally, both clusters and starting precursors could be grown on NPL and NW scaffolds for the growth of thin-shell emitters.

4.7. **Conclusions**

Despite some limitations in anisotropic growth of these structures, we have demonstrated the synthesis of two populations of atomically-precise colloidal ZnSe nanoplatelets with narrow linewidth UV emission. Initial attempts at shell-growth have produced the first examples of blue-emitting anisotropic Zn-based structures. Optimization of synthesis conditions along with Zn-chalcogenide shell growth could potentially yield highly emissive blue anisotropic structures. Additional knowledge of strategies for ZnSe anisotropic growth can inform strategies for the growth of exotic core-shell structures containing III-V materials like InP. Ultimately, it is believed that inorganic nanocrystals with blue emission can be incorporated as QD-LEDs in future display applications.

4.8. **References**

1. Scott, R.; Heckmann, J.; Prudnikau, A. V.; Antanovich, A.; Mikhailov, A.; Owschimikow, N.; Artemyev, M.; Climente, J. I.; Woggon, U.; Grosse, N. B.; Achtstein, A. W., Directed emission of CdSe nanoplatelets originating from strongly anisotropic 2D electronic structure. *Nature Nanotechnology* **2017,** *12*, 1155.

2. P.Yu; Cordona, M., *Fundamentals of Semiconductors*. 2001.

3. Olutas, M.; Guzelturk, B.; Kelestemur, Y.; Yeltik, A.; Delikanli, S.; Demir, H. V., Lateral Size-Dependent Spontaneous and Stimulated Emission Properties in Colloidal CdSe Nanoplatelets. *ACS Nano* **2015,** *9* (5), 5041-5050.

4. Pikus, G. E. B., G. L., *Fiz. Tverd. Tela* **1959,** *1*, 1641.

5. Antanovich, A.; Achtstein, A. W.; Matsukovich, A.; Prudnikau, A.; Bhaskar, P.; Gurin, V.; Molinari, M.; Artemyev, M., A strain-induced exciton transition energy shift in CdSe nanoplatelets: the impact of an organic ligand shell. *Nanoscale* **2017,** *9* (45), 18042-18053.

6. Dong, B.; Cao, L.; Su, G.; Liu, W., Facile synthesis of highly luminescent UV-blue emitting ZnSe/ZnS core/shell quantum dots by a two-step method. *Chemical Communications* **2010,** *46* (39), 7331-7333.

7. Kumano, H.; Nashiki, H.; Suemune, I.; Arita, M.; Obinata, T.; Suzuki, H.; Uesugi, K.; Nakahara, J. i., Excitonic properties of zinc-blende ZnSe/MgS superlattices studied by reflection spectroscopy. *Physical Review B* **1997,** *55* (7), 4449-4455.

8. Rossinelli, A. A.; Riedinger, A.; Marqués-Gallego, P.; Knüsel, P. N.; Antolinez, F. V.; Norris, D. J., High-temperature growth of thick-shell CdSe/CdS core/shell nanoplatelets. *Chemical Communications* **2017,** *53* (71), 9938-9941.

9. Mahler, B.; Nadal, B.; Bouet, C.; Patriarche, G.; Dubertret, B., Core/Shell Colloidal Semiconductor Nanoplatelets. *Journal of the American Chemical Society* **2012,** *134* (45), 18591-18598.

10. Tessier, M. D.; Mahler, B.; Nadal, B.; Heuclin, H.; Pedetti, S.; Dubertret, B., Spectroscopy of Colloidal Semiconductor Core/Shell Nanoplatelets with High Quantum Yield. *Nano Letters* **2013,** *13* (7), 3321-3328.

11. Polovitsyn, A.; Dang, Z.; Movilla, J. L.; Martín-García, B.; Khan, A. H.; Bertrand, G. H. V.; Brescia, R.; Moreels, I., Synthesis of Air-Stable CdSe/ZnS Core–Shell Nanoplatelets with Tunable Emission Wavelength. *Chemistry of Materials* **2017,** *29* (13), 5671-5680.

12. Ithurria, S.; Talapin, D. V., Colloidal atomic layer deposition (c-ALD) using self-limiting reactions at nanocrystal surface coupled to phase transfer between polar and nonpolar media. *Journal of the American Chemical Society* **2012,** *134* (45), 18585-18590.

13. Zhou, Y.; Wang, F.; Buhro, W. E., Large Exciton Energy Shifts by Reversible Surface Exchange in 2D II–VI Nanocrystals. *Journal of the American Chemical Society* **2015,** *137* (48), 15198-15208.

14. She, C.; Fedin, I.; Dolzhnikov, D. S.; Demortière, A.; Schaller, R. D.; Pelton, M.; Talapin, D. V., Low-Threshold Stimulated Emission Using Colloidal Quantum Wells. *Nano Lett.* **2014,** *14* (5), 2772-2777.

15. Ji, B.; Panfil, Y. E.; Banin, U., Heavy-Metal-Free Fluorescent ZnTe/ZnSe Nanodumbbells. *ACS Nano* **2017,** *11* (7), 7312-7320.

16. Ning, J.; Banin, U., Magic size InP and InAs clusters: synthesis, characterization and shell growth. *Chemical Communications* **2017,** *53* (17), 2626-2629.